Methods for a dedicated breast cancer scanner combining positron emission tomography (PET) and mammography imaging

Geng Zeng

A dissertation

submitted in partial fulfillment of the

requirements for the degree of

Doctor of Philosophy

University of Washington

2018

Reading Committee:

Paul E. Kinahan, Chair

Lawrence R. MacDonald

Richard Jeffrey Wilkes

Program Authorized to Offer Degree:

Physics

University of Washington

Abstract

Methods for a dedicated breast cancer scanner combining positron emission tomography (PET) and mammography imaging

Geng Zeng

Chair of the Supervisory Committee:
Dr. Paul E. Kinahan
Department of Radiology

The PET/X breast imaging system is designed to be a compact positron emission tomography (PET) scanner with a rectangular field of view (FOV) that can be mounted directly over the conventional mammography scanner. This thesis studies the prototyping of this dedicated breast cancer scanner that combines PET and mammography, using mostly computer modeling methods, while the hardware of data acquisition system is being concurrently developed. Apart from processing scripts and functions, two major simulation software packages are used: SimSET and CatSim. The former models PET emission process and the latter models mammography projection. This thesis delves into the details of using these packages and presents results of applying them to the PET/X system. By studying reconstructed images using

simulated PET data, this thesis characterizes the proposed PET/X scanner and estimates its performance upper bound. Under several idealized detector conditions, the PET/X scanner exceeds the design goal of detecting a 20% change of radiotracer concentration with high sensitivity and specificity. This thesis also explores the use of X-ray (mammography) images for necessary attenuation correction of the PET data. Preliminary result shows that the X-ray-based attenuation correction (XAC) method has potential to be a surrogate for ground truth attenuation correction for the PET/X system.

TABLE OF CONTENTS

LIST OF FIGURES

LIST OF TABLES

ACKNOWLEDGEMENTS

I'd like to express my foremost gratitude to Paul Kinahan, my advisor and the chair of defense committee. His tireless work ethics inspired me as a researcher and his calming and fatherly personality made my PhD years a memorable journey. Albeit busy beyond one could imagine, he always made sure of his accessibility to us graduate students and offered insightful suggestions and critiques. I would not have reached to this point academically without his generous guidance.

I would also like to thank my other advisor, Larry Macdonald, who kindly took me in under the PET/X project that ultimately turned into my thesis topic. He supervised me on a daily basis and our relationship continued even after his departure from daily operations in the lab. His meticulous attention to details and down-to-earth personality made a long-lasting impression on me.

I'm also grateful to my coworkers (or should I say teachers), Larry Pierce, Darrin Byrd and William Hunter, for their infinite patience when I constantly harassed them with MATLAB questions when I first started in the lab. Their intellectual curiosity often sparked interesting discussions and debates around the flex space table, creating many memorable moments over the years.

As I relive a typical day of my life in the lab, many faces come into view. Sandra Johnston brightens up everyone's day with warm greetings, Adrienne Lehnert surprises me with her decently fluent Spanish, Don DeWitt's cute pets. Robert Miyaoka's impressive knowledge about detectors. Adam Alessio's monthly Machine Learning journal club. And everyone's jaws

drop upon seeing Nate Bell's uber-fancy celebratory lab events, Friday snacks and a constant supply of donuts, breads and cupcakes for the poor and hungry souls. The sugar and butter are so enticing that even Mike Hoff, a coworker/ally from the neighbor office, frequents the flex space to partake in the joy.

No graduate school experience would be complete without the fellow master/PhD/post-doc labmates: Laurie Zhang, Efren Lee, Kristen Wangerin, Ruoqiao Zhang, David Perlmutter, Carina Pereira, Chris Sanchez, Soo Mee Kim and other visiting students from abroad. You all have become an integrated part of the IRL experience that I'll cherish dearly as I embark on the next chapter of life.

From my home department of Physics, I'd like to specifically thank Catherine Provost, Marcel den Nijs and Steve Sharpe. Their support and encouragement provided a source of strength and perseverance at difficult times.

At least I want to highlight the wonderful friends I crossed path with in the city of Seattle. Moving to the city was life changing in so many ways and the friendship I forged here will forever define who I am and where I head to in the future. I have so much fond memory of doing fun stuff with you all. Thank you for showing me the colorful life outside school and for helping me discover more about myself.

DEDICATION

To my loving parents who have given up so much in their lives to bring me to where I am today.

I'm forever grateful for their unconditional support, love and faith in me.

Chapter 1. INTRODUCTION

1.1 BREAST CANCER OVERVIEW

1.1.1 *Cancer overview*

Colloquially cancer represents a malignant tumor. More broadly, cancer is a clinical condition that is manifested by the presence of one or another type of neoplastic growth [1]. As cancer cells mutate from normal cells, they become less specialized and continue dividing without stopping or dying. The immune system may fail to recognize them and, at a later stage, they can often break off and travel to other parts of the body via bloodstream or the lymph system.

Cancer cells are also very heterogeneous in their genetic composition, varying from organ to organ and from person to person. Even within cells of the same tumor, genetic heterogeneity presents. Cancer cells can continue to mutate as they divide. All these variations make the profiling and treatment of cancer extremely difficult.

Given the versatility of cancer cells, it's not surprising that cancer is the second leading cause of death in the US. The number trails closely behind the top killer (heart diseases) and comes far ahead of the rest other causes. In 2015, each of these 2 leading causes, heart diseases and cancer, took around 600 thousand lives in the US. Combined, these two categories account for 45% of all deaths in the country [2].

Along with high mortality, cancer is also a lot more prevalent than many of us might perceive. With age, the risk of developing cancer increases dramatically. For example, men over 70 are 10 times more likely to develop invasive cancer than those under 49. It is estimated that one in three US persons would eventually develop some cancer in their lifetime [2].

If we further exam the statistics by cancer subtypes, the mortality rates and incidence rates can vary significantly. Overall, lung/bronchus claims a quarter of the death toll, followed by prostate/breast, colon/rectum, and pancreas, in decreasing numbers. Together these four cancer types attribute to over half of the total cancer deaths. It's important to note that although prostate/breast cancer (for men and women) is the 2nd most lethal type of cancer, they are far more common in new patients. 19% of the new cancer cases in men are prostate cancer, followed by lung/ bronchus (14%). For women, breast cancer is found in staggering 30% of the new cancer cases, compared to the 2nd place of lung/bronchus (13%) [2].

Due to its large share of the death toll, lung/bronchus cancer shapes the landscape of cancer statistics in the US. The overall cancer death rate peaked in 1991 (215.1 per 100,000 population), and since then has continuously dropped by 26% by 2015 (158.6 per 100,000 population). It was mostly due to the declining death rate of lung/bronchus cancer in men, which is correlated to the drop of number of smokers over the decades [2].

Cancer treatments vary from cancer types, and recently there's an increasing trend of personalized treatment that is tailored to individual's cancer genetic profile. NIH National Cancer Institute summarizes the common treatment types into the following categories: surgery, radiation therapy, chemotherapy, immunotherapy, targeted therapy, hormone therapy, stem cell transplant, and precision medicine. Most people receive a combination of treatments either concurrently or sequentially.

1.1.2 *Breast cancer*

Breast cancer is the most prevalent cancer in US women, with roughly one in eight women developing it in their lifetime. The incidence rate increases with age and peaks in their 70's. Racial and ethnic disparity is also present: non-Hispanic black and non-Hispanic white have

incidence rates that range from a quarter to a third higher compared to the other minority groups [3].

After lung/bronchus, breast cancer is the second most deadly cancer in US women. However, if we look into age groups, breast cancer is the leading cause of death among US women in both age brackets of 20-39 and 40-59. Not until in older age brackets (60-79 and 80-above) does lung cancer surpass breast cancer, due to the former's much higher mortality rate [2].

If diagnosed early and with proper treatment, breast cancer is very curable. The 5-year survival rate for local stage patients is well over 90%, and for regional stage over 85% (except for non-Hispanic black women at 78%). Even at distant stage, the 5-year survival rate is over 26% across all races (26%-40%). From 1989 to 2015, breast cancer death rate decreased almost 40%, thanks to advances in treatment and early detection [3]. The American Cancer Society recommends annual mammographic screening between ages of 45 to 54. Screening at a younger age is recommended if breast cancer is present in family history or BRCA mutation is present in the patient's genetic profile.

Breast cancer is no exception to cancer in general in that it displays great gene heterogeneity and can metastasize to other parts of the body. Therefore a diverse group of treatment types are utilized, and in majority of the cases, the patient receives more than one type of treatment [4]. Except for stage 4 patients, surgery is the most common treatment. A surgical procedure can be either mastectomy or breast-conserving surgery (also known as lumpectomy). Lumpectomy is more preferred for stage 1 and 2 patients, while mastectomy is most chosen for stage 3 patients. In recent years, there has been a trend of patients opting for mastectomy in favor of lumpectomy [5]. Other treatment options include radiation therapy, chemotherapy, hormone therapy, immunotherapy and targeted therapy. Breast cancer therapy development is going

through a rapid expansion right now. At the time of writing, cancer.org lists over 70 drugs FDA has approved to treat breast cancer. (https://www.cancer.gov/about-cancer/treatment/drugs/breast)

1.2 RADIATION PHYSICS

In medical physics, three out of four major types of photon-atom interactions are relevant: Rayleigh scattering, Compton scattering and photoelectric effect. The fourth one, pair production, is only possible when the energy of incident photon exceeds 1 MeV. It doesn't really apply to diagnostic imaging.

1.2.1 *Rayleigh scattering*

Rayleigh scattering, also known as coherent or classical scattering, is when the incident photon interacts with the entire atom. The photon is then scattered with the same energy. It's mostly seen in lower energy photons, and accounts for less proportion as the energy increases. (10% at 30 keV and 5% at 70 keV in soft tissue.) It usually plays a small role in medical imaging.

1.2.2 *Compton scattering*

Compton scattering, also known as inelastic or nonclassical scattering, is when the incident photon excites a valence electron, ejects the electron and then gets scattered with less energy. It's the predominant type of scatters in soft tissue at diagnostic imaging energy, and follows the equation:

$$E_{sc} = \frac{1}{\frac{1}{E_o} + \frac{1 - \cos\theta}{511\ keV}}$$

where E_{sc} is the energy of the scattered photon, E_o is the energy of the incident photon and θ is the scatter angle. It can be shown that at θ = 90 degrees the maximum energy of the scattered photon is capped at 511 keV (and 255 keV at θ = 180 degrees).

For PET (positron emission tomography), since the unattenuated photon is of 511 keV, the maximum energy of the scattered photon is 255 keV at θ = 90 degrees and 170 keV at θ = 180 degrees.

1.2.3 *Photoelectric effect*

Photoelectric effect is when the incident photon gets absorbed by often an inner shell electron, which then gets ejected. It's more likely to happen when the incident photon energy is slightly above the binding energy of the electron.

$$probability\ of\ absorption \propto \frac{Z^3}{E^3}$$

where Z is the atomic number and E is the energy of the incident photon. It's the primary type of interaction between photons and hardware component (detectors, shielding, etc.). After the inner shell electron is ejected, outer shell electrons

may fall in to fill the vacancy, giving off characteristic X-rays.

Absorption edge is a unique phenomenon associated with photoelectric effect. As energy increases, the photoelectric absorption generally goes down, except that at places where the energy level just crosses the binding energies of inner shell electrons, the absorption gets a boost. Graphically it shows as a sharp jump in the attenuation coefficient. Since they occur at the binding energies of the atom's electrons, absorption edges are also characteristic of each material.

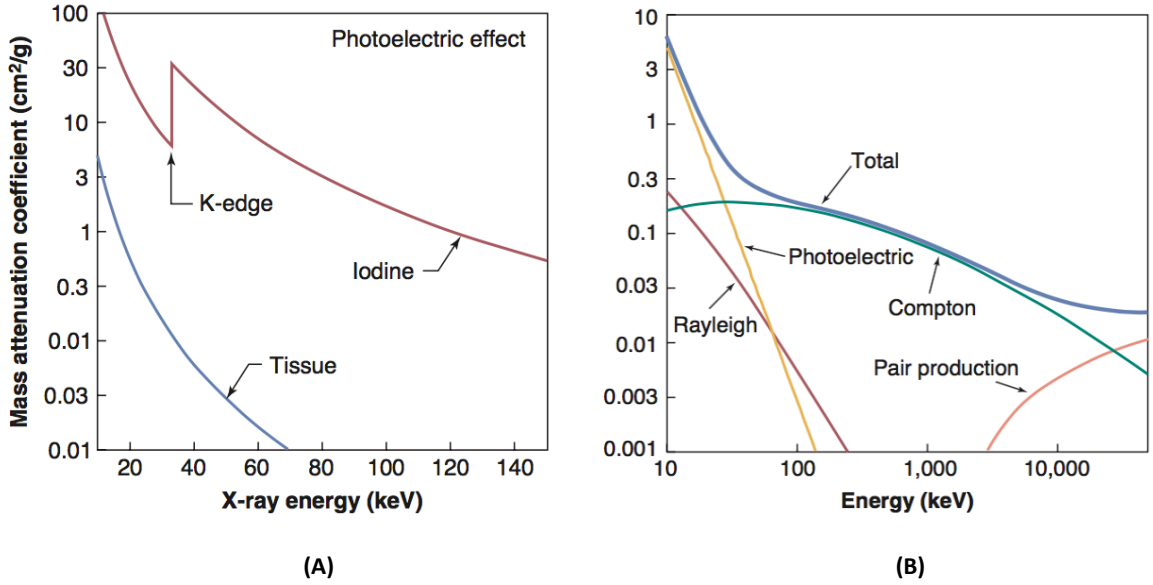

Figure 1.1. Attenuation coefficient as a function of X-ray energy.

(A): attenuation coefficients for soft tissue (Z = 7) vs. contrast agent iodine (Z = 53). One can see the abrupt increase of attenuation coefficient for iodine at the K-edge (33.2 keV). (B): attenuation coefficients breakdown for soft tissue (Z = 7) as different energies. We can see that in the diagnostic range (20 - 50 keV), photoelectric absorption and Compton scatter constitute the majority of the attenuation. Credit to Bushberg [6].

1.3 MAMMOGRAPHY

1.3.1 *Mammography physics*

Mammography is a radiographic examination specifically designed for breast imaging. The main components of a digital mammographic scanner are the X-ray tube and the planar detector.

The mammographic X-ray tube is similar to that of CT, but with a much lower bias voltage and current, and a shorter duration. The anode target material is usually molybdenum, rhodium or tungsten. The former two are chosen for their characteristic radiation that fall nicely into the energy range of mammography, while tungsten, a standard CT anode material, is chosen

for the high efficiency of bremsstrahlung production and high melting point. Given the composition of breast tissue, the ideal energy range is around 15 – 20 keV; too high gives little contrast and too low gives too much dose. In addition, the bremsstrahlung spectrum is further filtered by a flat molybdenum or rhodium film in order to reduce the amount of photons on the lower end of energy spectrum. This cuts the unnecessary dose imparted to the patient. The choice of flat filter material depends on the target material, with the usual combination of target/filter being Mo/Mo, Mo/Rh and Rh/Rh. The pairing of Rh/Mo is not practical as Mo's K-edge is lower than Rh's; doing so would filter out much of Rh's characteristic radiation.

Table 1.1. X-ray properties of molybdenum and rhodium for mammography

Material	Characteristic X-ray Emission (keV)	K-edge (keV)
Molybdenum	17.5 / 19.6	20.0
Rhodium	20.2 / 22.7	23.2

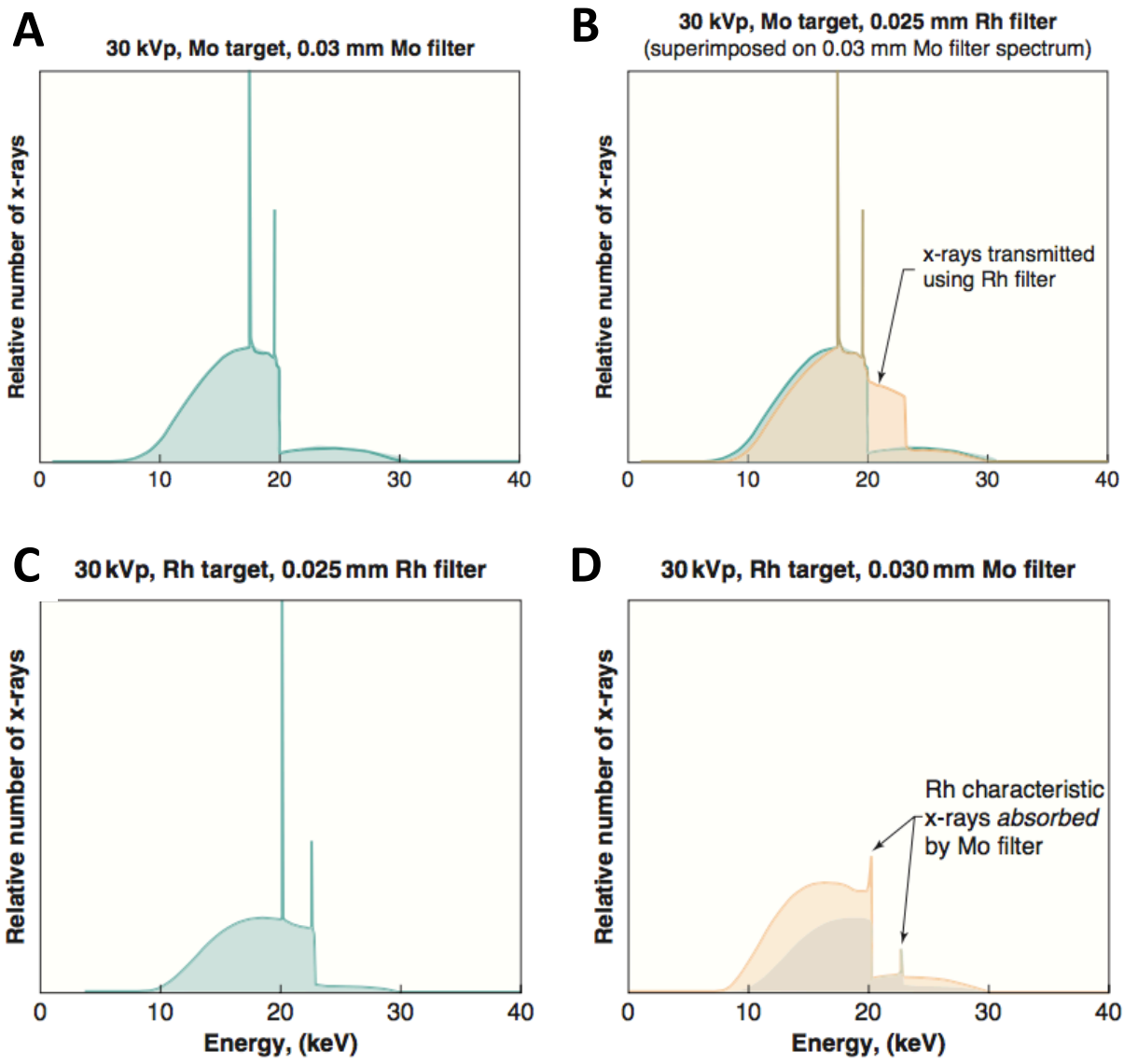

Figure 1.2. Filtered spectrum of 4 combinations of target/filter materials.

(A): Mo/Mo. Note the characteristic X-rays of Mo are preserved since they are below the K-edge of Mo. (B): Mo/Rh (yellow). Similar to Mo/Mo (green), but with more transmitted high energy photons due to the higher K-edge of Rh. (C): Rh/Rh. (D): Rh/Mo (yellow). It's not clear what the overlaid green spectrum is. An undesired combination: Mo's K-edge is below both peaks of Rh's characteristic X-rays. Doing so would attenuate much of Rh's desired characteristic X-ray photons. Credit to Bushberg [6].

The digital detector is a large rectangular plane of sides between 20-30 cm with a pixel resolution of sub-0.1 mm. An image would usually take storage space on the order of 10 MB. (If *For Processing,* along with *For Presentation*, images are stored, another factor of two increase is incurred). Embedded in the detector there is usually an array of additional photon sensors that form the Automatic Exposure Control unit (AEC). It prevents under- or over-exposure, and serves as a safe check on technologists' operation.

A mammography scanner also has several other unique components. The compression paddle is a clear piece of plastic that moves vertically and compresses the breast from above to a certain thickness. It helps with the separation of overlaying breast tissue and hence reduces misreading of abnormalities in the mammogram. In situations where spot compression or magnification becomes necessary, a smaller compression paddle is used only on a focused part of the breast.

Another feature of mammography is an anti-scatter grid, which transmits about 60% to 70% of primary X-rays and absorbs 75%-85% of the scattered radiation [6]. Since the mammographic X-ray energy is fairly low, the scatter to primary ratio is noticeably much higher than that of CT (Figure 1.3). The grid is also commonly referred as the *bucky*. During a scan, the bucky oscillates back and forth at a high speed to avoid gridline artifacts on the image.

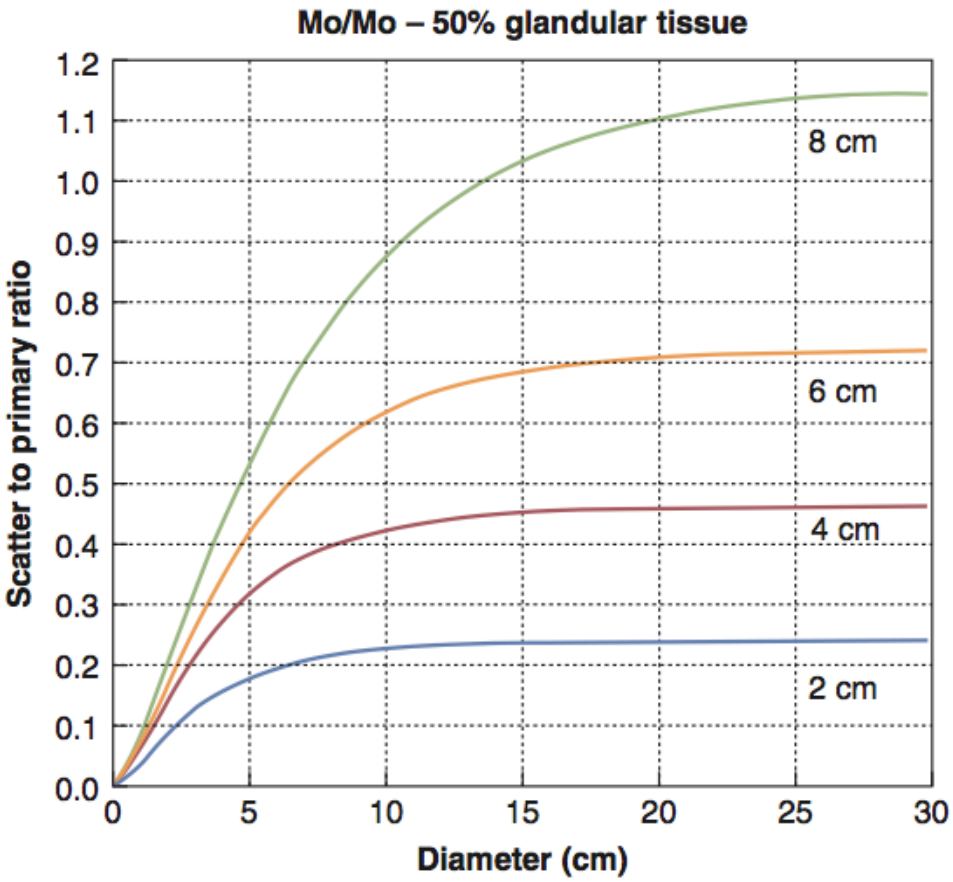

Figure 1.3. Scatter to primary ratio as a function of breast thickness and field area. Scatter in mammography depends on the thickness and size of breast. The tissue is taken as 50% glandular and 50% adipose. Credit to Bushberg [6].

Mammography can operate with a regular FOV, or with magnification. In the latter case, the bucky becomes unnecessary. Instead, a transparent magnification platform is inserted between the breast and detector. Since the breast is elevated away from the detector, the detected scatters are considerably reduced. Several magnification factors between 1x and 2x are usually available.

1.3.2 *Mammography in breast care*

Mammography is the predominant and standard screening tool for breast cancer. In developed western countries, the screening rate has been consistently over 60% in the past decades [7]. In the US, mammography screening for 40 year old and over underwent a rapid growth at the turn of 90's and plateaued around 65% in the 2000's, according the report on long-term trends in health published by CDC (Centers for Disease Control and Prevention) (https://www.cdc.gov/nchs/hus/contents2016.htm#070).

There's no doubt that mammography helps diagnose early stage breast cancer. Since the introduction of screening mammography, the detected incidences for early stage cancer have more than doubled from 1970's to 2000's [8]. However, mammography struggles with dense breast, a condition associated with marked higher risk of cancer. Study found that over 40% of the women aged 40 to 75 have dense breast, with younger patients having a higher proportion than older patients [9]. Screening with this complication leads to many false positive recalls and biopsies that are ultimately negative for cancer. In the recent years, there has been much debate on the necessity of the annual/bi-annual screening recommendation by USPSTF (the US Preventive Services Task Force) on the consideration of overdiagnosis, dose concern and cost-benefit analysis [10; 11].

In the meantime, prescribing supplementary imaging along with mammography screening, such as ultrasound and MRI, has been gaining popularity, especially when dense breast is involved. Emerging technology is also being transformed from research into clinics. For example, in 2011 FDA approved DBT (digital breast tomosynthesis), and now many mammography scanners are equipped with the capability to upgrade to tomosynthesis with an

add-on arm. A survey in 2016 shows that almost 80% of the radiologists use DBT now, and a quarter of the users used only DBT (without 2D images) [12].

1.4 POSITION EMISSION TOMOGRAPHY

1.4.1 *PET physics*

Positron emission tomography (PET) images patients by detecting gamma rays from the targeted tissue (often cancer tumors) that accumulates radioactive tracers. The isotopes emit positrons that soon annihilate with surrounding electrons and sends out a pair of gamma photons of 511 keV in opposite directions. If both photons are detected by PET detectors, that's called a coincidence event and the two locations where the pair of photons interact with the detector crystals form a line of response (LOR).

In reality, a LOR does not always represent truthfully the decay location. It is possible that one or both of the photons are scattered in the patient and hence change their courses of trajectory. This is referred to as a scatter coincidence. In other cases, one could detect a coincidence event of two photons, each coming from a different decay, but they happen to arrive at the detectors within the same time window. This is referred to as a random coincidence. Both types of coincidence, as shown in the figure, lead to erroneous LORs as they do not go through the true decay locations. In contrast, the desirable kind is called true coincidence.

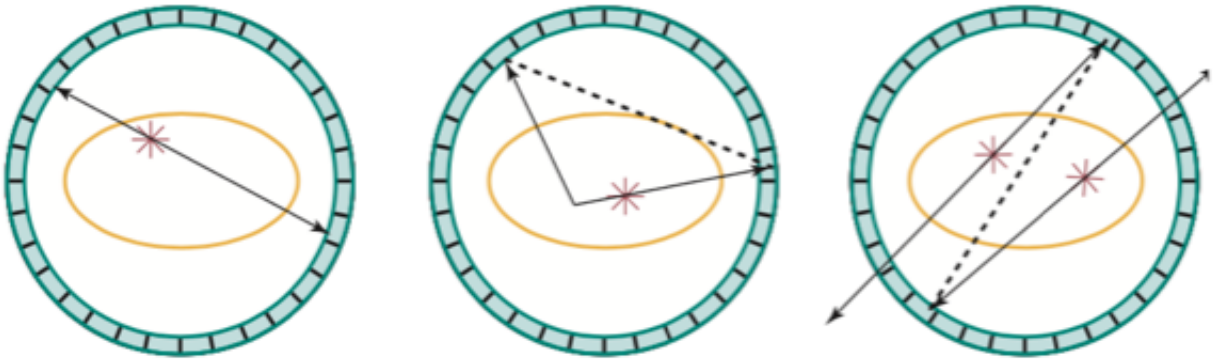

Figure 1.4. Three types of coincidence events.

Left: true coincidence. Both detected photons originate from the same decay and are not scattered in the object. Middle: scatter coincidence. Even though both photons originate from the same decay, one or both are scattered and therefore the LOR does not go through the decay location. Right: random coincidence. The paired detected photons are not from the same decay process. Credit to Bushberg [6].

Coincidence photons detector rely on the interaction between gamma photons and scintillation crystals in the detector modules. The scintillation material reacts by emitting visible light that is picked up by photomultiplier tubes (PMTs) or silicon photomultipliers (SiPMs). Common scintillation materials for PET include NaI(TI), BGO, GSO, LSO and LYSO. Their properties can differ in term of response time, attenuation coefficient at 511 keV, conversion efficiency to visible light and cost etc.

One, if not the most, important aspect in PET imaging is the attenuation of 511 keV photons during the emission process. Intuitively, decays occurring in the center of the patient will experience more attenuation, as the photons travel more distance through the body to reach the detectors, than the decays from body surface of the patient. This, if not corrected, leads to a

dishing artifact in the reconstructed image, i.e. the exterior of phantom body appears to have artificially higher activity of decays than the interior.

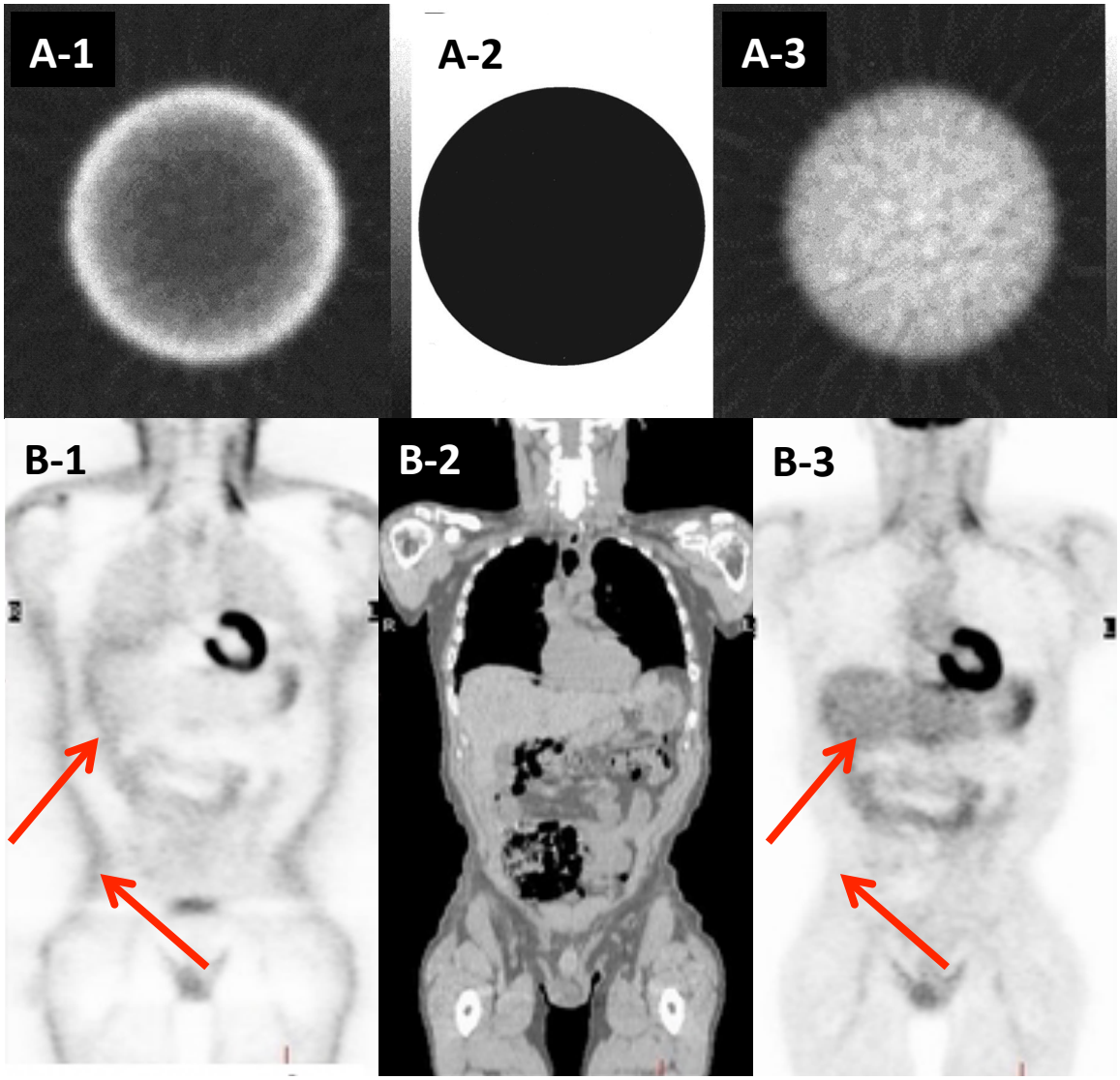

Figure 1.5. PET scans of a uniform cylindrical phantom (A's) and a patient (B's). (Column 1): reconstructed images with no attenuation correction. One can observe the dishing effect where the surface/boundary appears hotter than the inside. In B-1, one can notice that the skin and the boundary of liver are artificially hotter. (Column 2): attenuation map obtained from CT scans. (Column 3): images with attenuation correction. In A-3 the uniformity within the circle is restored. B-3 shows the normalized skin and liver area.

The prominence of attenuation effect stresses that the attenuation correction (AC) is indispensible. For that purpose, nowadays almost all the clinical PET scanners are equipped with a sequential CT to obtain the anatomical structure that can be converted to an attenuation map at 511 keV. For the few unconventional PET scanners, AC are obtained from other imaging modalities in conjunction or inferred from the PET emission data.

Mathematically AC is a multiplicative factor that can be applied to the original measured data. As shown (Figure 1.6), the probability of photons going through the patient in the downward direction is:

$$P_1 = e^{-\int_0^x \mu(s)ds}$$

where μ is the linear attenuation coefficient of the body tissue (1/cm or 1/mm). Similarly the probability of photons going through the patient in the upward direction is:

$$P_2 = e^{-\int_0^{d-x} \mu(s)ds}$$

Hence if N_0 is the total number of decays at location indicated by the asterisk and N is number of coincident events detected along the LOR shown, then:

$$N = N_0 * P_1 * P_2 = N_0 e^{-\int_0^d \mu(s)ds}$$

Note that the integral is now taken over the whole line segment of LOR going through the body and has the same value for all decays location along this line.

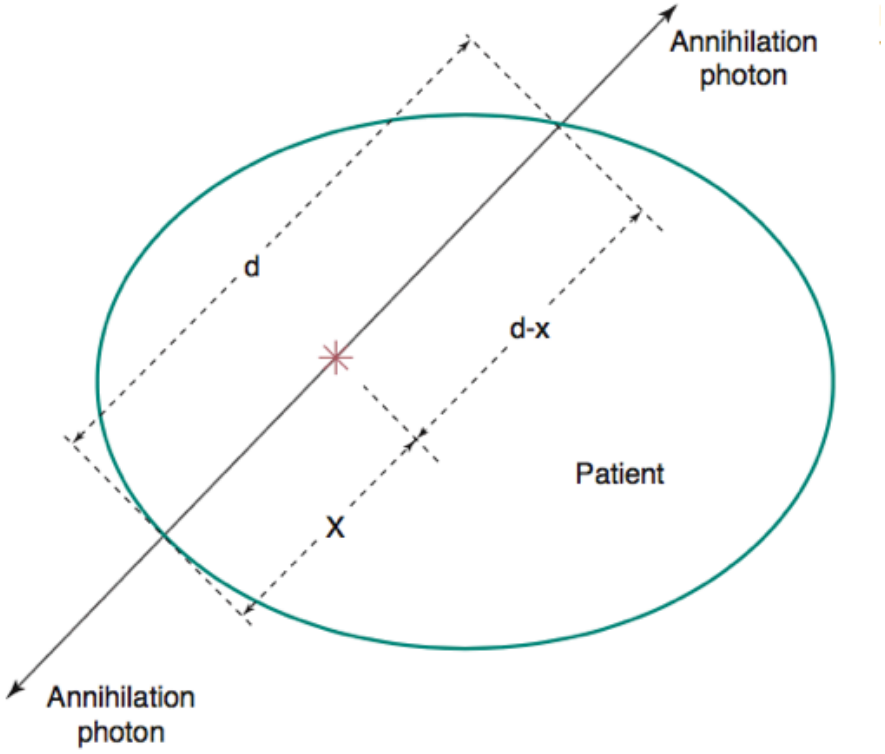

Figure 1.6. Example showing the calculation of attenuation correction.
Attenuation of a coincidence event depends on the total length of the LOR through the object, but does not depend on where the decay occurs along the LOR. Credit to Bushberg [6].

1.4.2 *PET in medical imaging*

PET has extensive clinical use in oncology, and also ample applications in many other fields such as neuroimaging, cardiology and small animal studies. In the majority of cases PET measures a surrogate of cellular metabolic function. ^{18}F-FDG has become the standard radiotracer in PET imaging due to its suited half-life of 110 minutes and relatively clean biological pathway. ^{18}F-FDG (fludeoxyglucose ^{18}F) is a glucose-like synthetic compound with a –OH (hydroxyl) replaced by ^{18}F. It can be taken up by metabolically active cells just like glucose

does, but can not be further metabolized until ^{18}F decays into ^{18}O (while emits a positron). Hence it's a good surrogate for cellular metabolic activity and especially favored by oncologists as a cancer cell tag. After decay, it can be further metabolized just like regular glucose into carbondioxide and water and then be eliminated out of the patient body.

Unfortunately, given the physics of PET, it has one of the highest doses among the common medical imaging modalities. The effective radiation dose of a PET scan ranges between 10 and 20 mSv. In comparison, a non whole-body CT alone is usually in the single digit, and X-ray radiography (such as chest X-ray and mammography) is on the order of 0.1 mSv [13]. Note, for reference, that the natural background radiation exposure is around 3 mSv per year, with geographical and altitudinal variations. [14; 15]

1.4.3 *Breast PET*

Functional imaging has a unique role of detecting changes in breast tumor activity long before the morphological indications. The utility on breast cancer care was first considered in 1994, when Thompson et al. has explored feasibility of positron emission mammography (PEM) [16]. More recent clinical studies focused on the argument that PET-based tracers could be used as a biomarker for early prediction of treatment response for breast cancer. Gebhart showed in a cohort study of HER2-Positive patients that PET was able to identify complete metabolic response as early as in week 2 [17]. Groheux also confirmed the early prediction of outcome using PET in a study of triple-negative breast cancer phenotype [18]. Both studies used ^{18}F-FDG, the most common radiotracer in PET. Other studies also investigated tracers such as ^{18}F-fluoroestradiol (FES), ^{18}F-fluorofuranyl norprogesterone (FFNP), ^{18}F-fluorothymidine (FLT) and ^{89}Zr-trastuzumab, etc. [19–22]

While the majority of clinical studies used the whole-body PET/CT scanner, a number of dedicated breast PET scanners have been (are being) developed over the past decade [19]. PEM Flex Solo 2 from Naviscan is a commercially available device [23]. It consists of two detector heads, each of which resides inside a hollow compression paddle. While the paddles stay stationary during a scan, the two heads move simultaneously inside the paddles from one end to other. One group from Stanford also explored the design of having two planar detectors, using cadmium zinc telluride detectors instead of the regular scintillating crystals [24]. A system from CERN, Clear-PEM, also has two planar detectors in parallel [25]. With the patient taking a prone position, the detector panels rotate around the breast to collect coincidences from full angles. The rotating idea was taken further in the PEM/PET system from West Virginia University, whose detector consists of four planar panels that can rotate around the breast. The system notably also has an integrated biopsy unit [26]. OncoVision in Valencia, Spain designed a full ring system, MAMMI, which consists of 12 PET detector modules [27]. A similar system, Elmammo, with a full ring PET detector developed by Shimadzu in Japan, was cleared for marketing in Japan in 2014 [28]. Like Clear-PEM, both MAMMI and Elmammo require the patient assumes a prone position.

It is not uncommon to see breast PEM/PET systems incorporating other imaging modalities. UC Davis has developed a dedicated PET system with a mini CT for breast imaging, namely DbPET/CT [29]. The CT detector and the pair of planar PET detectors revolve around the breast during the scan while the patient assumes the prone position. At Brookhaven National Laboratory, a PET/MR prototype for breast imaging was developed [30].

1.5 OTHER IMAGING MODALITIES FOR BREAST

1.5.1 *X-ray tomosynthesis*

X-ray tomosynthesis is a promising technique that emerged out of the conventional full field digital mammography (FFDM). It utilizes almost identical hardware but, instead of taking a stationary snapshot, the X-ray source moves along an arc around the breast and takes multiple shots. This results in a 3D reconstruction instead of a 2D projection image. Tomosynthesis has a remarked increase of detection rate than conventional mammography, while only delivering comparable radiation dose [31]. Especially in dense and glandular breast, tomosynthesis far excels FFDM (in both sensitivity and specificity), which suffers from overlaying tissue. Since 2005, the publication count on tomosynthesis in PubMed has taken off by multiple folds [32] and more and more physicians have responded using tomosynthesis in their clinical practice. In 2014, Hardesty et al. reported that 30% of 670 surveyed physicians were already using digital breast tomosynthesis (DBT) and many more were planning in the future [33]. A survey in 2016 shows that almost 80% of the radiologists use DBT now, and a quarter of the users used only DBT (without 2D images) [12].

1.5.2 *Ultrasound*

Ultrasound is 2nd most used breast imaging modality, often prescribed as supplementary screening to regular mammography. Free of ionizing radiation, low cost and easy accessibility make ultrasound a favored choice for screening purpose. It has been shown that combined with mammography, it improved the detection rate up to 4.6 per 1,000 [34]. In practice, many clinics have recommended supplementary ultrasound screening for those with dense breast on which

mammography suffers the most and for those that MRI does not apply. Both traditional handheld ultrasound and automated whole breast ultrasound (AWBU) show similar detection rate [35].

Other specialized ultrasound modalities have also gained research interest, such as US elastography [36], automatic whole breast US and contrast-enhanced US (CEUS), etc.

1.5.3 *MRI*

Magnetic resonance imaging is so far the most accurate breast imaging, achieving sensitivities greater than 90% alone in some cases [37; 38] or higher when combined with mammography and ultrasound [34; 39]. It is a natural first choice for supplementary screening to mammography. But due to the high cost of operation and varying tolerance of the contrast agents, it is only recommended to women with high risk and/or dense breast.

It should be noted that, unlike mammography and ultrasound, MR is also used in treatment selection and monitoring [40; 41].

1.5.4 *Other modalities*

Other imaging modalities may be applied to breast imaging [42], such as SPECT/scintimammography (^{99m}Tc) [43], optical [44], dedicated breast CT, photoacoustic imaging (PA) [45], and thermoacoustics [46], etc.

1.6 MOTIVATION FOR PET/X

The goal of PET/X is not to improve breast cancer detection during screening, but rather yield quantitative measurements on tumor response to therapy. Breast cancer (and cancer in general) inherently possesses a great degree of intratumor heterogeneity and each patient responds differently to the same therapy [47].

A personalized treatment plan is increasingly becoming the key to a satisfactory outcome. Physicians use the window of opportunity before surgery to evaluate the efficacy of the chemotherapy treatment, which usually is the same chemotherapy the patient will receive after surgery. An early evaluation of the efficacy on individual patient's basis will not only save the patient thousands of dollars, but also more importantly, give physicians the chance to try out other treatments if the original one proves to be ineffective. Multiple studies have shown that PET can be an early indicator of the tumor response to therapy. [17; 18; 48–51]

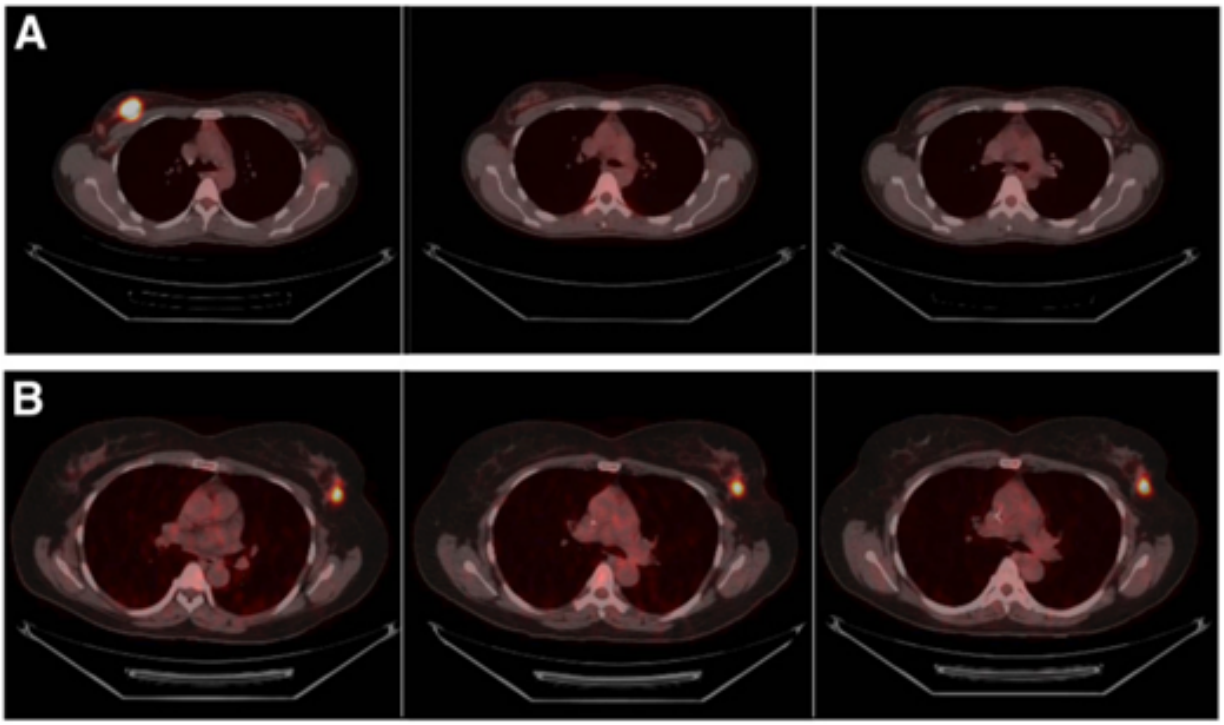

Figure 1.7. PET images showing varying early responses to breast cancer therapy. PET scans of a metabolic responder (A) and metabolic nonresponder (B) in sequential scans of baseline (left), week 2 (middle) and week 6 (right). One can see the drastic change of tumor activity in patient A between baseline and week 2 scans, whereas in patient B, the tumor remains pretty stable, indicating patient B's nonresponse to therapy. Credit to Gebhart [17].

A typical scenario of PET/X application would be during the window of opportunity when the neoadjuvant treatment is applied, as shown in Figure 1.8. A neoadjuvant therapy is usually given as a first step to shrink a tumor before the surgery. Throughout this window of opportunity, multiple PET/X scans could be taken to monitor individual patient's response to specific drugs. A proper evaluation of the neoadjuvant therapy will also help guide the treatment selection in adjuvant therapy after surgery.

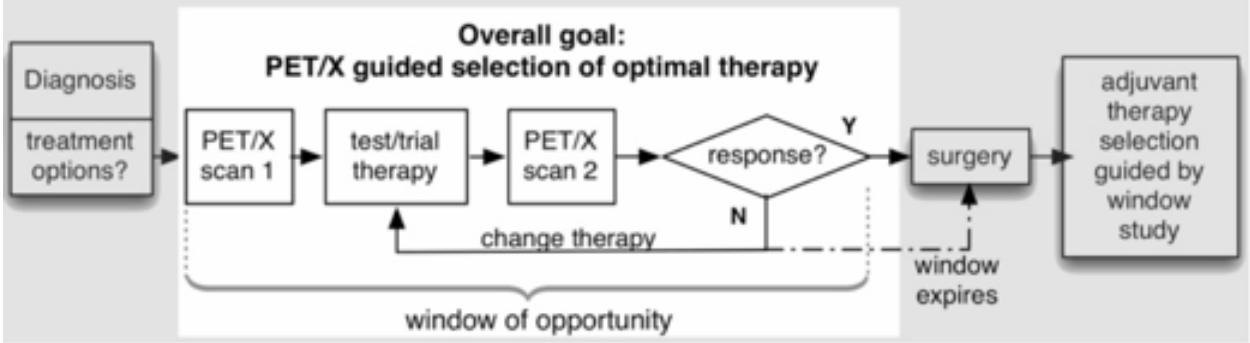

Figure 1.8. Proposed use of PET/X in the standard treatment planning of breast cancer. The PET/X scanner prototype is mounted on a conventional mammography scanner, directly over the planar mammographic detector. The 4 removable panels of PET unit form a rectangular FOV.

The PET/X system was designed with the quantitative target: For a source 5 mm in size with a lesion-to-background ratio ≥ 5, the coefficient of variation will be $\leq 5\%$ for measured activity concentration throughout the scanner field of view. The intended the scan time is 3-5 minutes with no more than 185 to 370 MBq (5 to10 mCi) injections of 18F-FDG.

Chapter 2. THE PET/X SYSTEM

2.1 MECHANICS

2.1.1 *System overview*

The PET/X scanner is designed to be a removable PET unit that works in conjunction with a conventional mammography scanner. It replaces the bucky component and is mounted directly over the mammographic detector. The PET unit consists of 4 planar detector panels that form a rectangular FOV. Upon completion of a 3-5 minute PET scan, the PET detector panels can be removed to make possible subsequent mammography scanning. In between the PET and mammography acquisition, the patient would not need to be repositioned.

Figure 2.1. Prototype of the PET/X scanner.

The PET/X scanner prototype is mounted on a conventional mammography scanner, directly over the planar mammographic detector. The 4 removable panels of PET unit form a rectangular FOV.

2.1.2 *PET unit overview*

The 4 separable panels of PET unit form a rectangular FOV of 240 × 100 × 160 mm. The left and right panels each carries one “trayboard” unit (a composite unit of a detector circuit board, a cooling plate and 12 detector blocks). The top and bottom panels each carries two trayboard units. The top panel has two other vertical resting positions to accommodate different FOVs in the *y* dimension.

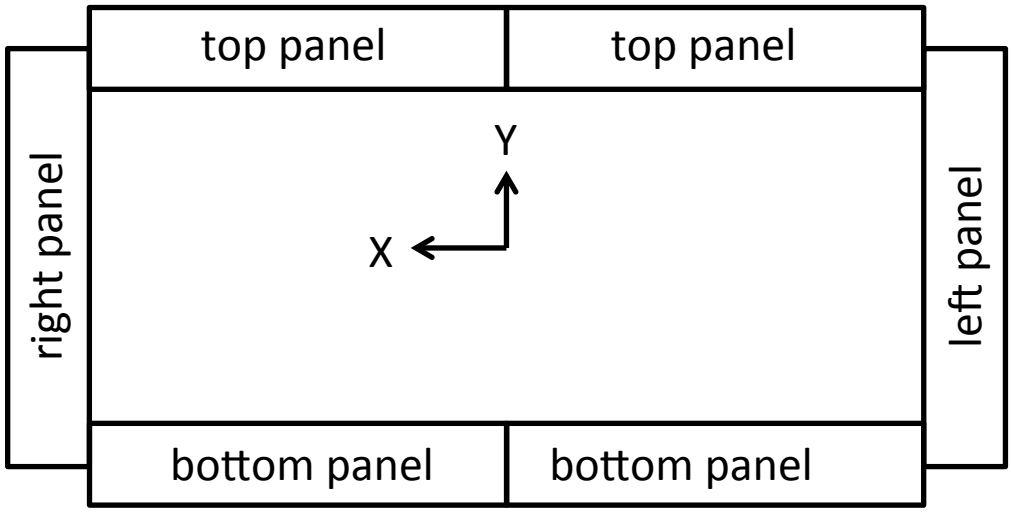

Figure 2.2. Partially assembled PET/X scanner viewed *FROM* the patient's perspective. (Top): As shown in the photo, trayboard units are wrapped in black Tedlar film to avoid photon contamination from ambient room light. The left and right panel each carries 1 trayboard unit, while the top and bottom each carries 2 trayboard units. (In the picture, both top and bottom panels are missing 1 trayboard unit.) (Bottom): Note that, from the patient's perspective, positive *x* direction is pointing to the left, hence the reversed labeling of *left panel* and *right panel*.

2.1.3 *Detector blocks*

Each trayboard unit houses 12 detector blocks in a 4 × 3 arrangement. Each detector block measures 40 × 40 mm in dimension, with a crystal thickness of 10 mm. The LYSO (lutetium-yttrium oxyorthosilicate) crystal is pixelated into a 20 × 20 grid, resulting a pitch size of just under 2 mm considering packaging materials and tolerance. Beneath the crystal is a 12×12 grid of SiPMs that output positional coordinates in the form of (x+, x-, y+, y-). Light guide is applied to assist better optical photon transfer. Each detector block is individually wrapped with black Tedlar film before assembly onto the trayboard unit.

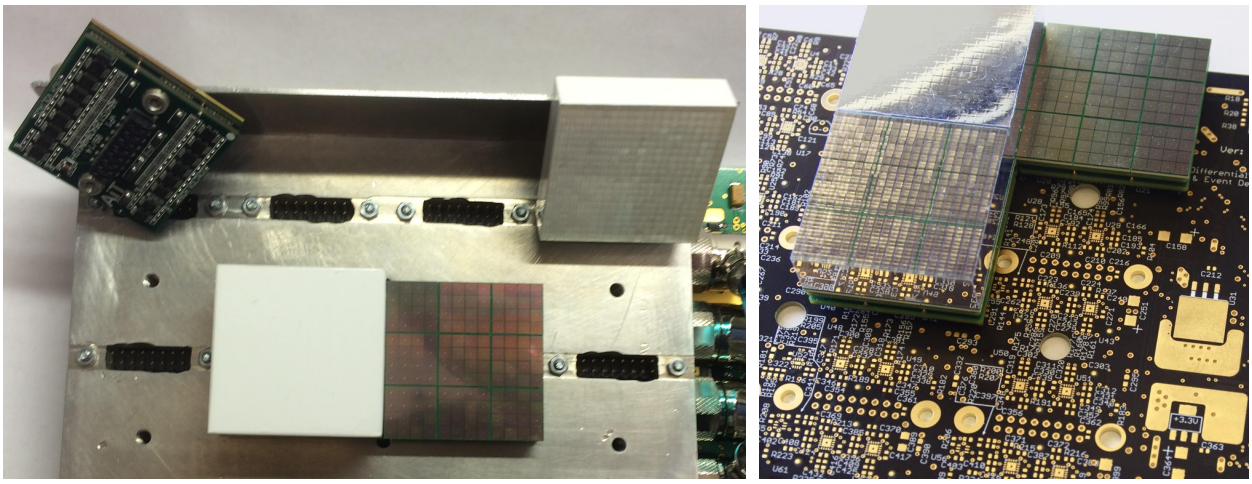

Figure 2.3. SiPM and crystal block.

The SiPM measures 40 × 40 mm and comes in an array of 12 × 12 sensors. On top of SiPM sits a LYSO crystal cut into 20 × 20 pixels, giving a pitch size of just under 2 mm. A total of 12 SiPM/crystal blocks populate a trayboard unit.

2.1.4 *Cooling system*

The aluminum cooling plate is sandwiched by 12 detector blocks on one side and the trayboard on the other side. The whole unit is referred to as a trayboard unit. The whole trayboard unit is secured together by fine screws that go through the trayboard and cooling plate and fasten in the detector blocks. Embedded in the body of the cooling plate is a close-loop tunnel. A centralized cooler pumps the water-based coolant to circulate in the tunnels. The operating coolant temperature is set between 18 to 20 degrees Celsius.

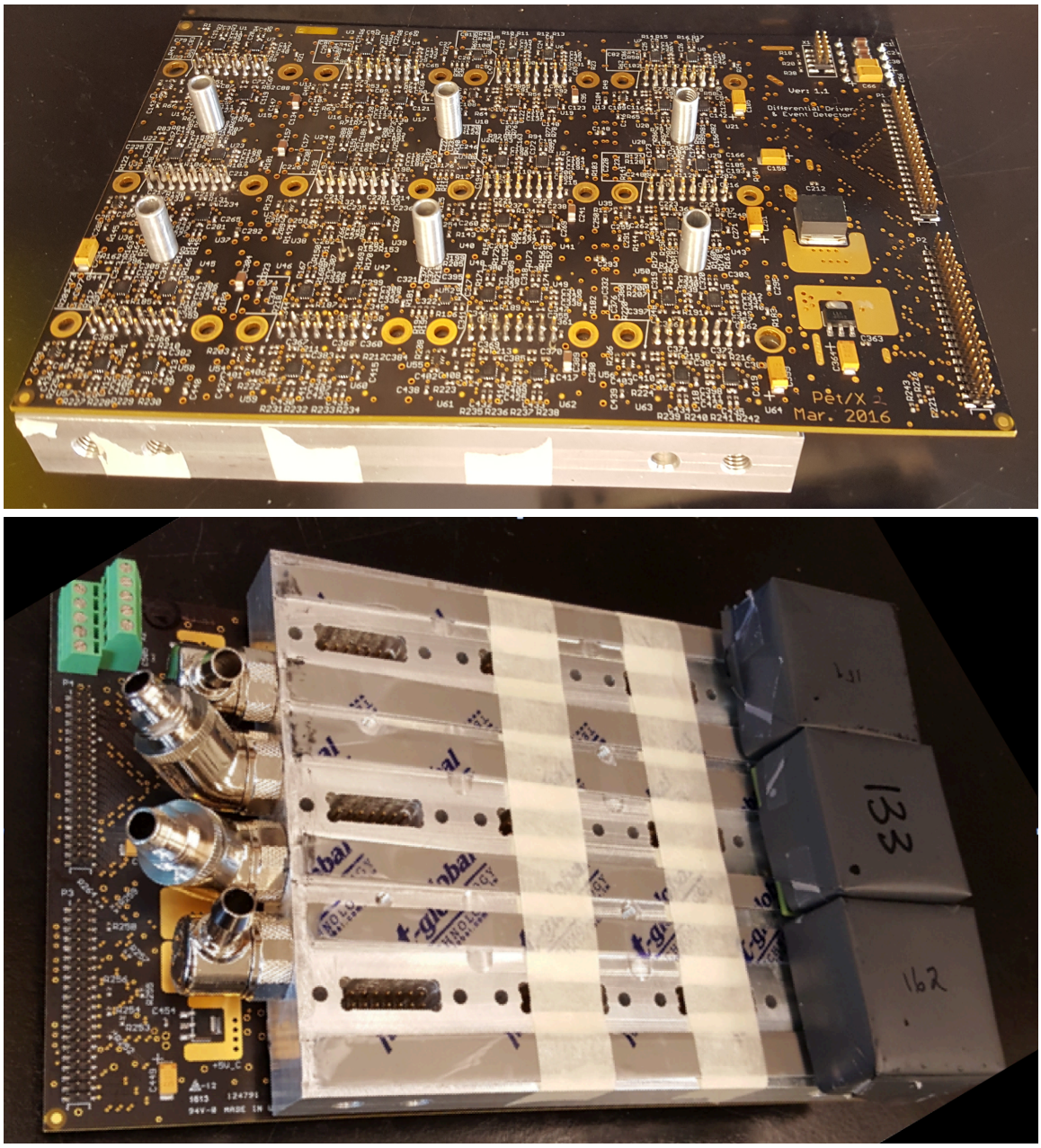

Figure 2.4. Partially assembled trayboard.

(Top): A trayboard unit viewed from the backside. The 6 cylindrical posts that fit in the registration recess holes keeps the trayboard from touching the scanner frame. (Bottom): A trayboard unit viewed from the crystal side. 3 out of a total 4 × 3 crystal/SiPM's blocks are mounted. Adhesive thermal strips are places underneath the SiPM's to dissipate heat to the cooling plate.

2.1.5 *Data acquisition system*

Each trayboard transmits the detected signals via ribbon cables to a corresponding digitizing acquisition (DAQ) board. Each trayboard also has a separate fast channel that joins at a common coincidence board (Figure 2.5). The coincidence board determines the legitimacy of coincidence events and sends the command to the corresponding DAQ board. Each DAQ board then sends the data to computer via a USB 3.0 connection.

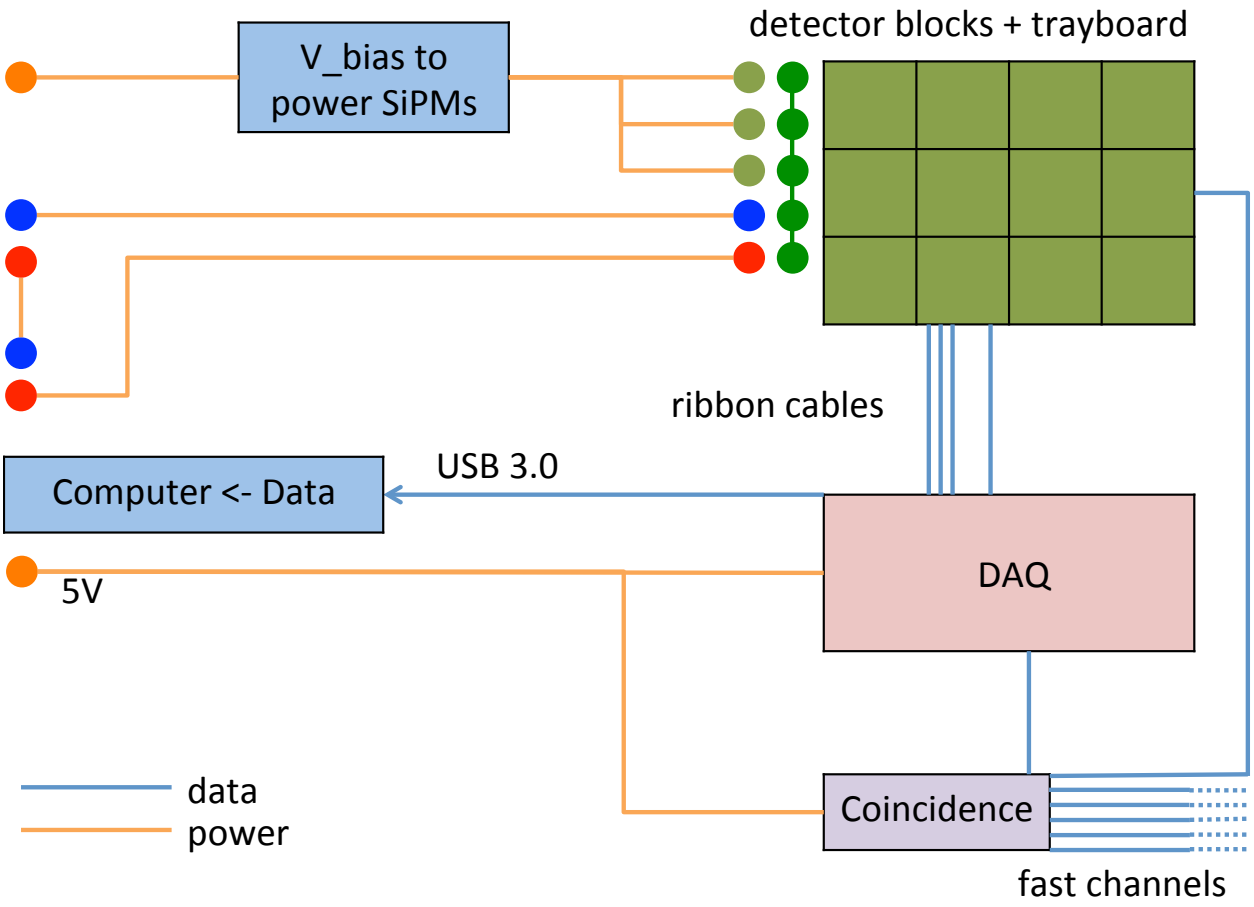

Figure 2.5. Schematic drawing of the data acquisition system.

2.2 DATA FORMATS

2.2.1 *Data flow overview*

The data off the scanner comes in list mode. It then goes through a series of filtering and formatting steps. Here's a summary of all the formats that we have agreed on. They can either exist as an intermediate stage during the data processing chain or be directed as an input/output outlet.

The graph below shows the overview of data flow in both simulation and measurement. The specifics of each data format are detailed in separate subsections.

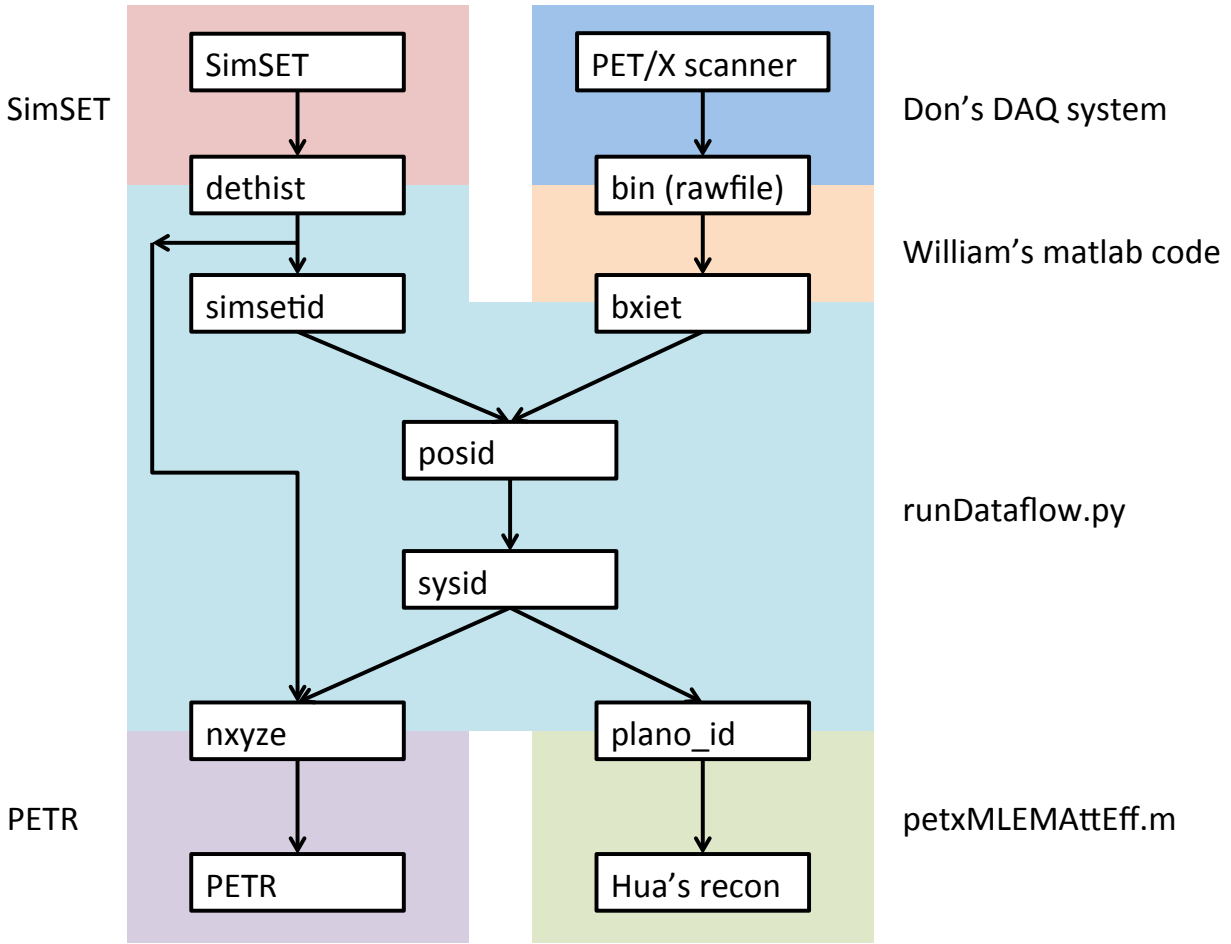

Figure 2.6. Flowchart of various data formats.

This flowchart provides an overview of data formats of the following subsections. The colored background indicate the processing code/environment in which each conversion takes place.

2.2.2 *dethist*

This is the list mode output data from SimSET simulation. The data fields in the *dethist* file are specified by a parameter file. We currently have 2 versions of the *dethist* file format. They are mostly identical, with only a couple differences: the old format lacks *loc_COM* and *simsetid (SimSET_crystal_ID)*. The older parameter file is named *myPET/Xoldformat.paramlist* and the newer one is *myPET/Xnewformat.paramlist*. Shown below is the newer version we are currently using, since it includes the crystal bin indices in the list mode output.

Table 2.2. *dethist* specification

NAME	TYPE	# of ENTRIES	# of BYTES per entry	EXPLANATION
flag_existance	char	1	1	0/1 indicates presence. If 0, then all the following fields are absent.
*loc_COM**	float64	3	8	Interaction centroid: xyz in centimeter
N_scatters	int32	1	4	Number of scatters of this photon in detectors
tot_energy	float64	1	8	Total deposited energy in keV
loc_decay	float64	3	8	Decay location: xyz in centimeter
*simsetid**	int32	1	4	SimSET crystal ID

N_hits	int32	1	4	Number of interactions
loc_each	float64	3	8	Location for each interaction: xyz in centimeter
energy_each	float64	1	8	Deposited energy for each interaction
activeness_each	uint16	1	2	0/1 indicates the activeness of the material where each interaction occurs

*: Data fields only present in *myPET/Xnewformat.paramlist*, but not in *myPET/Xoldformat.paramlist* .

2.2.3 *posid*

The *posid* is an umbrella term of 5 indices: panel_ID (*pid*), tray_ID (*tid*), ring_ID (*rid*), transaxial_xtal_ID (*txid*) and axial_xtal_ID (*axid*). This corresponds directly to the indexing scheme off the PET/X scanner. There are 6 panels: 1 on each side of left and right, and 2 on each side of top and bottom. (Sometimes the panels are referred to as half-panels, or trayboards, as well). Each panel/trayboard consists of 3 trays. Both *pid* and *tid* indexing increase counterclockwise as shown in the diagram (Figure 2.7). Each tray consists of 4 blocks in the *z* direction, indexed as rings 0 through 3 (*rid*). The ring closest to chest wall is indexed 0 (with the lowest *z* coordinate). Within each block, there are 20 × 20 pixelated crystals. The indexing direction of crystals is consistent with the blocks: *txid* follows the direction of *pid* and *tid*; *axid* follows that of *rid*.

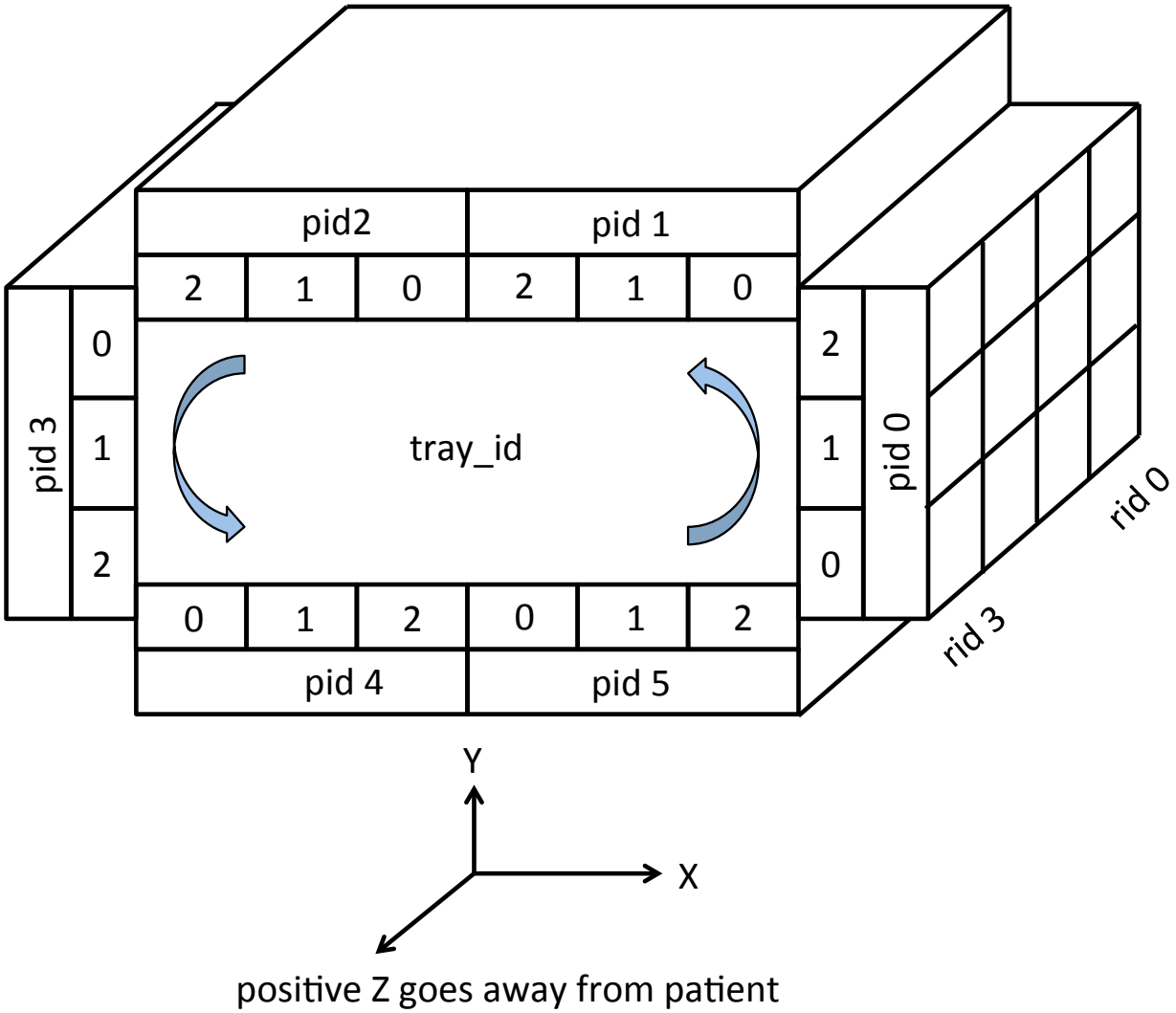

Figure 2.7. Diagram showing the indexing of *posid*.

Note that this is the view *FACING* the patient. The positive *x* direction points to the right and the positive *z* direction comes out of page. All 3 indices *pid*, *tid* and *txid* increase following the counterclockwise direction as indicated by the circular arrows. For *axid* and *rid* indices, a lower index corresponds to a smaller *z* coordinate. Hence the smallest *axid* and *rid* indices are nearest to the patient, and the largest values are nearest to the reader.

Table 2.3. *posid* specification

NAME	TYPE	# of ENTRIES	# of BYTES per entry	EXPLANATION

pid	uint8	1	1	panel_ID: 0-5
tid	uint8	1	1	tray_ID: 0, 1, 2
rid	uint8	1	1	ring_ID: 0, 1, 2, 3
txid	uint8	1	1	transaxial_xtal_ID: 0-19
axid	uint8	1	1	axial_xtal_ID: 0-19

2.2.4 *sysid*

sysid (system_ ID) is closely related to *posid* but from a more macroscopic perspective. That is, the indexing scheme treats the entire system as if the *TOP, BTM, LEFT* and *RIGHT* panels all have uniform bins and ignores the substructure of trays and blocks, etc. We haven't had the need to write out data in *sysid* format, so right now it's just an intermediate step in the processing stream. But it holds the advantage of being more intuitive, straightforward and unifying, and can be potentially used as a storing format in the future. The indices increase in the same counterclockwise direction following the *posid* convention (see *posid* details).

Table 2.4. *sysid* specification

NAME	TYPE	# of ENTRIES	# of BYTES per entry	EXPLANATION
framename	uint16	1	4	4 alias values: *TOP, BTM, LEFT* and *RIGHT**
frameid	uint16	1	4	crystal ID in *framename*: *TOP* or *BTM*: 0-119 *LEFT* or *RIGHT*: 0-49 or 0-59**

zid	uint16	1	4	crystal ID in z direction: 0-79

*: In the current implementation, I picked *LEFT, TOP, RIGHT, BTM* = 991, 992, 993, 994. But these values are customizable as long as sufficient documentation ensues. Better pick unconventional integers so there's little chance of colliding with other variable values.

**: *frameid* for *LEFT* or *RIGHT* could be 0-49 or 0-59 depending on if we want to include the overlapping crystals in the corners. Note that the current FOV is 100 mm vertically and the side panels are 120 mm high. Hence there are 10mm, or 5 crystals, on each ends that overlap with the top and bottom panels. As of now, the reconstruction package by Hua does NOT take into consideration of those corner events, so I rebinned the events to 0-49 on *LEFT* and *RIGHT*.

2.2.5 *bxiet and variations*

Those are the data formats after going through William Hunter's processing code, which does time sorting, coincidence event pairing, energy filtering and windowing, etc. It's designed to be flexible and can have quite a bit degree of customization. The general format is that they start with a 2-byte integer specifying the header length *header_length*. Then in the next *header_length* characters, one can write in plain text whatever the following data format is going to be. The rest of file will follow the aforementioned specification.

bxiet is the first format in this class that we proposed and used to process the acquired data from the PET/X scanner. *bxiet* stands for "board / crystal index with energy and time". Below is one example:

Table 2.5. *bxiet* specification

NAME	TYPE	# of ENTRIES	# of BYTES per entry	EXPLANATION
header_length	uint16	1	2	Number of characters in the header
header	char	1	header_length	A freestyle header specifying the upcoming fields
event_timestamp	uint32	1	1	In 1 millisecond
*N_endpoints**	uint8	1	1	Number of end points per event. Currently set = 2*
1st_energy	uint16	1	2	In 0.01 keV
1st_posid	uint8	5	1	[*pid*, *tid*, *rid*, *txid*, *axid*] See *posid* specification
2nd_energy	uint16	1	2	In 0.01 keV
2nd_posid	uint8	5	1	See *posid* specification

*: So far we've only considered coincidence events of pairs. Hence *N_endpoints* is always equal to 2. In the future we might include triplets and higher orders.

2.2.6 *nxyze*

This is the input format for Kyle Champley's reconstruction code.

Table 2.6. *nxyze* specification

NAME	TYPE	# of ENTRIES	# of BYTES per entry	EXPLANATION
N_total	uint64	1	8	Total number of events
n_blue	uint16	1	2	Number of interactions for the blue photon*. Usually = 1. Can be either the 1st interactions or center of mass

x, y, z	float32	3	4	In cm
energy	float32	1	4	In keV
n_pink	uint16	1	2	Similarly for coincidence photon
x, y, z	float32	3	4	Similarly for coincidence photon
energy	float32	1	4	Similarly for coincidence photon
*LORweight***	float32	1	4	Optional field

*: Restricted to 1 for current implementation. The reconstruction algorithm can be generalized to the case where multiple interactions per events are recorded.

**: It's an optional field per Champley's specification, though I have never had the need to try it, so this field is usually absent.

2.2.7 *plano_id*

This is the input format for Hua's reconstruction code. It consists of 6 pairs of binned data, from the combinatorics of the 4 *frameid*: *TOP, BTM, LEFT* and *RIGHT*. Per Hua's specification, 6 pairs of counts are written into the binary file sequentially in the following order, with no header or separators:

- *'mainpair'*
- *'sidepair'*
- *'righttop'*
- *'lefttop'*
- *'leftbtm'*
- *'rightbtm'*

Please refer to *Image Reconstruction in Rectangular PET Systems Using Distance-Driven Projections* [58] for more implementation details.

Table 2.7. *plano_id* specification

NAME	TYPE	# of ENTRIES	# of BYTES per entry	EXPLANATION
'mainpair'	uint16*	nTop × nTop × nAxis × nAxis	2	*nTop, nSide, nAxis* are the number of bins of FOV in *x, y* and *z* directions.
'sidepair'	uint16	nSide × nSide × nAxis × nAxis	2	
'righttop' and the rest	uint16	nSide × nTop × nAxis × nAxis	2	

*: Some older files used *uint32* for the smaller FOV simulation (200×80×150 mm), but it proved to be problematic for the larger FOV (240×100×160 mm), so now it's set to uint16. It is also consistent with the data type used in the reconstruction code in MATLAB (*single* instead of *double*). If there's any confusion, it's pretty easy to figure out the data type from the file size since the "planogram" dimension is fixed given a scanner specification.

2.3 RECONSTRUCTION ALGORITHMS

Two separate packages of reconstruction algorithm have evolved out of the PET/X project, and they are continuously being improved. At the time of writing, it has not been decided which package will be ultimately deployed on the PET/X scanner.

2.3.1 *Hua's reconstruction package*

The first one, developed by Qian Hua, a former GE employee at GE Global Research Center, features Distance-Driven projectors and iterative updates using Maximum-Likelihood

Expectation-Maximization (MLEM). The code is all written in MATLAB except the projectors are compiled in C++. It's designed to work with binned coincidence data in a form of "planogram", which is a *struct* consisting of the following fields and dimensions:

- *'mainpair':* nTop × nTop × nAxis × nAxis
- *'sidepair':* nSide × nSide × nAxis × nAxis
- *'righttop':* nSide × nTop × nAxis × nAxis
- *'lefttop':* nSide × nTop × nAxis × nAxis
- *'leftbtm':* nSide × nTop × nAxis × nAxis
- *'rightbtm':* nSide × nTop × nAxis × nAxis

where *nTop, nSide* and *nAxis* are the number of bins along the FOV's width, height and axial depth. The first two pairs are also collectively referred to as *linograms* and the last four as *orthograms*.

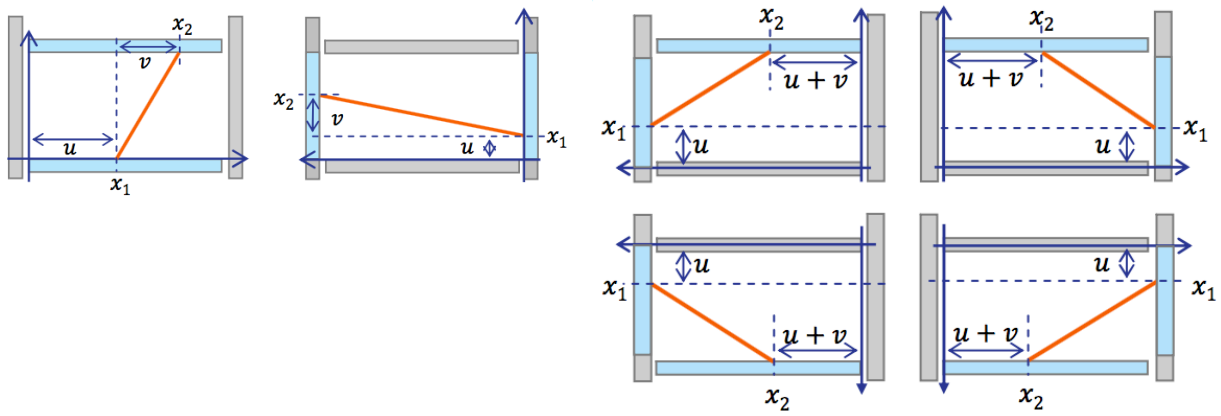

Figure 2.8. Diagrams showing the binning of 6 pairs of coincidences.

Shown in Figure 2.8, x_1 and x_2 are the native crystal bin indices. They are transformed to the planogram indices *u* and *v* by the following relations:

$$u = x_1$$

$$v = x_2 - x_1 \qquad (x_2 \geq x_1)$$

$$v = x_2 - x_1 + N \qquad (x_2 < x_1)$$

where x_2 = 0, 1, 2 … N-1. For linograms, N = *nTop*, and for orthograms, N = *nSide*.

Same procedure will be done on z_1 and z_2 to yield *s* and *t*, where z_1 and z_2 correspond to the *zid* in the *sysid*. The planogram is then indexed using *(u, v, s, t)* for each *field* in the *struct* in MATLAB.

Once the data is binned into planogram, the iterative updates follow the MLEM algorithm:

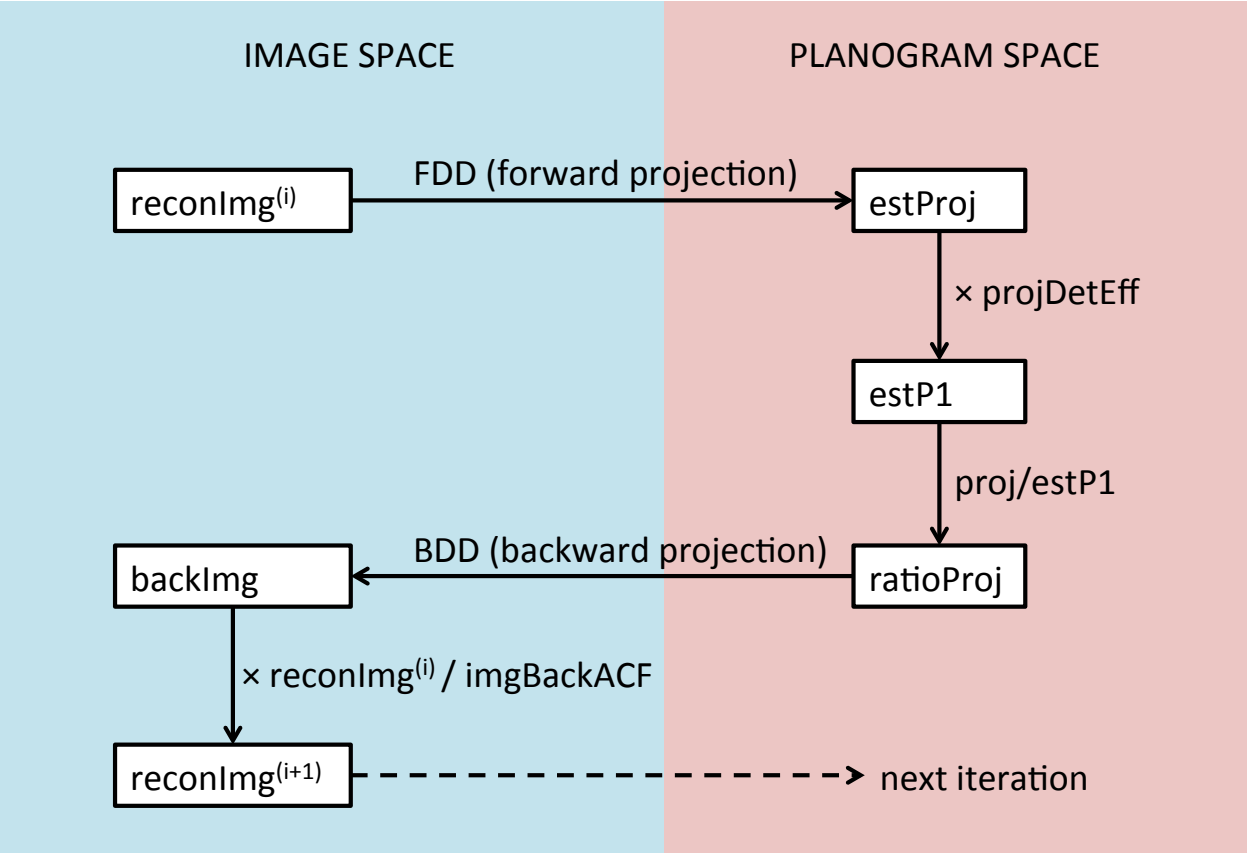

Figure 2.9. Schematic workflow for iterative reconstruction.

In the first flow chart, *proj* is the binned data in planogram *struct* format, and *reconImg* is the output. *reconImg*$^{(0)}$ is usually seeded with a uniform block of 1's. Two options for correction

files are available: *imgBackACF* for attenuation purpose and *projDetEff* for crystal penetration correction. The former is dependent on each phantom, and the latter is specific only to the scanner setup. *imgBackACF* is calculated from the attenuation map *muImg*:

Figure 2.10. Schematic workflow of obtaining *imgBackACF*.

A caveat! If there's no attenuation, then *muImg* = 0. That means *projPL* = 0 and *projACF* = 1. But beware that *imgBackACF* is NOT uniform 1's or 0's. Another caveat is that much of the internal calculation of Hua's code is using float numbers of format *single* instead of the MATLAB default *double*, for example *projACF*. A sample of the cross sections of *imgBackACF* with no attenuation is shown below:

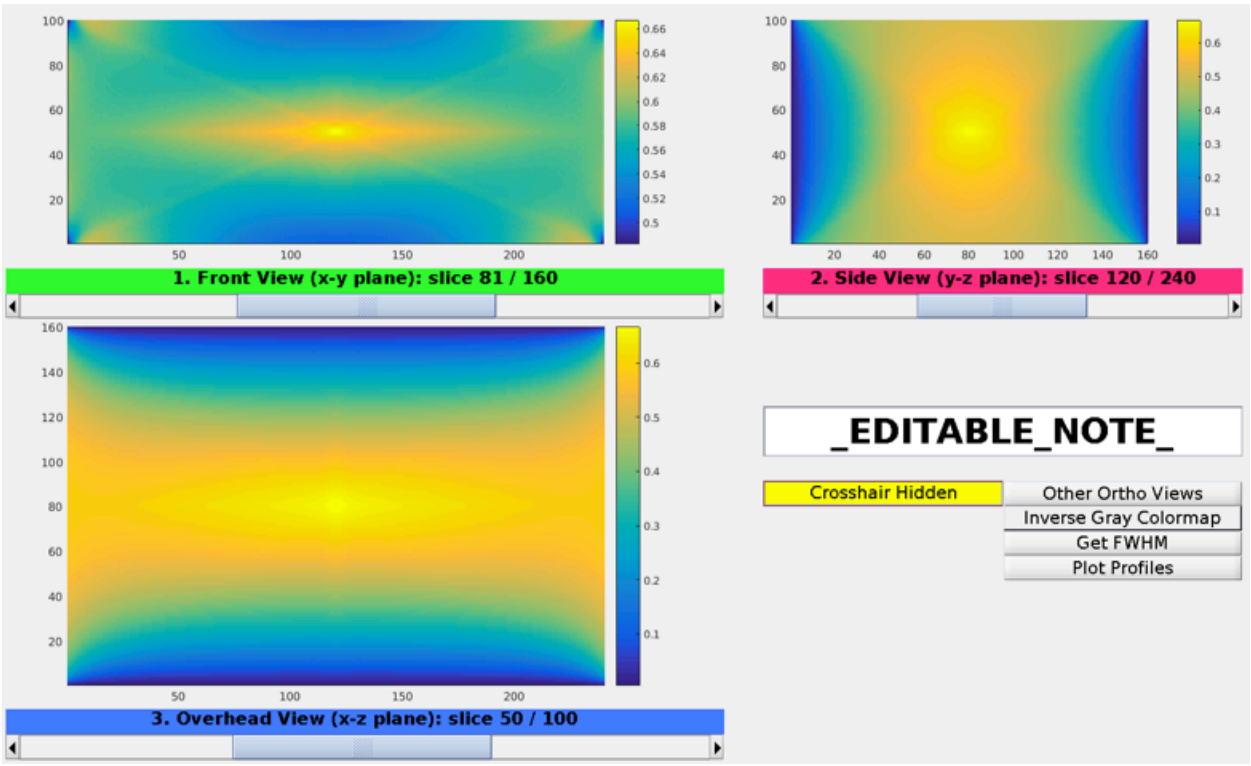

Figure 2.11. *imgBackACF* for reconstruction when no attenuation was simulated. Image displayed by *viewer3d.m*, a customized image viewer for 3D matrices. 3 cross-sectional views are displayed. This viewer is used through out this document for displaying volumetric images.

2.3.2 *PETR*

The second reconstruction package was developed by Kyle Champley, a former lab PhD student and currently a research scientist at Lawrence Livermore National Laboratory. It features Separable-Footprint projectors and two options for reconstruction (analytical and statistically-based iterative). For the iterative one, it uses Penalized Weighted Least Squares algorithm; for the filter-back projection, it uses Planogram Frequency-Distance Rebinning Exact (PFDRX) based on his PhD work.

The input file is in list mode following the *nxyze* data format as described in the previous section. Rather than binning the list mode data separately outside the reconstruction package, it

equips an internal binner function that bins the data into horizontal and vertical detector pairs (*plan_0* and *plan_90*).

Per Kyle's documentation, implemented data corrections include:

- Solid angle correction
- Attenuation correction
- Variable crystal penetration correction
- Optional weighted list mode data
- Optional multiplicative correction from a file

The following are not implemented:

- Detector blur
- Scatter correction
- Randoms correction
- Detector sensitivity
- Dead time and pulse pileup correction

Chapter 3. SIMULATION TOOLS

Simulation plays an important role in research and is an essential tool in product development as well. Through simulation we obtain estimates of some measurement, which we can then use to revise and improve the initial design of the apparatus. We can artificially include or exclude certain physical effects to see how much impact such process would have on the output metric. Simulation is also commonly used to select preferred parameter values when direct measurements are not convenient or feasible. Since the infant stage of the PET/X project, simulation has been an integrated and indispensible component throughout prototyping and model evaluation process. In this chapter I'll describe two major reconstruction packages that I use heavily. CatSim is modified to simulate mammography and SimSET is used to generate PET emission data.

3.1 VIEWER3D.M

Since the simulation study involves mostly PET images (3D volumes) and MATLAB doesn't have a handy tool for displaying volumetric data, I wrote my own customized viewer *viewer3d.m*. It conveniently displays three cross-sections in the *x*, *y* and *z* direction. The setup assumes:

- A right-handed coordinate system, with the *x*-axis pointing to the right, the *y*-axis pointing upward and the *z*-axis pointing out of the page.
- The 3 views in the following order:
    1) The front view located in the northwest. It shows the *x*-*y* plane cross-section with a slider on the *z*-axis.

2) The side view located in the northeast. It shows the *y*-*z* plane cross-section with a slider on the *x*-axis.

3) The overhead view located in the southwest. It shows the *x*-*z* plane cross-section with a slider on the *y*-axis.

- The value of the sliders represents the index value on that particular axis.
- Crosshair in each view reflects the slider values in the other dimensions. They are also color-coordinated with the corresponding sliders.

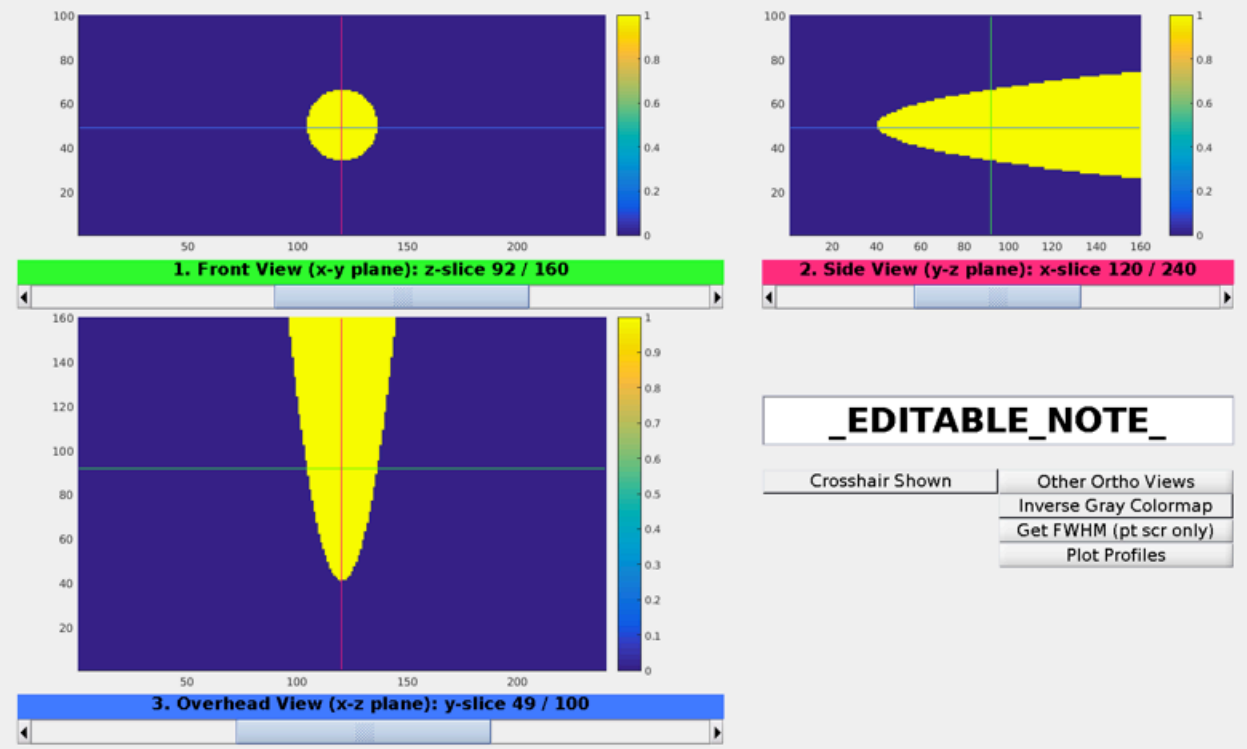

Figure 3.1. Three views of a cone-like object displayed by *viewer3d.m*.

Screenshot illustrating 3 orthogonal views of a sample object. The object has a cone-like shape, with its axis running through the z-axis. In the northwest it's the view of the *x*-*y* plane, hence we see a circle. In the other views we see more of a triangle shape. This viewer is used through out this thesis to show volumetric images.

The viewer takes in a maximum number of 5 inputs: 1 required and 4 optional. Purposely designed, the order of the input parameters does NOT matter.

- Required: 3D image volume. Must be a 3 dimensional matrix.
- Optional: a list of starting indices on the 3 dimensions, shown by the 3 sliders on view 1, 2 and 3. Note that the 3 views correspond to the indices on *z, x* and *y*-axes respectively. For example, [5, 7, 9] means indices [$z = 5$, $x = 7$, $y = 9$]. The default values are [1, 1, 1]. Use [-1, -1, -1] for the 3 views that intersect at the max-valued voxel and [-2, -2, -2] for the min-valued voxel.
- Optional: a list of color limits: [clim_low, clim_high]. It will set the color limits for all 3 views simultaneously.
- Optional: a string of keyword of a color map. It's case insensitive and has to match one of the color maps: 'AUTUMN', 'BONE', 'COLORCUBE', 'COOL', 'COPPER', 'FLAG', 'GRAY', 'HOT', 'JET', 'LINES', 'PINK', 'PRISM', 'SPRING', 'SUMMER', 'WHITE', 'WINTER', 'PARULA', 'default'.
- Optional: a string of notation that will appear on the viewer's *_EDITABLE_NOTE_* box. If a total of 2 string inputs are supplied and both match color map keywords, the first input will be used as color map and the second will be understood as notation.

Once run, a GUI with 3 views and adjustable sliders will pop up. A number of buttons are located in the southeast:

- _EDITABLE_NOTE_: if any notation was passed in as an input, it would be displayed here. The user can also notate directly in the box afterwards.
- Crosshair Shown: toggles between show and hide the crosshairs in the image. The crosshairs are color-coded to the corresponding sliders.

- Other Ortho Views: re-launches another GUI with the axes rotated: *y -> x, z -> y, x -> z*
- Inverse Gray Colormap: toggles between inverse gray and the current color map.
- Get FWHM: so far only works on the image of one point source. It calculates 2 metrics of full-width-half-max and will output the following variables in the current workspace: *fwhm_lin_x*, *fwhm_lin_y*, *fwhm_lin_z*, *fwhm_gau_x*, *fwhm_gau_y*, *fwhm_gau_z*. *fwhm_lin* is calculated with linear interpolation and *fwhm_gau* is calculated with Gaussian fit.
- Plot Profiles: plots the profiles of the 3 crosshairs in the *x*, *y* and *z* axes.

3.2 CATSIM

CatSim is a MATLAB-based CT simulation tool developed by General Electric. I modify it to simulate mammography since both modalities share similar physics. It should be noted that, for a number of reasons detailed later, the mammograms are simulated for the PET/X study only. They are not meant to be real mammogram substitutes, as the noise and scatter properties are not modeled. Special thanks to Pablo Milioni De Carvalho from Buc, France for his generous help. The latest CatSim version I used is v6.03.

3.2.1 *CatSim overview*

- CatSim takes either voxelized or analytical phantoms, handled separately by dedicated projectors. The analytical phantoms are described following the *FORBILD* format in a text file (*.pp*). The voxelized phantoms include a text file (*.vp)* and several data files in binary format (*.VolumeFraction_[material]*). Each data file corresponds to one material in the phantom, with the values indicating the percentage composition of that material in each voxel. CatSim provides a standalone function *catvoxel.m* to convert an analytical

phantom to a voxelized phantom; the *.vp* file and binary data files are generated automatically.

- *catsim.m* is the core function. It simulates a scan and saves the output in a pseudo sinogram file (*.prep)*. The basic steps in *catsim.m* include:
  - Air/offset scan
  - Detector and spectrum setup
  - Read phantom
  - Loop through number of views
  - Within each view, calculate projection and write to *.prep*
- CatSim also provides a simple fast filtered back reconstruction function called *catrecon.m.* It enables a quick check on the simulation result.

3.2.2 *Modification to mammography*

Both CT and mammography measure the transmitted X-rays through the patient object. The scanners therefore share a lot in common when compared to the other imaging modalities. In simulation, the main modifications are done on the detector geometry and the X-ray source.

CT detector is modeled as an ensemble of multiple flat detectors, also referred to as *modules* in CatSim. The modules line along the curved gantry opposite to the X-ray source (Figure 3.2). During a scan, the whole gantry, including the detectors and X-ray source, rotates at a very high speed with a full circle of projections completed in a fraction of a second. Each module is further sub-divided into uniform cells. A cell is the smallest detector element. On the periphery of each cell there can be dead zones made of inactive materials.

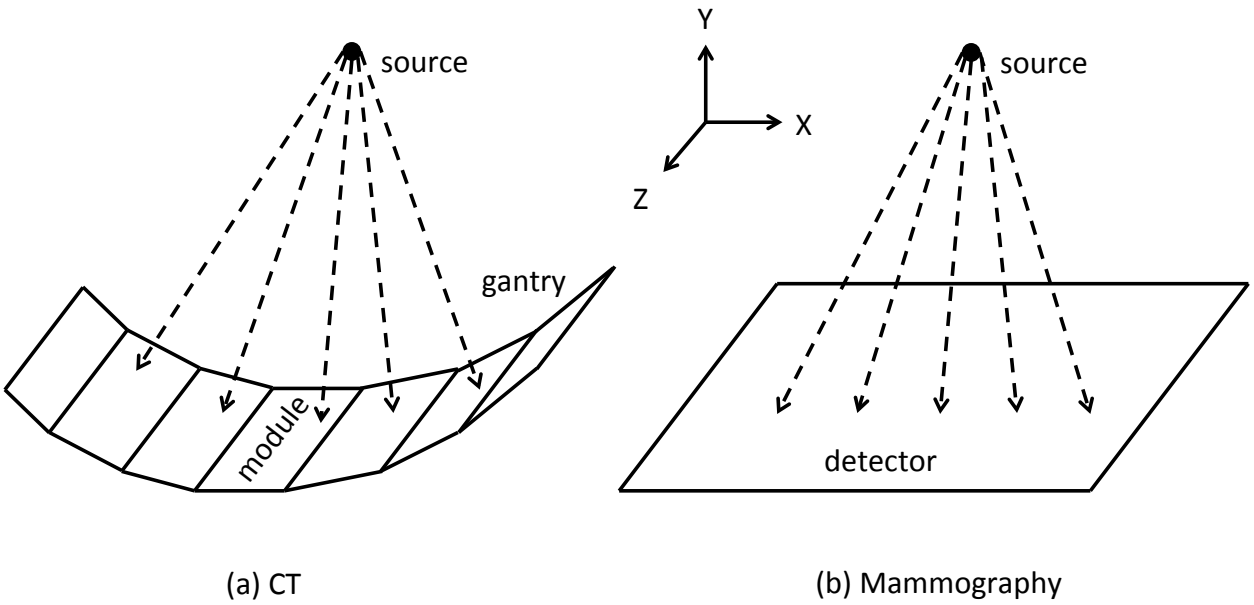

Figure 3.2. Schematic illustration of CT (a) and mammography (b) modeling in CatSim. (a) The CT gantry is composed of multiple modules that line along an arc opposite to the source. Each module is further sub-divided into uniform cells (not shown in the sketch). (b) The planar mammography detector is modeled by selecting only the central module in the CT model and enlarging it to the appropriate size.

Mammography detector may appear very different than CT, but sharing similar X-ray physics makes the modification from CT to mammography possible. We need to specify the number of module to be 1, as mammography is planar, and enlarge it to the mammographic detector size. We also need to set the number of views to be 1. That's basically setting the source and gantry to be stationary. The source needs an offset in the *z* direction, since the mammographic source is directly above the edge, instead of center, of the detector. (Figure 3.2)

CT also has a very different X-ray source. CT spectrum ranges from 70-120 keV and uses a much higher mAs. Because CT X-ray also goes through a much greater attenuation length of the patient body than mammography does, the CT detector receives signals of much more varying intensity between the patient area and the background. In order to reduce saturation on

the CT detector, a *bowtie* filter is placed after the source to pre-filter the X-ray. The name is chosen for its shape of a thinner middle part and thicker ends (Figure 3.3). Mammography, in contrast, does not equip such a filter. Its X-ray energy level and current are much lower compared to CT (generally 30 keV or lower) and the body tissue scanned has a much more uniform composition.

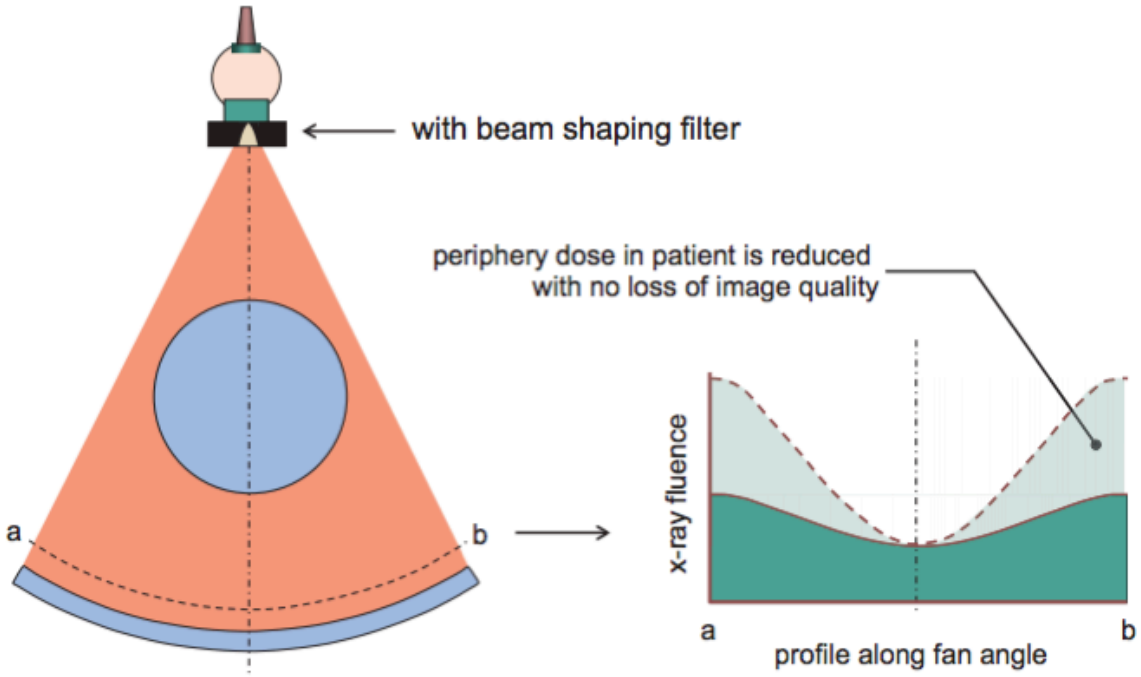

Figure 3.3. Effect of a bowtie filter in CT.
(Left): The phantom object is represented by the blue circle and the CT detector is the blue arc below the object. (Right): Profile plot of the X-ray intensity along the detector arc. Without the bowtie filter (shown as the light green area), one can see that the intensity behind the object is significantly lower than those on the sides (near *a* and *b* ends), due to attenuation of the phantom object. In contrast, with the bowtie filter (shown as the dark green area), the intensity variation is much smaller. Credit to Bushberg [6].

The input configuration files for CatSim (*catvoxel.m* and *catsim.m*) are text files (*.cfg*), but in reality they are MATLAB scripts that will be ran directly. MATLAB compatible syntax is

expected for those configuration files. All parameters are taken in as *fields* in a *struct* called *cfg*. Below is a list of a few parameters for the modification. Note that this is not a comprehensive list.

Table 3.8. A few notable changes (non-comprehensive) to CatSim configuration file

CHANGES	EXPLANATION
cfg.convert_to_prep = 0;	In order to get the raw output *.scan* instead of *.prep*
cfg.compute_airscan = 1;	*.air* is used to correct *.scan*
cfg.sid = 660-30; cfg.sdd = 660;	*isocenter* is where the phantom is centered. *sdd* is usually fixed given a particular scanner, but *sid* need to be adjusted with phantom to ensure the breast sit on the detector surface (not below nor above)
cfg.col_count = cfg.cols_per_mod;	This ensures there's only 1 module. Same with *row_count*
cfg.source_z_offset = - cfg.rows_per_mod * cfg.row_size / 2;	This sets the source directly above the edge of detector (instead of center)
cfg.total_n_views = 1	One projection view only. If tomosynthesis, then it can be greater than 1
cfg.spectrum_filename = 'speXim_Rh30.dat';	Usually either Rh or Mo spectrum file, specific to mammography
cfg.flat_filters = ['rh', 0.025];	Either Mo or Rh.
cfg.bowtie_filename = 'VCTair.txt';	*VCTair* is essentially no bowtie
cfg.callback_gantry = 'Gantry_Tomo';	This is a file from Pablo
cfg.callback_DAS = 'Detection_DAS_Tomo'; cfg.callback_DAS_air = 'Detection_DAS_Tomo';	This is a file from Pablo

cfg.callback_DAS_offset = 'Detection_DAS_Tomo';	

3.2.3 *Other details*

One important physical component we choose to ignore to model is the *bucky*. Unique to mammography, the bucky serves a similar purpose of reducing scatter as collimators do in CT. A fine difference is that the CT collimator is usually fixed in space, while the bucky encloses an anti-scatter grid that moves back and forth at a very high speed in order to blur out the grid lines on the mammogram. Note that in CT, X-rays have higher energy and the FOV is much larger, therefore the fraction of scatter in CT scan is way less pronounced than that in mammography. In fact the previous versions of CatSim didn't even have a feature to model the collimator.

Conveniently, the lack of bucky modeling in CatSim doesn't appear to impose a problem for PET/X, as PET/X is designed to use without the bucky either. In the proposed prototype, the PET unit replaces the bucky sleeve and sits directly over the mammography detector. This is similar to the scenario where a magnification stand is used: when the breast is elevated away from the detector, the scatter is greatly reduced. In the PET/X case, the breast is positioned a few inches away from the detector to make room for the PET detector blocks going in between. Whether or not leaving the bucky out would introduce too much scatter in practice, and how much deterioration it would bring to the final mammogram, remains an unsolved problem that needs to be investigated empirically in the future.

Another feature we didn't model, which isn't available in CatSim either, is the anode's heel effect. Due to the shape and angle of the anode surface, the outgoing x-rays has a varying intensity that is very much angle dependent. In practice, this unevenness is usually taken care of

by a calibration scan during post-processing. Since we are simulating mammograms for the PET/X purpose and are less interested in a complete mimicry of a real scanner, it is reasonable not bother to model the heel effect in the first place.

3.2.4 *Example 1: beam-hardening effect*

Beam-hardening is the phenomenon when polychromatic X-rays go through an attenuating material, low energy photons get attenuated more than the high energy ones. As a result, the average energy of the spectrum increases, i.e. the beam *hardens*. The effect is present in all X-ray radiography modalities, but more pronounced in mammographic spectrum as the energy level is much lower compared to CT. Below is one example of the simulated spectrum of Rh 31 keV, before and after attenuation.

A full comparison of photon transmission property at 511 keV and mammographic energies is included as an appendix to this document.

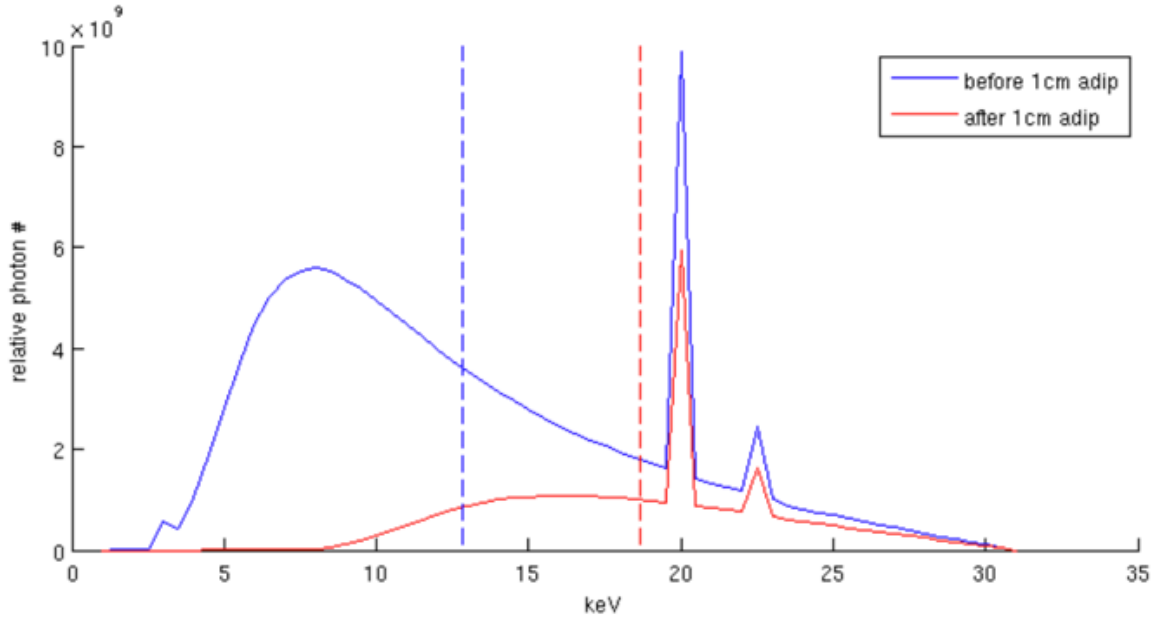

Figure 3.4. Simulated beam hardening.

The figure shows the spectrum of rhodium anode of 31 keV before (blue) and after (red) going through 1 cm of adipose material. One can see that the lower end of the spectrum gets attenuated much more strongly compared to the higher end of the spectrum. Also note the apparent peaks around the characteristic X-rays of rhodium (20.2 keV and 22.7 keV). The dashed lines indicate the average energies of the corresponding spectrum. The average energy increases from 13 keV (blue) to 18 keV (red).

3.2.5 *Example 2: sample mammography images*

In this earlier study of experimenting converting CatSim as a mammography simulator, I used both a physical breast phantom and a digital breast phantom (Figure 3.5). The corresponding mammograms are then compared to give a visual confirmation of the plausibility (Figure 3.6). Pablo Milioni De Carvalho has more tests of numeric validation in a separate document titled *CatSim_Essential_Guidelines.docx*.

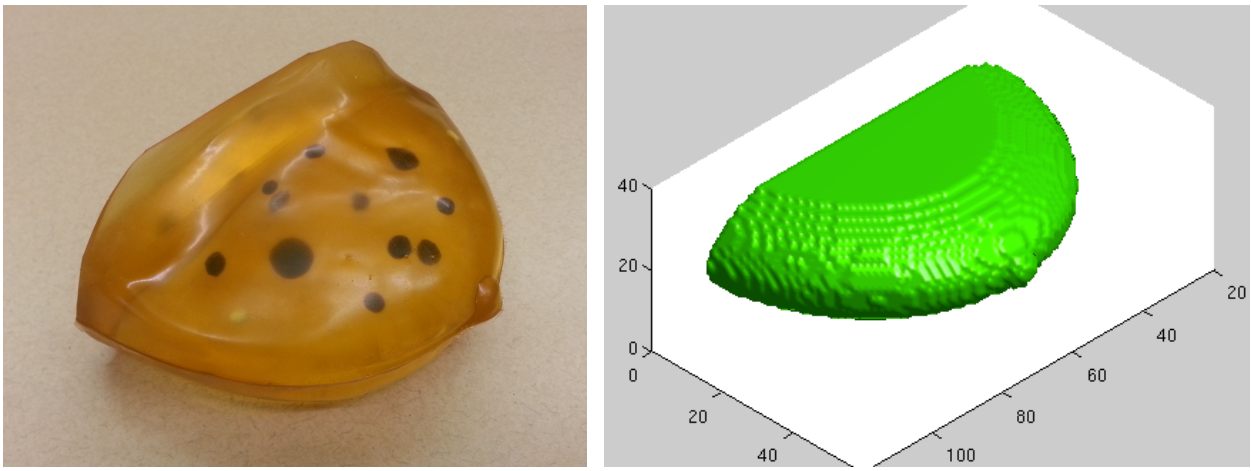

Figure 3.5. Physical and digital breast phantom.
(Left): A standard physical breast phantom with embedded lesion throughout the volume.
(Right): A digit breast phantom for CatSim. It's modeled as a truncated ellipsoid.

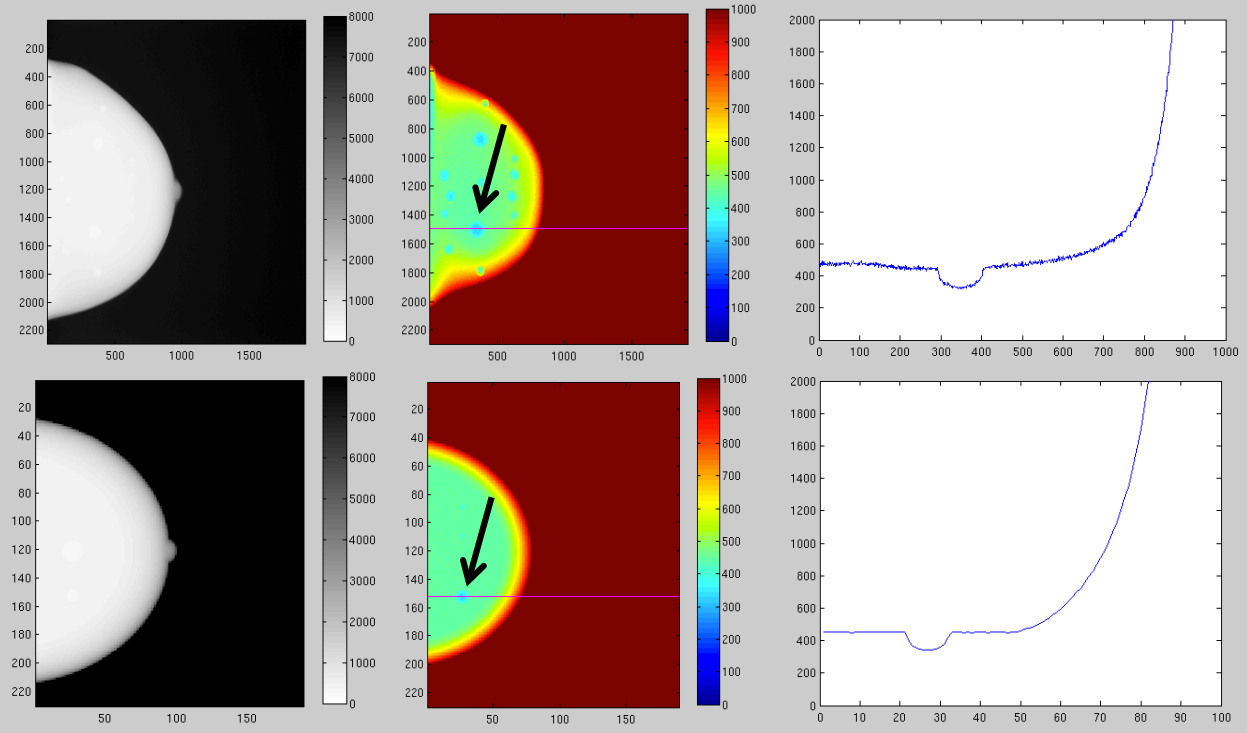

Figure 3.6. Scanned and simulated mammograms.

(Top row): Scanned mammogram of the physical breast phantom. (Bottom row): Simulated mammogram from CatSim using the digital breast phantom. (Left column): mammograms in inverse gray color map. (Middle column): Same mammograms in windowed color range to show embedded lesion, as pointed by the arrow. (Right column): profiles along the red lines shown in the middle column. The pit on the curve corresponds to the tumor lesion as it usually corresponds to the denser tissue than the surrounding breast tissue.

3.3 SIMSET

SimSET (Simulation System for Emission Tomography) is an open source package that "uses Monte Carlo techniques to model the physical processes and instrumentation used in emission imaging". (http://depts.washington.edu/simset/html/simset_main.html). Most of my work involves using SimSET to generate list mode emission data for the PET/X and other scanners. In particular with the unconventional box geometry of the PET/X detector, several crucial

modifications to the source code had to carefully implemented to ensure smooth simulation. This section details the customization steps and shows some visualization results.

3.3.1 *Rational for customization*

SimSET assumes a circular detector layout, as in all commercial PET scanners. The assumption is enforced by the concept of a *target cylinder*, which separates the phantom object and detector blocks. Before each simulation call, SimSET checks to make sure that the object is entirely enclosed in the target cylinder and all detector blocks are positioned outside the cylinder. Doing so guarantees that the phantom object will not overlap with the detector elements. This safety check, however, imposes a fundamental conflict with the PET/X geometry. If we chose a large target cylinder to enclose the full rectangular FOV, we would inevitably include some detector blocks within the target cylinder. Alternatively, if we picked a small target cylinder so that all detector blocks lie outside, we would not be able to include the full FOV. Either choice would result an instant runtime failure (Figure 3.7).

In the past, the workaround has been choosing the largest allowed target cylinder and run several different simulations to recover the rectangular FOV collectively (Figure 3.7). Apart from the inconvenience of dividing and recombining the FOV and phantom and subsequently combining the simulation results, it still has a few unavoidable limitations. For example, it's not possible to cover the entire rectangular FOV with a series of circles. For another, it's not clear how to deal simulations with attenuation since parts of the phantom lying outside the target cylinder have to be truncated at each individual simulation.

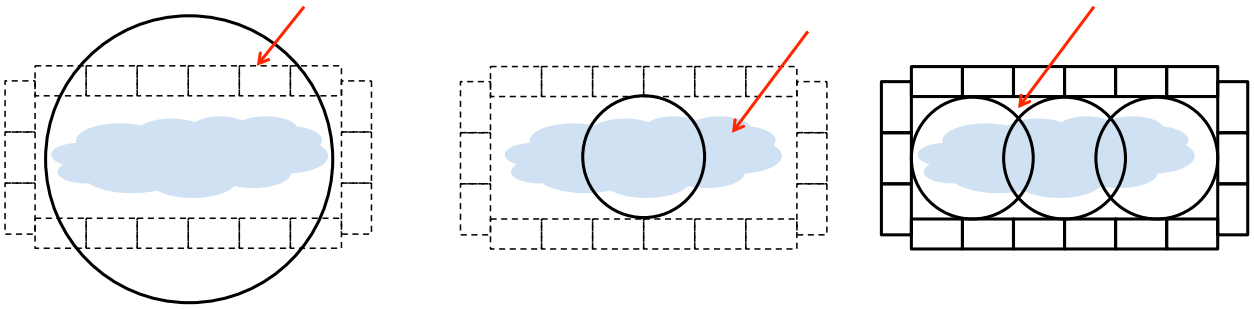

Figure 3.7. Issues with the regular SimSET.

(a): If a large target cylinder is chosen to enclose the entire phantom object, it would unavoidably include some of the detector components, which would fail the SimSET prerequisite check. (b): If a small target cylinder is chosen to avoid including detector components, it may not be able to cover the entire phantom. (c): To somewhat circumvent the restriction, one can use multiple simulations, each with a legitimate target cylinder covering a different part of the FOV with a different part of the original phantom, and then combine the list mode data together. Even though the full phantom can be collectively covered this way, there's still some corners of the FOV that can NOT be covered.

3.3.2 *Overview of customization steps*

To circumvent the target cylinder restriction, I separate a standard SimSET run in two sequential steps and change the target cylinder size half way through the simulation to by pass the prerequisite check.

1) Step 1: set the target cylinder large enough to enclose the entire FOV. Track the photons through the phantom object till they hit the target cylinder. The intermediate list mode data is saved into a binary file for the next step. Even though technically some detector elements are also included in the target cylinder, the prerequisite check doesn't kick in until the detector module is run.

2) Step 2: enable the *Detector User Function* module in SimSET and define a customized function that backtracks photons from the target cylinder onto a virtual rectangular boundary surrounding the FOV.
3) Step 3: change the target cylinder to an artificially small size so that all detector blocks would be lying outside the cylinder. A small phantom that fits within the new small target cylinder is supplied as well to bypass the SimSET safety checks. Resume the photon tracking from the virtual rectangular boundary into the detector blocks. Output the final result in list mode.

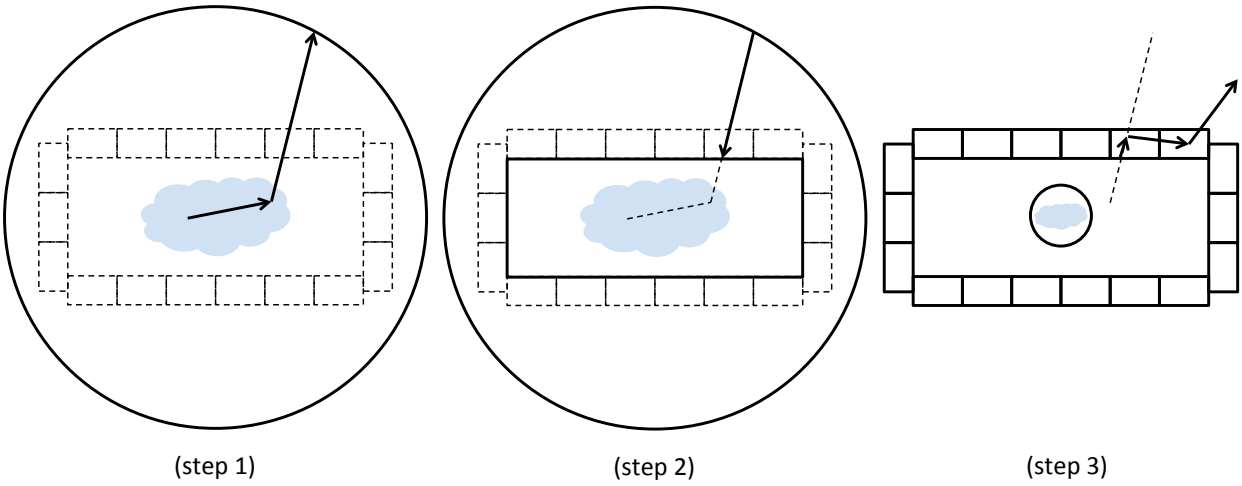

Figure 3.8. Three steps of SimSET modification to accommodate the rectangular FOV. The rectangular blocks represent the location of detector blocks and the circle represents the target cylinder. (Step 1): Set the target cylinder to be large enough to enclose the entire FOV. SimSET will track the photons through the object phantom until they reach the target cylinder. The intermediate result is then saved as list mode data. (Step 2): Customized Detector User Function will backtrack the photons on the target cylinder back to the inner surface of the detectors, shown as the rectangle in solid black lines. (Step 3): Reset the target cylinder to an artificially small radius. Note that we also need to adjust the phantom specification accordingly. Now photon tracking will continue to

proceed into the detector blocks and SimSET will output the interactions as list mode data.

3.3.3 *Work through an example*

The PET/X simulation study has a FOV of 200 × 80 × 150 mm. If we set the center at (*x, y*) = (0, 0), then the maximum distance within the FOV in *x*-*y* plane is Sqrt (100^2 + 40^2) = 107.7 mm. This sets the minimum radius of the target cylinder since we need to enclose the full FOV. I set it at 12 cm. (Figure 3.9)

Note that SimSET uses centimeters.

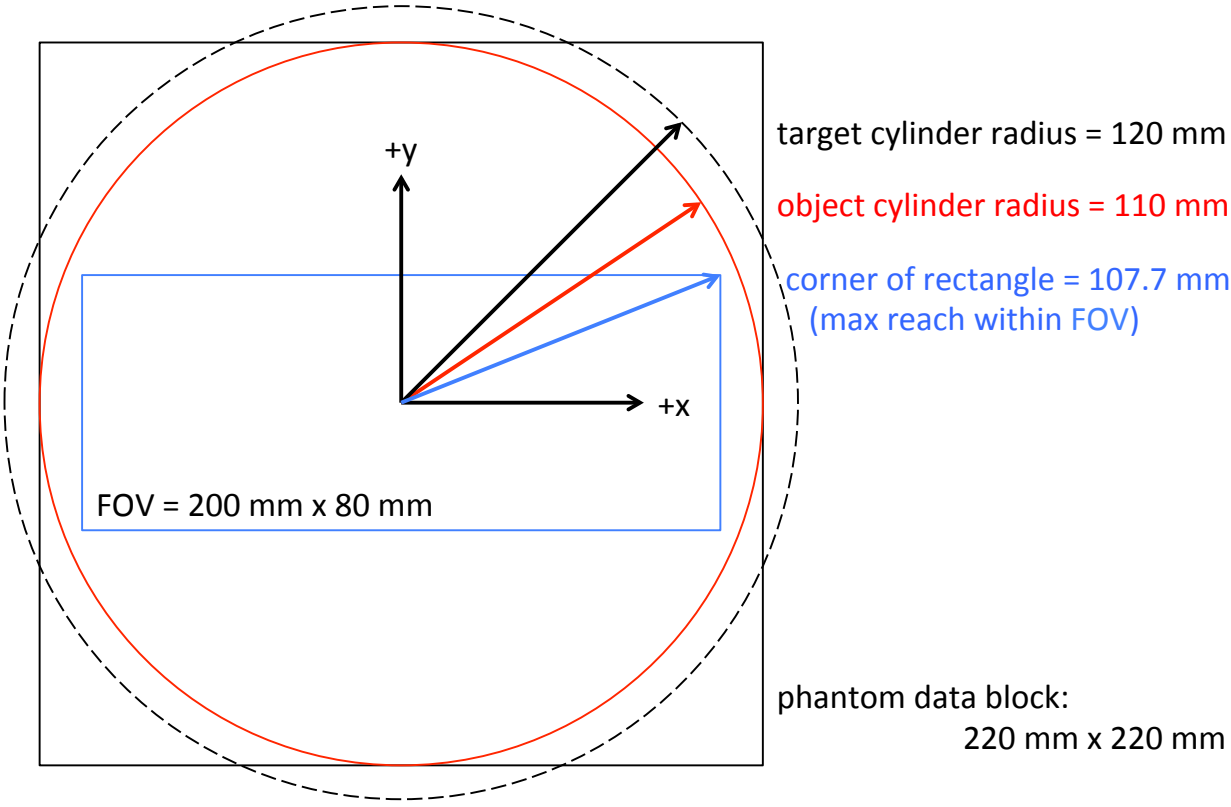

Figure 3.9. Setup for target cylinder, object cylinder and phantom data block.

The maximum distance within the FOV is 107.7 mm and the object cylinder has to at least cover that, and the target cylinder has to at least cover the object cylinder. In

agreement with these constraints, I picked the target cylinder radius of 120 mm. Note the SimSET phantom data block is the square that circumscribes the object cylinder.

In the *z* dimension we need to assign the cylinder length a very large value. (In this case, it's *z_min* = *z_max* = 750 cm) This will ensure that photons emitted from very close to the detector surface can still be captured, as illustrated in Figure 3.10.

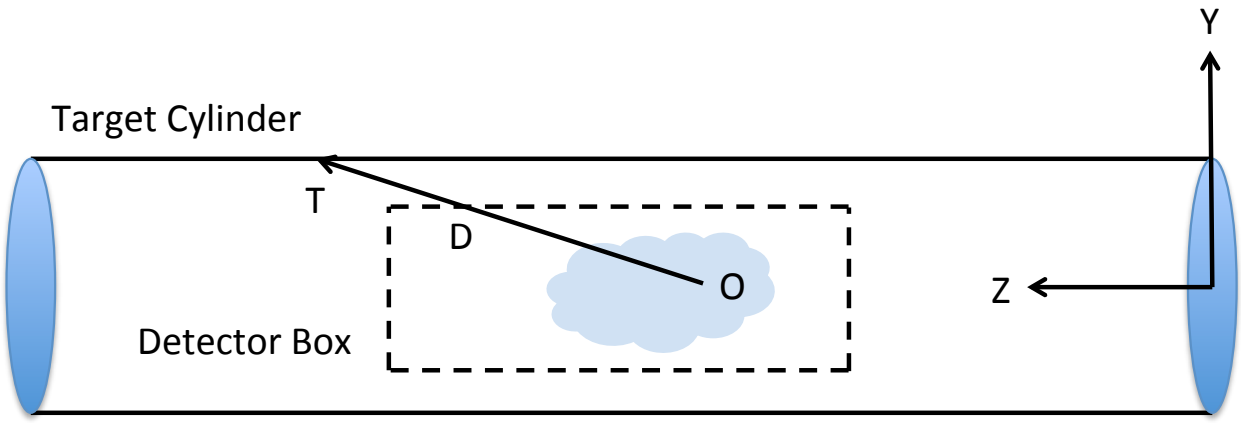

Figure 3.10. Side view (y-z plane) of the target cylinder in relation to the detector box (shown in dashed lines).

A photon from decay point O that hits the target cylinder at point T should be saved because it would go through the PET/X detector at point D. In order to preserve all these photons, the target cylinder should be made a lot longer than the detector length itself. It should be easy to notice that the closer the decay occurs near the detector surface, the more horizontal the photon path could be, and therefore the farther point T can be located.

1) Step 1: there are 2 options to run the photon generator:

- *bin/phg filename.phgin*
- *bin/phg -d 1 filename.phgin*

The optional flag "*-d 1*" enables manual specification of the decay location and photon direction. It's useful for idealized phantoms such as perfect points, lines and

planes, or just about any analytical phantoms if voxelization of the phantom object is not desired. One needs to hardcode the specification in the source code (function *SubObjGenVoxAngCellDecay()* in file *SubObj.c*) and recompile.

The intermediate history file records a plethora of information about the resulted photons that have survived attenuation and scattering in the object and have landed on the target cylinder. The format and name of the output is specified in the *.phgin* file. (In this example they are set as *myPET/X.phghist*)

2) Step 2: the corresponding command is:

   • *bin/bin -p filename.histin*

   The customized user function is run at the very beginning of the detector module. The definition is hardcoded in the source code (function *DetUserPETPhotonsTruncToBox()* in file *DetUsr.c*) and requires recompilation. At the end of the function, the variable *acceptCoincidence* is set to *true* if we wish to keep the photon, i.e. if the photon stored on the target cylinder can be backtracked to the box surface. If so, the photon's location is updated with its new location on the box surface. Otherwise *acceptCoincidence* is set to *false*: the photon will be discarded and not be permitted to proceed to the detector blocks.

3) Step 3: this step follows immediately the user function and does not require a separate command. It records all the interactions of the photon within the detector blocks. The final output is in list mode, whose fields can be customized in a parameter file (*.paramlist*). The name and location of this parameter file is set in the detector parameter file (*.detparams*)

The current format is specified in *myPET/Xnewformat.paramlist* and includes the following fields:

- *Coincidence photon record flag (1 for recorded, 0 for not recorded)*
- *Energy-weighted centroid of interactions (x, y, z)*
- *Number of scatters*
- *Deposit energy in keV*
- *Decay location (x, y, z)*
- *Crystal index*
- *Number of interactions*
- *Each interaction location (x, y, z) and energy*
- *Active or inactive material*

3.3.4 *Notes on important implementation details*

a) SimSET reads in the phantom values from a binary file, i.e. a string of integers. They are then populated to the voxelized phantom space in the following order: first from $-x$ to $+x$, then $+y$ to $-y$ and finally $-z$ to $+z$. Note the reversed order in y direction. In practice it will introduce a flip around the y-axis. It's a known issue to Robert Harrison.

b) In simulation, the decays are also processed one grid at a time, in a particular order. It's incorrect to assume that the decays are randomly sampled from the entire object phantom. Therefore it's always advised to run a batch of mini simulations and combine the results later, rather than to run a giant simulation and divide the result to smaller parts.

c) SimSET requires that the phantom space have the same x and y dimension. If *xMin* and *yMin* are not equal, or if *xMax* and *yMax* are not equal, the SimSET prerequisite check will fail. Pictorially, the phantom lives in a square in the x-y plane. More precisely, the

phantom has to live within the circle that inscribes the square, formally known as the *object cylinder* in SimSET manual. Note that the voxel size in the x and y directions can differ however, so *num_X_bins* and *num_Y_bins* can have different values.

d) After the *phg/bin* command, SimSET will save all the photons that land on the circular surface of target cylinder, but not those on the 2 flat ends.

e) In a realistic simulation the intermediate history file can take substantial storage space, as it contains many more fields than we may even need later. Always a precaution to check and ensure there will be sufficient disk space.

f) The dimension of the virtual box surface in the customized detector user function is specific to the scanner configuration. If one were to run a simulation with a different scanner configuration, there are 3 ways to address that modification. The 1st obvious solution is to alter the source code and recompile. The 2nd way is to add the dimension as additional parameters in the exact same configuration file (*.phgin* and *.histin*) to be parsed by SimSET. It would be a preferred method if one can figure out the parsing section of the SimSET code. The 3rd, which I end up implementing, is to pass in the dimension in a separate text file. I then add in the source code to read the text file and parse the parameters. The advantage of this way is that it's a lot more customizable with my own parsing code. The downside is that one has to keep around an additional input file, which makes code sharing less convenient and potentially confusing. Currently the file is named *simsetCustomInput.txt*. I also put in an output file *simsetCustomOutput.txt* that may store any custom data one wants to write out from SimSET. Currently it's not receiving any output.

g) In the final list mode output, even if one opts for coincident mode only (by setting *simulate_PET_coincidences_only* to *true* in *.phgin* and *.histin*), all *blue* photons will be recorded regardless of their coincidence status, while only the coincidence *pink* photons are recorded. (I refer to the first coincidence photon as *blue* and the second coincidence photon as *pink*.) If the corresponding *pink* photon does not exist, the *coincidence photon record flag* in the list mode output will be 0. Robert Harrison noted that it was a known (noncritical) issue in SimSET. Therefore one may find many *blue* photons without the corresponding *pink* photons in the binary list mode data and need to discard them later in post processing.

h) In 3.3.2 step 2) and 3), since an artificially small target cylinder is used, we need to make sure the phantom description in *.histin* is also in agreement. In practice, we can keep the same binary phantom file but just set in *.histin* the variables *xMax*, *yMax*, etc be less than the target cylinder radius. Otherwise the phantom may exceed the target cylinder and a runtime failure will ensue.

3.3.5 *Examples of simulation results*

1) As an example to 3.3.4 a) and c), this figure shows plots of decay locations of a 4 × 3 × 2 voxel phantom. The binary phantom file contains the following 4 × 3 × 2 = 24 integers in the exact order (for the comfort of reader's eyes, they are displayed in rows of 4's):

1, 0, 0, 0, (1^{st} slice)

2, 1, 2, 1, (1^{st} slice)

1, 0, 0, 5, (1^{st} slice)

1, 2, 1, 2, (2^{nd} slice)

0, 1, 0, 1, (2^{nd} slice)

1, 2, 1, 2, (2^{nd} slice)

The value in the binary phantom file is proportional to the decay density in each voxel. In Figure 3.11 one can see that the portions of voxels outside the object cylinder are truncated. Any decays occurring outside the cylinder will be voided. Also upon examining the first row (1, 0, 0, 0) in Figure 3.11, we can see that the voxels are populated following an order from –x to +x. However, the fact that the first row ends up in the positive y direction indicates that the voxels are populated from +y to –y. We can also verify that z direction follows the same convention with x direction.

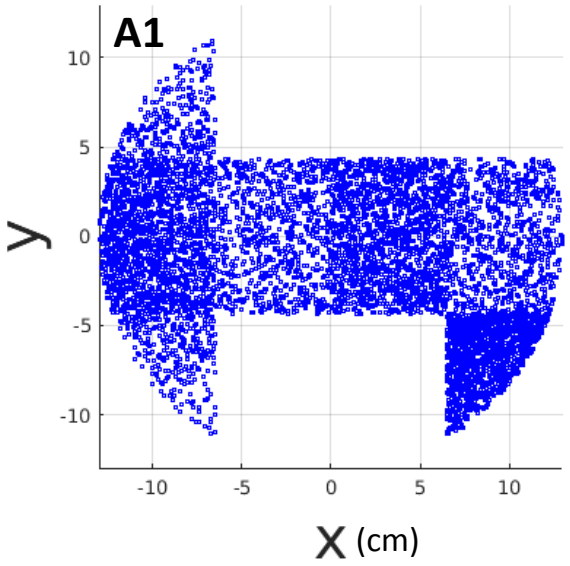

A2

1	0	0	0
2	1	2	1
1	0	0	5

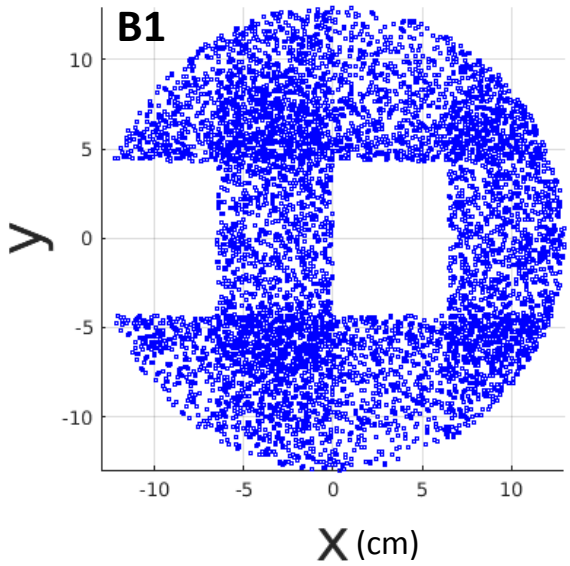

B2

1	2	1	2
0	1	0	1
1	2	1	2

Figure 3.11. Scatterplot of a toy 4×3×2 phantom.

The values in the binary phantom file are proportional to the decay densities in the voxels in the plots. In each plot, there are 4×3 voxels: 4 horizontally and 3 vertically. (A1): Decay plot of the 1st slice. The corresponding values in the binary file are: 1, 0, 0, 0, 2, 1, 2, 1, 1, 0, 0, 5. (A2): The voxelization of the phantom space for the 1st slice. One can see that the values in the table are proportional to the decay densities in (A1). The 0 entries also have no decays in the corresponding locations in density plot. (B1): Decay plot of the 2nd slice. The corresponding values in the binary file are: 1, 2, 1, 2, 0, 1, 0, 1, 1, 2, 1, 2. (B2): Similar voxelization scheme for the 2nd slice. Note that in both (A1) and (B1), the

voxels in the peripheral are truncated by the object cylinder. Also note that the order of populating values in the y direction (+y to –y) is different than that of x and z directions (-x to +x, -z to +z).

2) As described in step 1) in section 3.3.3, it is now possible to have an analytical phantom that's not made possible by using the default voxelized phantom. Figure 3.12 shows two examples, one of a perfect plane source and the other of an artistic arrangement. The plane source is smooth and infinitely thin, and has a potential to be used in PET/X scanner normalization correction. The latter phantom takes form of a cylinder through the z-axis with a cross-sectional shape of a three-leaf clover.

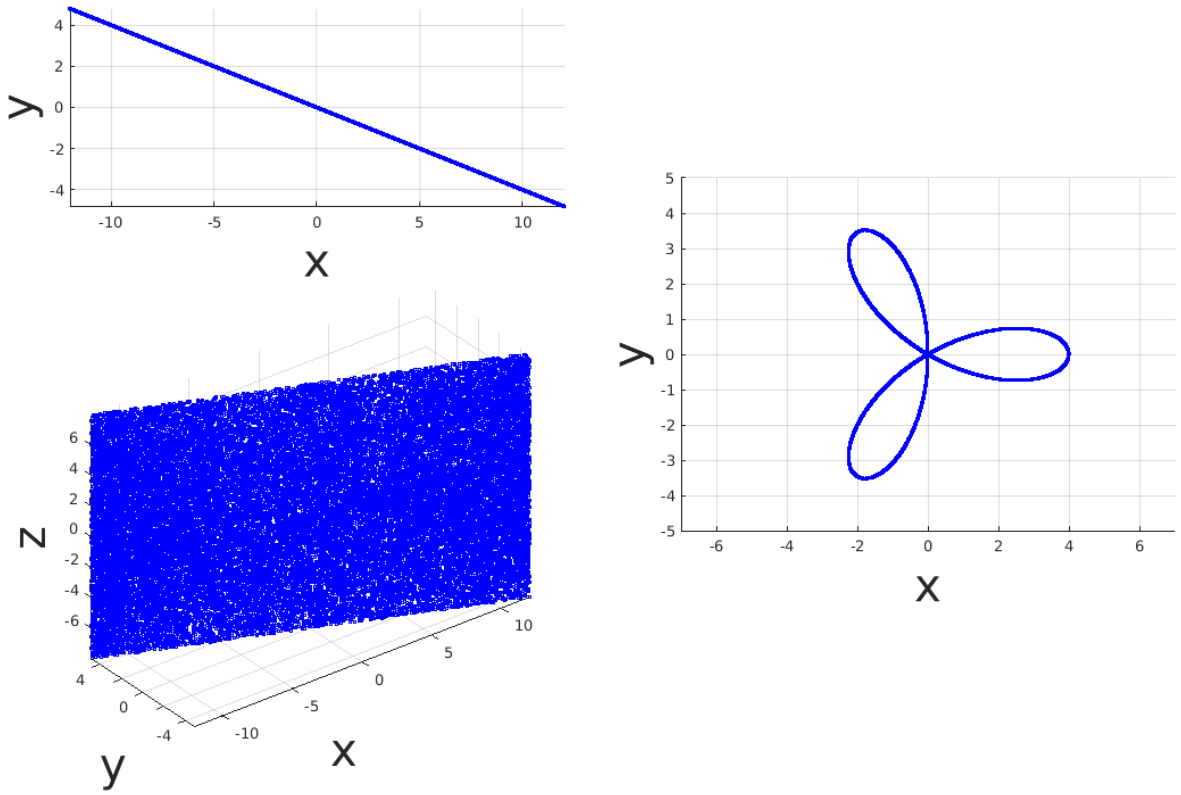

Figure 3.12. Scatterplot of analytical phantoms.
(Left top): x-y view of an infinitely thin plane source connecting diagonally across the scanner corners. (Left bottom): 3D view of the same plane source. (Right): x-y view of an

artistic right cylindrical source through the z-axis. The cross-section takes form of a three-leaf clover.

3) Figure 3.13 shows the interaction locations of photons inside the detector blocks after step 3) of section 3.3.3. One can see that the right side of the scanner receives a significantly higher amount of coincidence events than the left side, due to the placement of the phantom object. The interactions are extracted from the binary output file (*.dethist*).

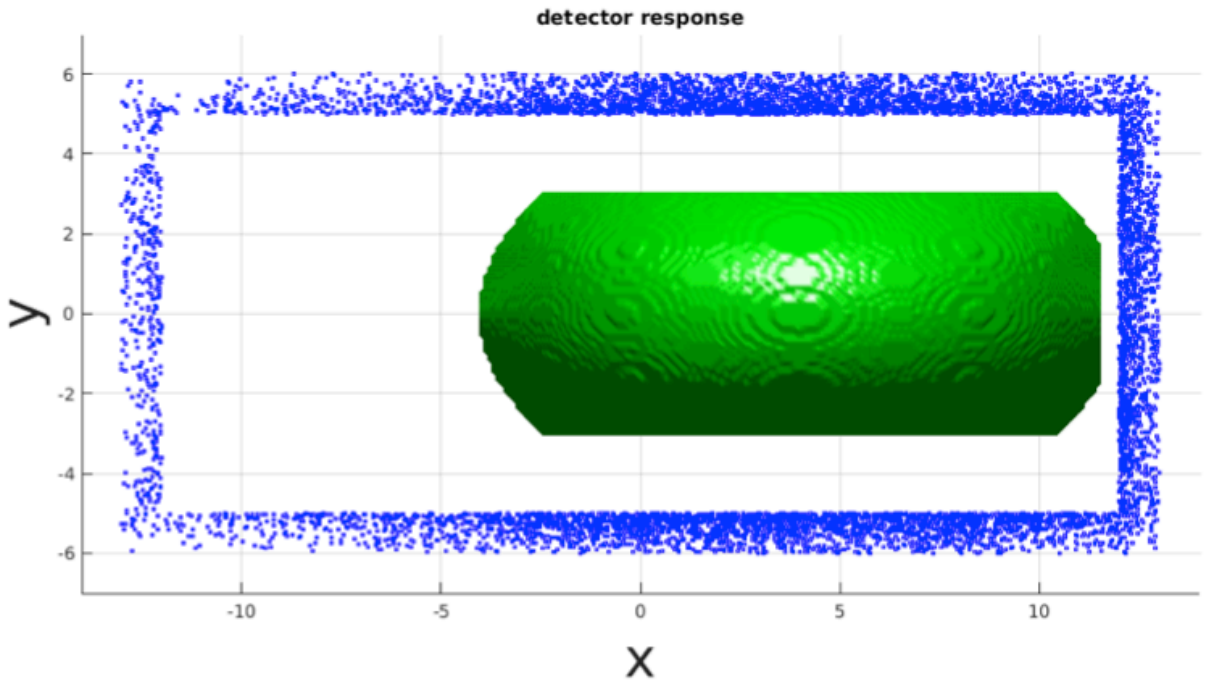

Figure 3.13. Scatterplot of interactions of coincidence events for PET/X.

The interactions of coincidence events (plotted as blue dots) are extracted using the first interaction of the photons. A 3D volume rendition of the breast phantom (green) is also plotted to show the relative position in respect to the scanner. Note this is using the larger PET/X scanner model, with the FOV measuring 240 × 100 × 180 mm and a crystal thickness of 10 mm.

Chapter 4. SIMULATION STUDY OF QUANTITATIVE PRECISION OF PET/X

This chapter is based on my paper [52], with added materials.

4.1 ABSTRACT

The goal for PET/X is measuring changes in radiotracer uptake for early assessment of response to breast cancer therapy. Upper bounds for detecting such changes were investigated using simulation and two image reconstruction algorithms customized to the PET/X rectangular geometry. Analytical reconstruction was used to study spatial resolution, comparing results to the distance of the closest approach (DCA) resolution surrogate that is independent of reconstruction method. An iterative reconstruction algorithm was used to characterize contrast recovery in small targets. Resolution averaged < 2 mm FWHM when using depth-of-interaction (DOI) information. Without DOI, resolution ranged from 2.1 ± 0.13 mm to 3.1 ± 0.42 mm for scanner crystal thickness between 5 and 15 mm. The DCA resolution surrogate was highly correlated to image-based FWHM. Receiver operating characteristic analysis showed specificity and sensitivity over 95% for detecting contrast change from 5:1 to 4:1 (area under curve > 99%). For PET/X parameters modeled here, the ability to measure contrast changes benefitted from higher photon absorption efficiency of thicker crystals, while being largely unaffected by degraded resolution obtained with thicker crystals; DOI provided marginal improvements. These results assumed perfect data corrections and other idealizations, and thus represent an upper bound for detecting changes in small lesion radiotracer uptake of clinical interest using the PET/X system.

4.2 INTRODUCTION

We are currently building the PET/X scanner, which is a breast PET scanner combined with an x-ray mammography system. Our goal for the PET/X scanner is to precisely measure changes in radiotracer uptake after an initial dose of therapy, and to determine correlations between the early changes in uptake and long-term response to the therapy. Based on discussions with radiologists and medical oncologists regarding potential clinical impact, the initial system performance target was that a measured 20% change in tracer uptake in 5 mm lesions with standardized uptake value (SUV) of 5 should correspond to at least 95% specificity (< 5% false positive rate for detecting a true change in uptake). We would like to achieve this performance with 3 to 5 minute scans and no more than 185 to 370 MBq (5 to 10 mCi) injections of ^{18}F-FDG or other radiotracer. Guidelines for using PET to monitor response to therapy have been proposed, for example, the EORTC guidelines [53] and PERCIST [54]. These guidelines are designed for whole-body ^{18}F-FDG PET scanning. In general, the guidelines must carry conditions such as being applied to "evaluable" tumors, which imposes restrictions on tumor size, baseline standardized uptake value, and other factors. Our goal with PET/X is to reduce the size of evaluable tumors to 5 mm. Thus, our scanner design focuses on this performance goal, as opposed to a specific spatial resolution or scanner efficiency. PET/X is designed to be fully tomographic to support quantitative accuracy and precision. Our design uses four flat panels (Figure 4.1) similar to a breast PET scanner previously developed at the Lawrence Berkeley National Laboratory [55; 56]. This design faces similar constraints as other PET scanners, namely, trade-off between spatial resolution and scanner efficiency, and overall system complexity (e.g., measuring event depth-of-interaction (DOI)). This design also faces unique challenges associated with the rectangular geometry, e.g., tomographic data sampling patterns.

The approach and preliminary descriptions of our image reconstruction algorithms have been reported [57; 58]; this paper represents a further assessment of these approaches.

This paper extends our previous analysis of trade-offs in crystal thickness selection [59; 60] by (i) including the use of two independent fully 3-dimensional image reconstruction methods [57; 58], (ii) adding a study of reproducibility through multiple simulation realizations, and (iii) performing a receiver operator characteristic (ROC) analysis of the ability of the PET/X scanner to accurately measure changes in lesion contrast. In this first report of performance metrics from reconstructed PET/X images, we use idealized data models to investigate fundamental upper bound performance limits of the PET/X geometry and image reconstruction approaches. Several physical phenomena important to PET imaging have been omitted for this work in order to focus on sources of fundamental constraints of the detector geometry and reconstruction algorithms.

4.3 METHODS (SIMULATION AND RECONSTRUCTION)

We used the SimSET photon tracking simulation package [61] and two custom image reconstruction packages [57; 58]. The latter two were written specifically for the unique rectangular field of view (FOV) of the PET component.

4.3.1 *Detector description*

As shown in Figure 4.1, the PET scanner consisted of 4 planar detectors, forming a rectangular system with a complete azimuthal angular sampling (around the z-axis). In our study, the top and bottom panels measured 200 mm wide (x-axis) and 150 mm deep (z-axis). The panel-to-panel separation was set at 80 mm. The left and right panels measured 100 mm high (y-axis) and 150 deep (z-axis), with a panel-to-panel separation fixed at 200 mm. Each detector panel was

modeled as one solid piece of 40 mm thick lutetium oxyorthosilicate (LSO). Data were later filtered to keep only events corresponding to certain crystal thicknesses under study, as described in 4.3.3.

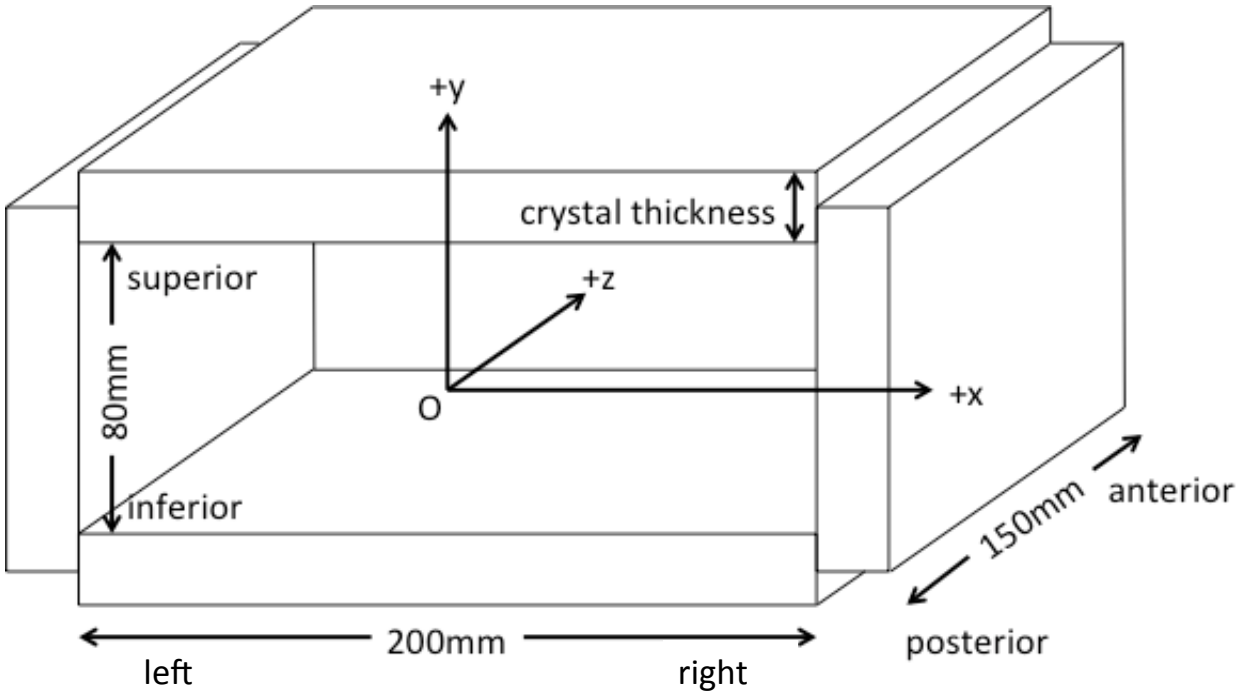

Figure 4.1. Schematic illustration of the PET/X scanner.

The 4 planar detector panels form a rectangular field of view that measured 200 mm wide by 80 mm high by 150 mm deep. Note that the axial view (x-y plane) in PET/X corresponded to a coronal view of the patient.

4.3.2 *Phantom description*

We used a breast phantom that was analytically described as a truncated ellipsoid. Ten same spheres of one of the 3 sizes, 5 mm, 10 mm or 15 mm diameter, were embedded in the breast volume as shown in Figure 4.2. This version of the phantom was used to measure the contrast recovery coefficient. Four spheres were in an axial plane 15 mm from the chest wall edge of the scanner, four were axially halfway, and two were near the nipple region. All ten spheres were the

same size for any given simulated phantom object. The activity concentration target-to-background ratios (TBR) were set to 5:1 or 4:1.

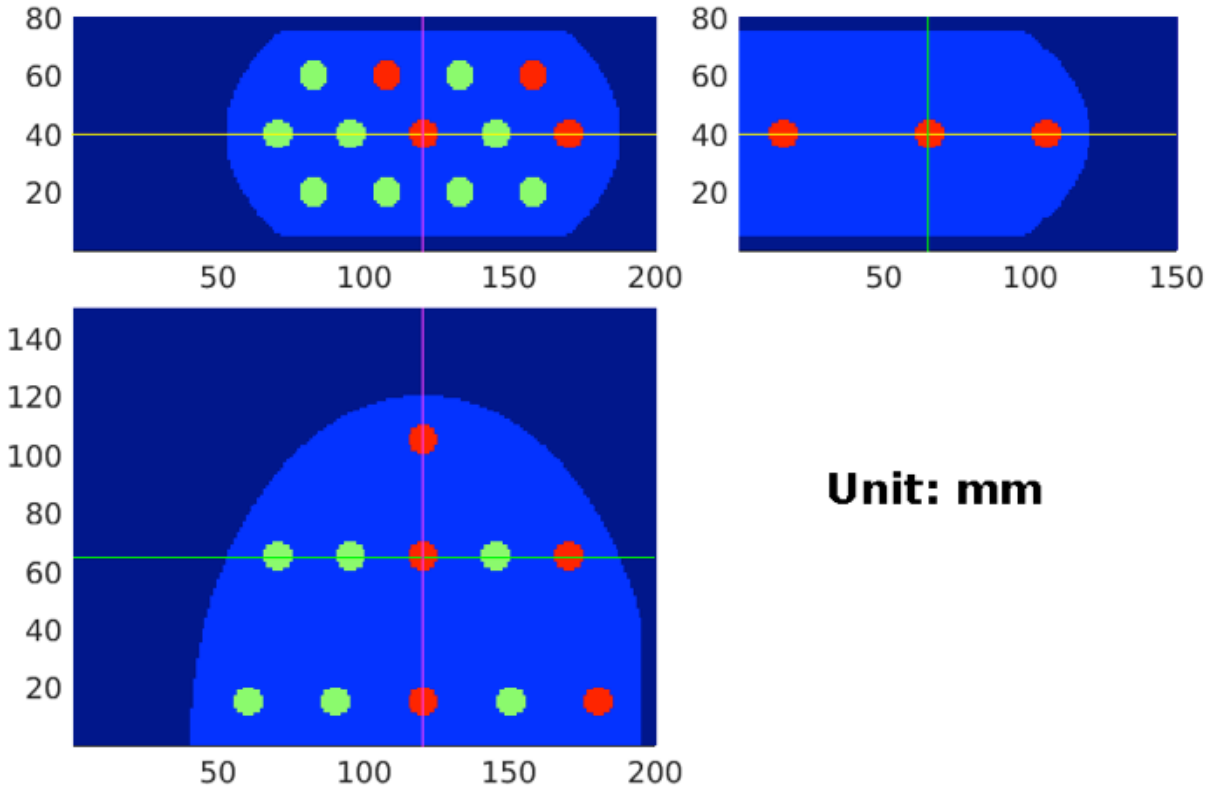

Figure 4.2. Orthogonal views of one sample breast phantom.

Lesions were represented by ten 10 mm-diameter hot spheres (shown in red) and breast background data was taken from distributed spheres of the same size (shown in green). The phantom was voxelized on a 1 mm grid. The image slice shown in each view is indicated by the crosshairs in the other two views. Note that not all spheres lie in the cross-sections shown here. Also note that the axial view (top left) is along the PET/X scanner axis that will be along the patient anterior-posterior direction, and thus corresponds to a coronal view in conventional tomographic orientations.

In separate simulations, the spheres were replaced with idealized point sources at the same locations. This phantom was used to study image spatial resolution. The analytical

phantoms were pixelated into 1 cubic mm voxels, resulting in (roughly) 50, 550 and 1740 total voxels in each of the 5 mm, 10 mm and 15 mm-diameter spheres, respectively. The attenuation coefficient of the entire phantom was modeled to be uniform adipose tissue.

In order to study activity recovery in an object that would not suffer from partial volume errors or resolution loss, we also simulated a 40 mm-diameter hot sphere in a warm uniform background with the TBR set to 5:1. The background filled out the rectangular FOV. The volumes of interest (VOIs) were a 10 mm × 10 mm × 10 mm cube taken from inside the large sphere and another equal-sized background cube away from the sphere.

4.3.3 *SimSET data generation and filtering*

We simulated 500M decays per realization, corresponding to roughly a 3-minute scan with 3 kBq/mL activity concentration for the 900 mL breast phantom. The concentration is representative of a standard clinical FDG dose of 370 MBq uniformly distributed in an 80 kg person after a 60-minute uptake time. Coherent scattering was modeled with perfect energy resolution, while positron range and acollinearity were not. Only true coincidence events were simulated; no random coincidence events were simulated.

To create an object that can occupy the entire rectangular FOV, we had to bypass the constraint in SimSET that required the object and detector to be separated by a cylindrical shell. First, photon pairs were tracked through the phantom object and recorded on an artificially oversized target cylinder. Next, a custom user function was implemented to project the photons back onto the inner surface of the rectangular detector geometry. Finally, the SimSET detector module was used to simulate the interaction location of the annihilation photons within the LSO scintillators.

List mode data, including all individual interactions in the 40 mm-thick crystals, were saved, and post-processing was done to filter interactions that would have been recorded by detector crystals of 5 mm, 10 mm, and 15 mm-thick LSO. This data filtering process was validated in a prior study [59]. The total energy threshold was set at 510 keV to reject scattered events. The remaining interactions were then used to compute the line-of-response (LOR) as detailed below.

Simulations were run separately for the warm background alone, and for the hot spheres embedded in activity-free attenuating background. The list mode data of background and spheres were combined during the post-processing before reconstruction to yield a TBR of either 5:1 or 4:1.

Twenty independent realizations were repeated for each sphere size to allow estimation of the variance.

4.3.4 *Event position estimation*

We modeled event positioning within the detectors in three ways [59]:

1. The 1st-vertex interaction location of the 511 keV photon.
2. The 3-dimensional center-of-mass (3D-COM) of the energy deposited from all interactions.
3. The 2-dimensional center-of-mass (2D-COM).

The 1st-vertex represented the true positioning of the event. In 3D-COM, the energy-weighted COM of all filtered interactions of the same incident photon was calculated to represent the event position. Note that 1st-vertex and 3D-COM were equivalent for photoelectric absorption events (single interaction). The 2D-COM position estimation reassigned the depth-of-interaction (DOI) coordinate of the 3D-COM estimation to a fixed depth for all events. The fixed depth was

calculated as the expected value of the mean penetration depth of 511 keV photons in the incident angle orthogonal to the front crystal face, and thus dependent on the total depth of the crystal thickness. No further detector blurring was added. The data files of 1st-vertex, 3D-COM and 2D-COM corresponded to the perfect LOR, LOR with DOI and LOR without DOI respectively.

4.3.5 *Reconstruction algorithms and image processing*

Two separate reconstruction codes were used. For spatial resolution analysis with the idealized point sources, we used a fast analytical filtered back projection called PFDRX (Planogram Frequency-Distance Rebinning Exact algorithm) [57]. The image voxel size was 0.25 mm.

For contrast recovery coefficient analysis with the sphere sources, we used an iterative reconstruction algorithm that featured distance-driven projector and maximum-likelihood estimation (ML-EM) [58]. We applied 3D-Gaussian post-reconstruction smoothing to control noise and used 15 iterations for all reconstructed images in this study. The image voxel size was 1 mm.

Both algorithms included attenuation correction. In this work we used the phantom itself as the attenuation map to correct the attenuated coincidence data.

4.4 METRICS

4.4.1 *Spatial resolution and Distance of Closest Approach (DCA)*

Images of the ideal point sources were reconstructed using PFDRX with no post-reconstruction smoothing. For each point source, the image-based full width at half maximum (FWHM) in all three dimensions were calculated and then averaged to give a single value per point source.

We also calculated a spatial resolution surrogate, d_{FWHM}, using the Distance of Closest Approach (DCA) method, first introduced by MacDonald et al. [59]. The appeal of the DCA method is that it is independent of the image reconstruction method; here we used list mode data, but it can also be estimated from sinogram data. The DCA is an event-by-event metric defined as the shortest distance from each positron annihilation position to the corresponding line of response (LOR) determined by the detectors. The DCA thus represents the best possible estimate of the annihilation position that the LOR can provide. Of the three event-positioning estimations we described above, events using the ideal 1st-vertex estimate had DCA equal to zero (apart from machine precision with which the list mode data were stored and possible data discretization effect due to object voxelization). The 3D- and 2D-COM LORs were less accurate estimates of the true LOR position, and consequently had DCA greater than zero [59].

Detected events from each point source simulation produced a distribution of DCA values: P_{DCA}. The spatial resolution surrogate, d_{FWHM}, is then defined as the threshold value encompassing some percentage of the events; we used the 29th percentile of the P_{DCA} as follows to define d_{FWHM}:

$$\int_{r=0}^{r=d_{FWHM}} P_{DCA}\, dr = 0.29 \tag{4.1}$$

where the integration (dr) is over DCA values in the distribution P_{DCA}. Our use of the 29th percentile stemmed from the fact that integrating an isotropic 3D Gaussian distribution within a sphere with radius equal to one FWHM of the Gaussian yields 29% of the normalized distribution, as follows:

$$\int_{r=0}^{r=FWHM/2} P_{Gauss}\, dV = 0.29 \tag{4.2}$$

where integration is over the volume of a sphere of diameter FWHM, and

$$P_{Guass} = (2\pi\sigma^2)^{-\frac{3}{2}} exp\left(-\frac{r^2}{2\sigma^2}\right) \quad (4.3)$$

is the isotropic 3D Gaussian (FWHM=2.35 σ). A more detailed explanation of d_{FWHM} calculation and a comparison with measured data can be found in [59].

We hypothesized that the d_{FWHM} should scale proportionally with the spatial resolution obtained in a reconstructed image (with proportionality depending on the image reconstruction and filtering processes, among other factors). We investigated the relationship via the correlation between the image-based spatial resolution and d_{FWHM}: two LOR estimates (3D- and 2D-COM) and three different detector crystal thicknesses (5/10/15 mm) were included.

4.4.2 *Scanner efficiency*

Scanner efficiency was defined as the ratio of the number of accepted events into reconstruction over the number of decays in the phantom. As a first approach to test out our reconstruction algorithms, we used an energy threshold of 510 keV to filter out the scattered events, effectively simulating perfect scatter correction. This gave us a lower bound on the scanner efficiency for different crystal thicknesses.

4.4.3 *Relative contrast recovery coefficient (RC)*

We studied the quantitative precision and accuracy of reconstructed images using the iterative ML-EM algorithm. The relative contrast recovery coefficient (*RC*) was calculated as:

$$(RC_{mean})_{k,r} = \frac{TBR_{image}}{TBR_{phantom}} = \frac{(VOI_{mean})_{k,r}/(VOI_{bkgd})_r}{TBR_{phantom}} \quad (4.4)$$

where k indicates the sphere index, r = 1… 20 are the independent realizations of simulation, VOI_{mean} is the mean voxel value within the target (i.e., sphere) volume of interest (VOI), VOI_{bkgd} is the background mean, and $TBR_{phantom}$ is the true target-to-background contrast in the phantom object (fixed at either 5:1 or 4:1). The sphere VOI used the same voxels as the sphere voxels in the phantom. The background mean (VOI_{bkgd}) was obtained by averaging 9 background spherical samples of the same VOI size as the target spheres Figure 4.2.

RC_{max} was calculated similarly as RC_{mean}, only with VOI_{mean} replaced by VOI_{max}. VOI_{max} is the maximum voxel value within the VOI.

For each configuration of phantom and crystal thickness, we average the $RC_{k,r}$ across sphere indices k and realization indices r to get the mean. We calculated the associated uncertainty in RC using the ensemble root mean square error (ERMSE) with the following definition:

$$ERMSE = \frac{1}{K}\sum_{k=1}^{K} RMSE_k \tag{4.5}$$

$$RMSE_k = \sqrt{\frac{\sum_{r=1}^{R}(RC_{k,r}-\overline{RC_k})^2}{R-1}} \tag{4.6}$$

$$\overline{RC_k} = \frac{1}{R}\sum_{r=1}^{R} RC_{k,r} \tag{4.7}$$

where again, k and r are sphere and realization indices, respectively. $\overline{RC_k}$ is the average recovery coefficient of lesion k among 20 realizations. RC can be either RC_{mean} or RC_{max}.

4.4.4 *Sensitivity and specificity of detecting changes in sphere uptake*

We investigated the sensitivity (i.e., true positive rate) and specificity (1-false positive rate) of detecting a change in TBR and performed a receiver operator characteristic (ROC) analysis for detecting such change. We simulated cases of a pre-therapy TBR of 5:1 and a post-therapy TBR

of 4:1 and calculated associated RC means and variances (ERMSE). Based on the two end point TBR values, we interpolated the RC mean and variance for any intermediate post-therapy TBR value. Using RC_{mean} and ERMSE in an ROC analysis, we estimated the sensitivity and specificity of measuring TBR changes, which is the ultimate clinical task intended for PET/X. We then plotted the sensitivity as a function of TBR drop, given several specificity cutoffs. We also computed the ROC curve for several post-therapy TBR values. The associated areas under the curve (AUCs) were computed.

4.5 RESULTS

4.5.1 *Spatial resolution and d_{FWHM}*

Figure 4.3 shows the correlation between image spatial resolution and the DCA resolution surrogate d_{FWHM} for various detector crystal thicknesses. The correlation was very high with a Pearson correlation coefficient of 0.9167.

The 2D-COM resolution showed a larger variation with respect to the crystal thickness. The 1st-vertex LOR estimate (representing perfect LORs) was not included, because d_{FWHM} was effectively 0, as positron range, non-collinearity effects and detector point spread function were not modeled.

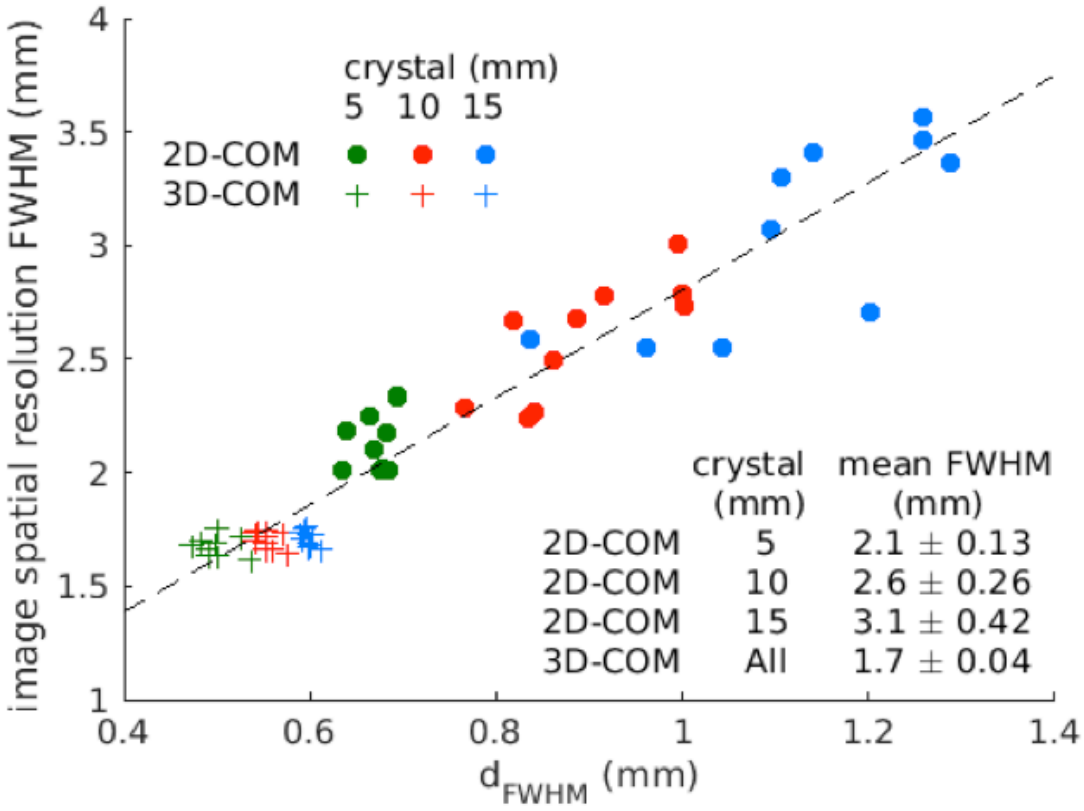

Figure 4.3. Scatterplot showing the correlation between the image spatial resolution using PFDRX reconstruction (vertical axis) and d_{FWHM} derived from DCA method (horizontal axis).

Each data point represents one of the 10 point sources in the phantom for a given detector crystal thickness and LOR estimate method. The phantom consisted of analytical point sources in a uniform background.

4.5.2 *Scanner efficiency*

The scanner efficiency Figure 4.4 for true coincidences ranged from 2% to 18.2% as the crystal thickness increased from 5 mm to 40 mm. With thinner crystals, the dependency was approximately linear.

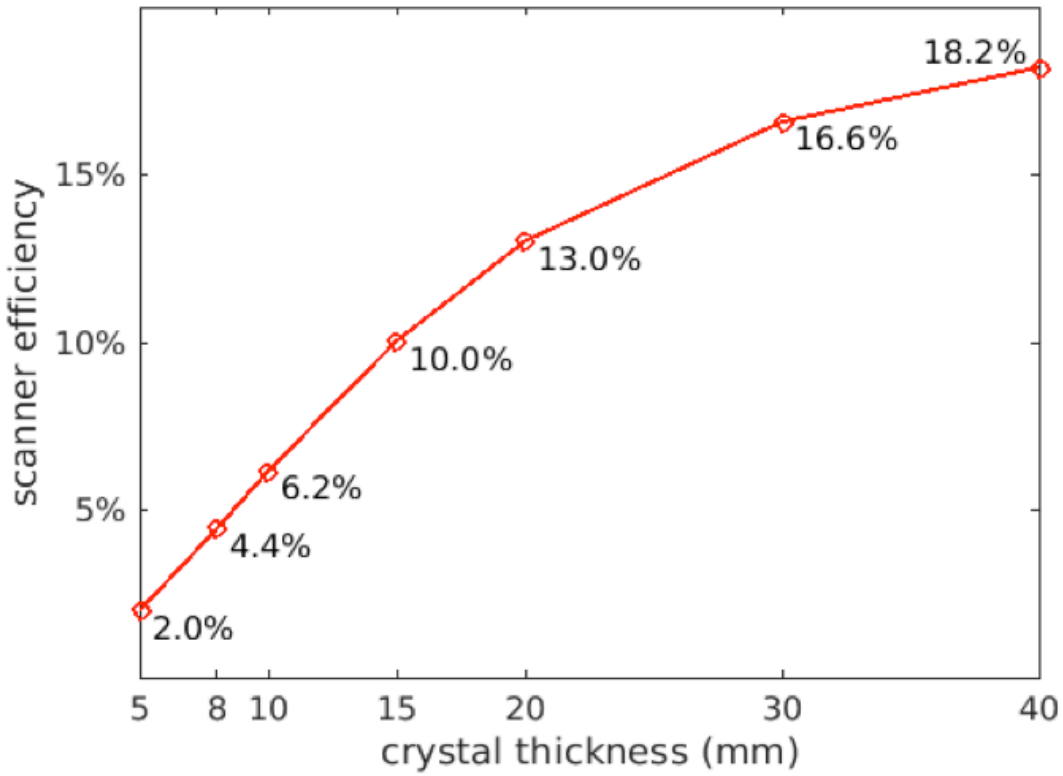

Figure 4.4. Scanner efficiency as a function of crystal thickness for the rectangular geometry.

LSO was used as the scintillator material. Events that were scattered in the object and events that were scattered in the crystals and eventually escaped were both rejected by an energy threshold of 510 keV.

4.5.3 *Sample reconstructed images*

Figure 4.5 shows three sample images of the 5 mm-diameter spheres using 1st-vertex, 3D-COM and 2D-COM LOR estimations (left to right). All three images were adjusted to the same gray scale. It was visually clear that the recovery coefficient was the best with 1st-vertex and worst with 2D-COM. Minor artifact could be observed in the near-chestwall region in the 2D-COM images, possibly due to the lack of depth-of-interaction and unoptimized normalization. In the

analyses that follow, RC values were averaged across the six interior spheres, away from the chest wall.

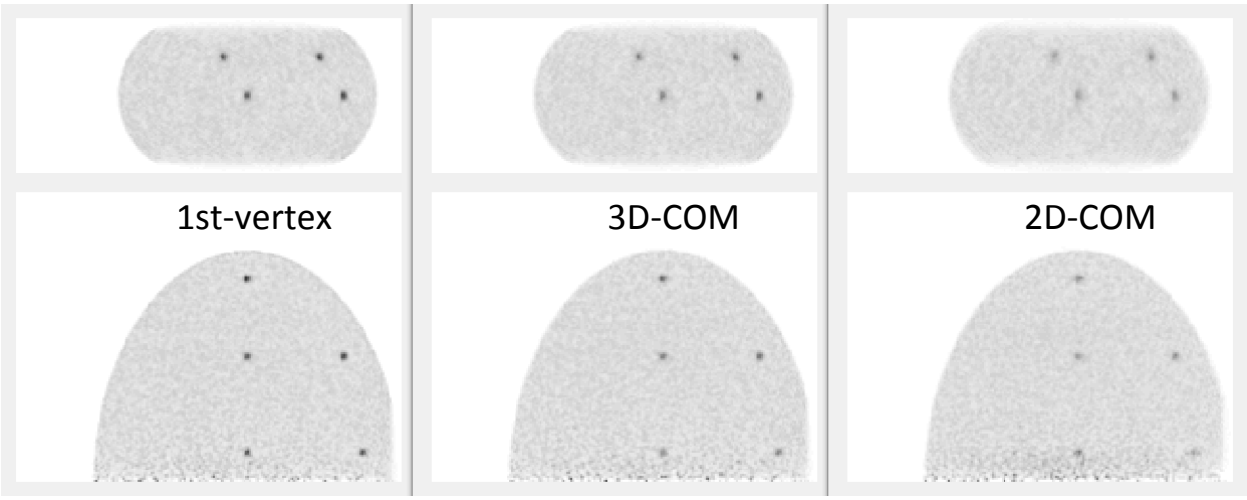

Figure 4.5. Orthogonal views of sample reconstructed images using the iterative algorithm.

Top row: PET/X axial cross-section at the anterior-posterior center, cf. Figure 4.2. From left to right, the LOR estimation methods were 1st-vertex, 3D-COM and 2D-COM. All images shared the same gray scale. Sphere diameter was 5 mm and crystal thickness was 10 mm. Image voxel size was 1mm. Iteration number was 15. No Gaussian smoothing was applied in this image.

4.5.4 *Post-reconstruction smoothing*

Post-reconstruction processing and image regularization have yet to be optimized for this system. We applied varying degrees of 3D-Gaussian smoothing to the image containing the 40 mm diameter hot sphere. The smoothing curbed the divergence of VOI_{max} as a function of iteration number, and had little effect on VOI_{mean}. (Figure 4.6) Note that 5 dashed lines of VOI_{mean} overlap with each other; similarly for VOI_{bkgd}. Based on this exploration, we applied smoothing with sigma = 0.8 mm for subsequent analyses of RC.

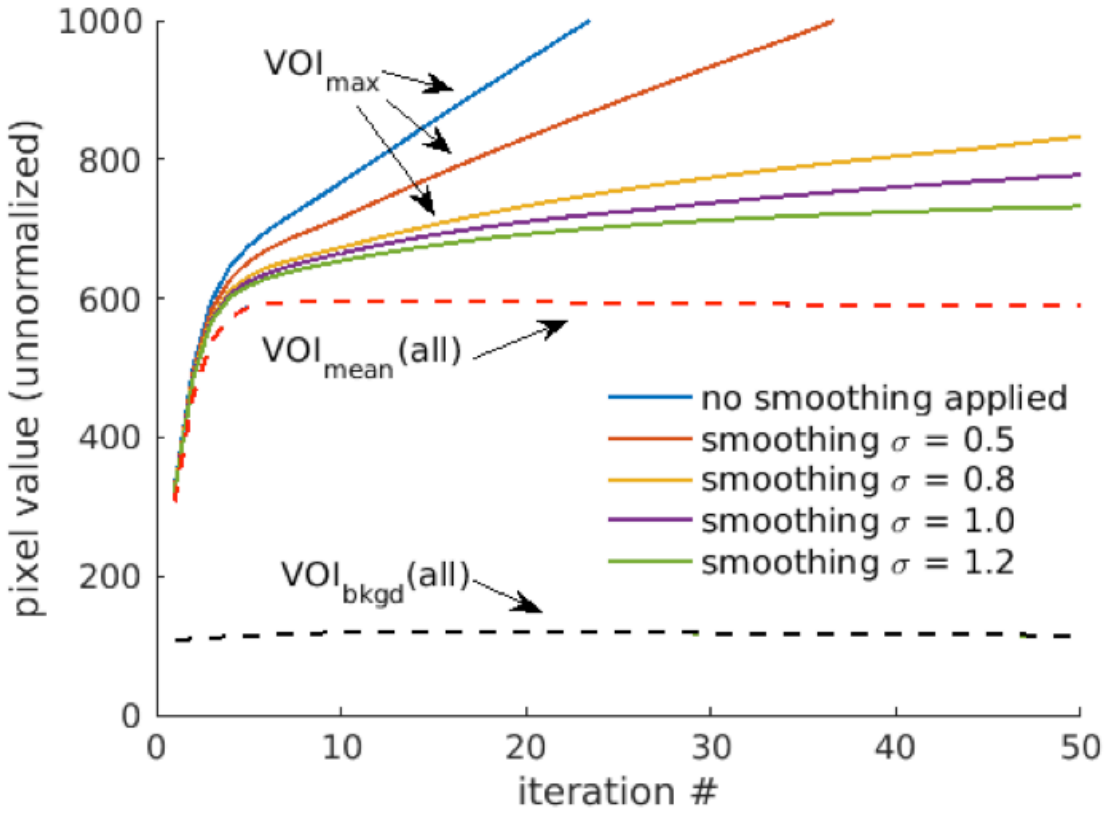

Figure 4.6. VOI_{mean}, VOI_{max} and VOI_{bkgd} as a function of iteration when various levels of post-reconstruction smoothing were applied, along with the original unsmoothed data, of the 40 mm-sphere phantom.

3D Gaussian filters with sigma = 0.5, 0.8, 1.0 and 1.2 mm were applied. Note that for both VOI_{mean} and VOI_{bkgd}, smoothing had little effect, resulting in the overlapping of 5 smoothing levels. The RC_{mean} in this case ranges from 0.99 to 1.05 for iterations > 10.

4.5.5 *Post-reconstruction smoothing (update)*

Post-reconstruction smoothing was also done on a separate set of simulation data that matched to the physical scanner prototype we have built. Its FOV was 240 mm × 100 mm × 160 mm. It used a uniform breast phantom with a similar number of decays as before. No attenuation was simulated and hence no attenuation correct was needed during reconstruction. The iteration

number was set to 100. The scanner FOV was segmented into 2 mutually excluded regions: breast and background (Figure 4.7). (Note the background here indicated the region in the phantom that had no activity) Four metrics were computed: mean values of breast and background, and standard deviations of those 2 regions. Similarly, the mean values were not affected every much by smoothing, while the standard deviation of the activity region varies quite visibly.

Based on Figure 4.9 (mostly on the standard deviation within the breast), sigma = 0.75 appeared to be a compromising balance between curbing numeric divergence and preserving image texture. It is consistent with the earlier conclusion of sigma = 0.8 in 4.5.4.

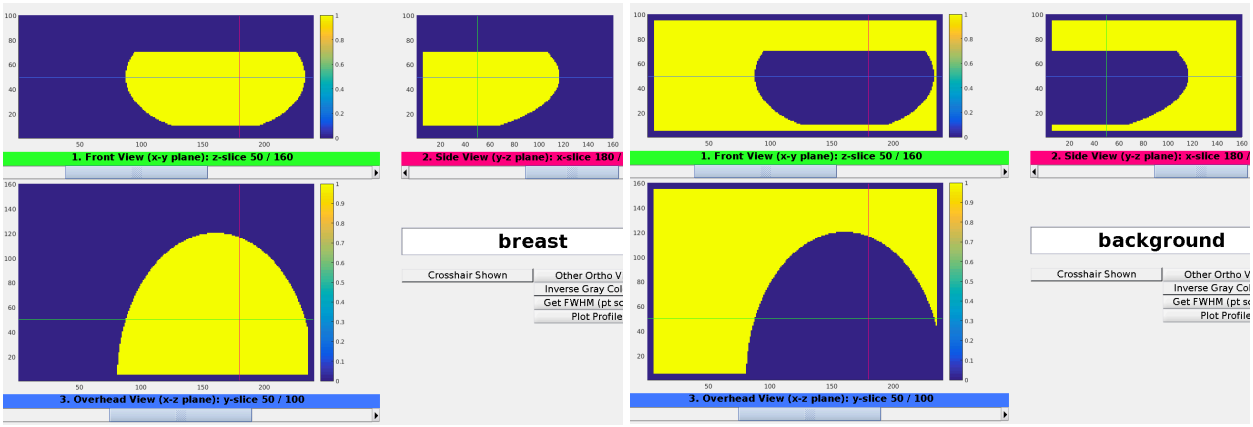

Figure 4.7. Two regions of interest: breast and background.

A 5 mm space from the FOV off the detector surface was excluded from the breast and background region. The breast and background regions did not share any overlaps.

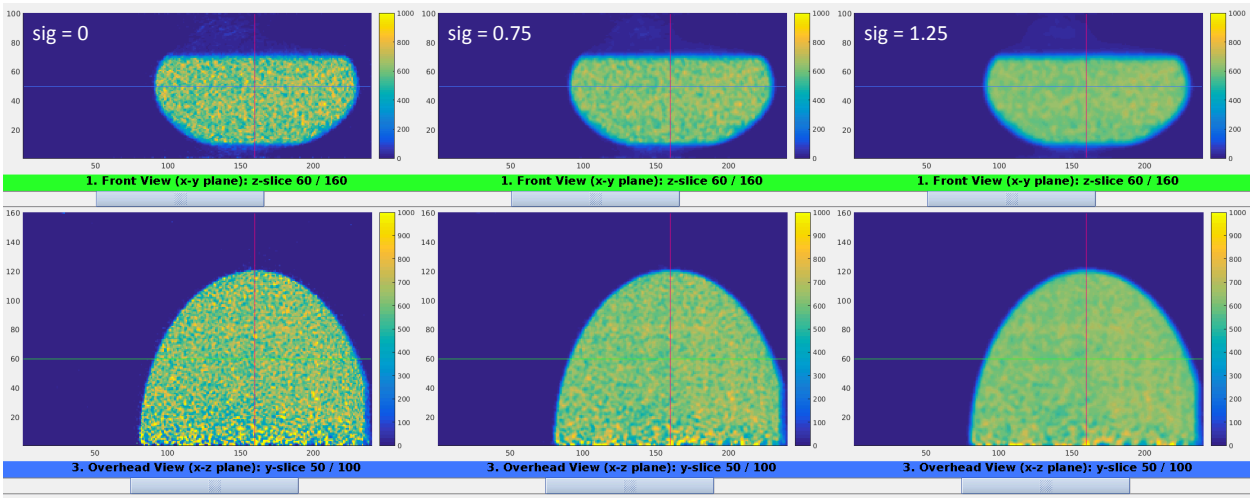

Figure 4.8. Sample reconstructed images using various filter sizes.

From left to right: post-reconstruction smoothing using Gaussian filters of sigma = 0, 0.75 and 1.25.

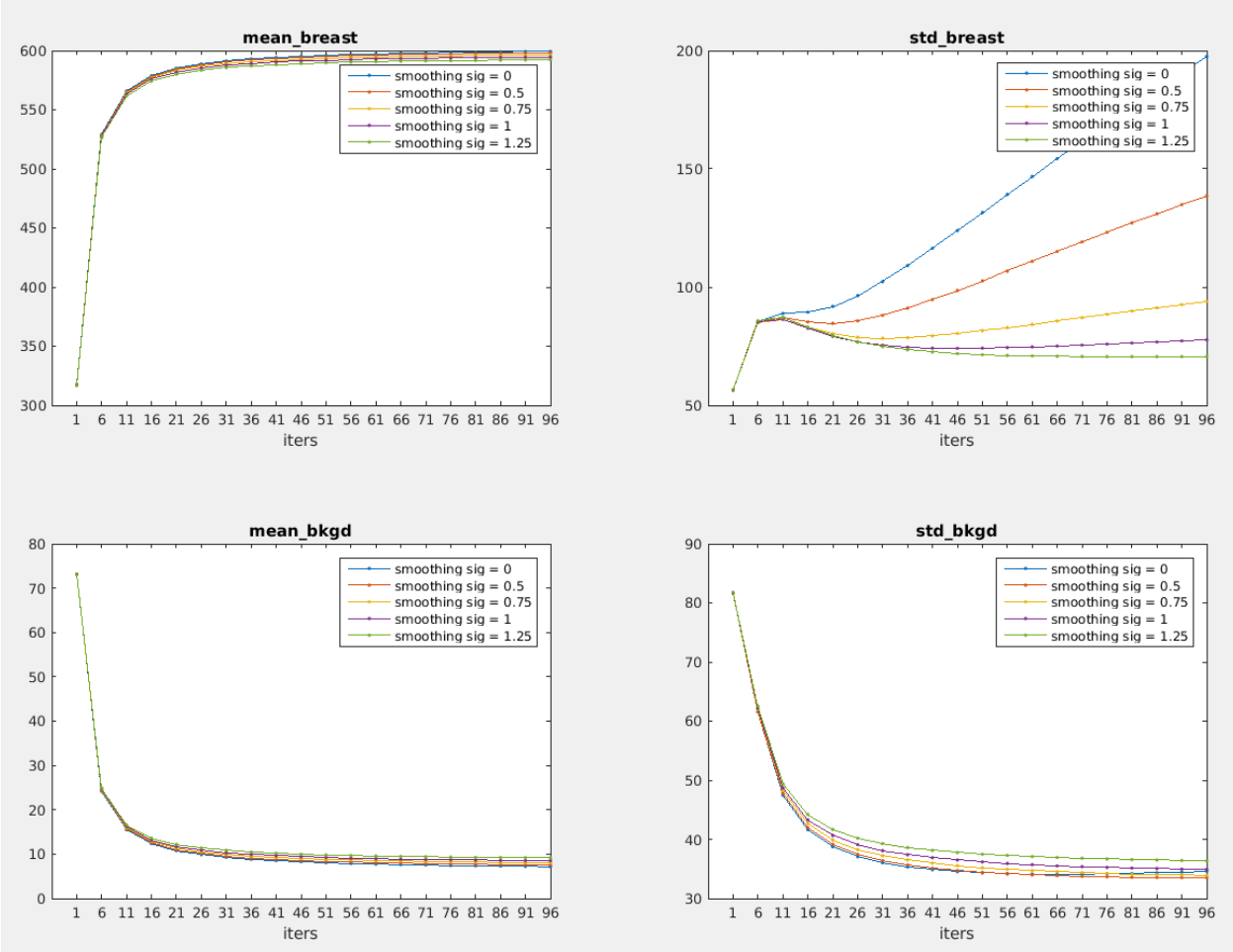

Figure 4.9. Mean and standard deviation as a function of iteration for various smoothing levels.

All metrics were calculated based on the raw voxel values and were not normalized. All four graphs shared the same arbitrary unit. Four different sigma's were used for the Gaussian smoothing and *sig = 0* corresponds to the original unsmoothed image. Except for standard deviation of breast, all 3 metrics were close to asymptotic values by iteration 30.

4.5.6 *Contrast recovery coefficient (RC)*

Figure 4.10 plots *RC* as a function of sphere size (A) or detector crystal thickness (B), with the error bars representing the ERMSE eq.(4.5).

In (A), the *RC* difference between 3D-COM and 2D-COM (DOI versus no DOI) was more significant with smaller spheres. Also note that the error bars were smaller for larger spheres for all three LOR estimation methods.

In (B), with 1st-vertex LORs, *RC* was essentially independent of detector thickness as expected. However, with 3D- and 2D-COM, thicker detectors led to lower *RCs*. In particular, the *RC* difference between 3D-COM and 2D-COM was larger for thicker crystals. It was also important to point out that the error bars were smaller with thicker crystals, albeit with lower *RC* values.

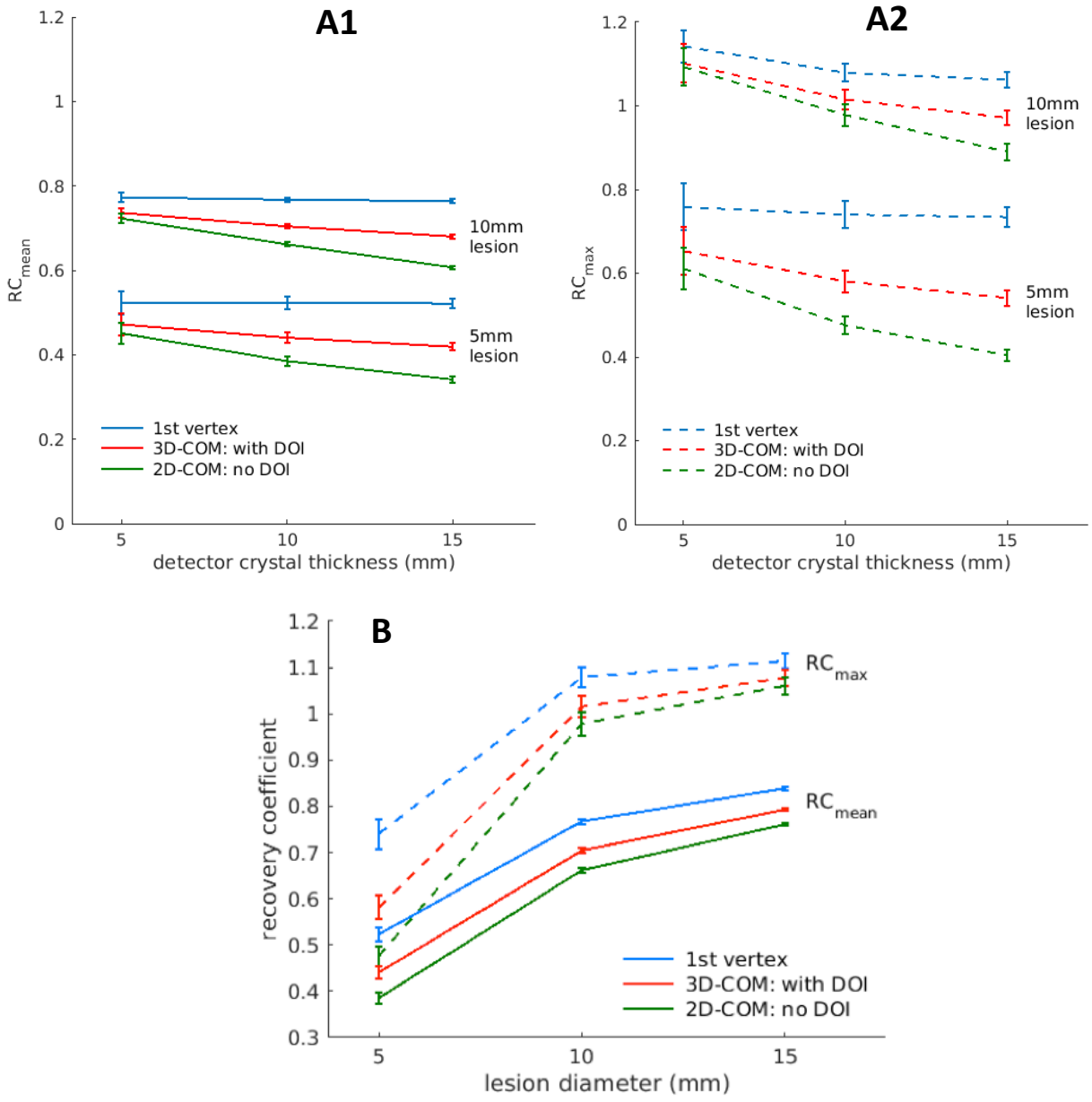

Figure 4.10. Recovery coefficient as a function of lesion size and crystal thickness. (A1): Recovery coefficients with various crystal thicknesses for both lesion sizes of 10 mm and 5 mm. RC_{mean} values were shown. (A2): Same as (A1), but using RC_{max} values. (B): Recovery coefficients for various sphere sizes with crystal thickness of 10 mm. Both RC_{max} and RC_{mean} were plotted. In all three subfigures, all three LOR estimate methods were included. The error bars represented ERMSE. Each image was treated with a post-reconstruction Gaussian smoothing with sigma = 0.8 mm as mentioned previously.

4.5.7 *RC variance*

Table 4.9 shows the ratio of ERMSE to mean of the *RCs* for cases of 5/10 mm crystals and 5/10 mm spheres. The values outside parenthesis were calculated using RC_{mean} and inside using RC_{max}. In each configuration, we simulated both TBRs (5:1 and 4:1) independently. The ratio ranged from sub-1% to 6% depending on the configuration of crystal thickness and sphere size. In all configurations, the results were similar between 2D-COM and 3D-COM.

Table 4.9. Ratio of ERMSE/global mean of the recovery coefficients.

all units are %*				
TBR = 5	5 mm sphere		10 mm sphere	
Crystal thickness	2D-COM	3D-COM	2D-COM	3D-COM
5 mm	5.33 (8.03)	5.49 (8.72)	1.55 (4.10)	1.51 (4.18)
10 mm	2.85 (4.57)	2.81 (4.41)	0.74 (2.68)	0.72 (2.29)
TBR = 4	5 mm sphere		10 mm sphere	
Crystal thickness	2D-COM	3D-COM	2D-COM	3D-COM
5 mm	5.42 (8.18)	5.90 (9.03)	1.72 (4.64)	1.66 (4.60)
10 mm	2.98 (4.58)	3.03 (4.68)	0.92 (3.12)	0.88 (2.35)

* the percentages outside of the parentheses were calculated using RC_{mean}, and those inside were using RC_{max}

4.5.8 *Sensitivity and specificity of detecting changes*

Results from the ROC analysis are shown in Figure 4.11. We found essentially equivalent results when using either *RC* (eq.(4.7)) or just the sphere VOI data ($VOI_{mean/max}$) as the radiotracer uptake metric. The radiotracer uptake metric used clinically, SUV, is based on data from an image region of interest without regard to the local background or true contrast. Our results were similar for sphere VOI and *RC* because in our case the background VOI data were very stable (i.e., low, consistent variance in all cases).

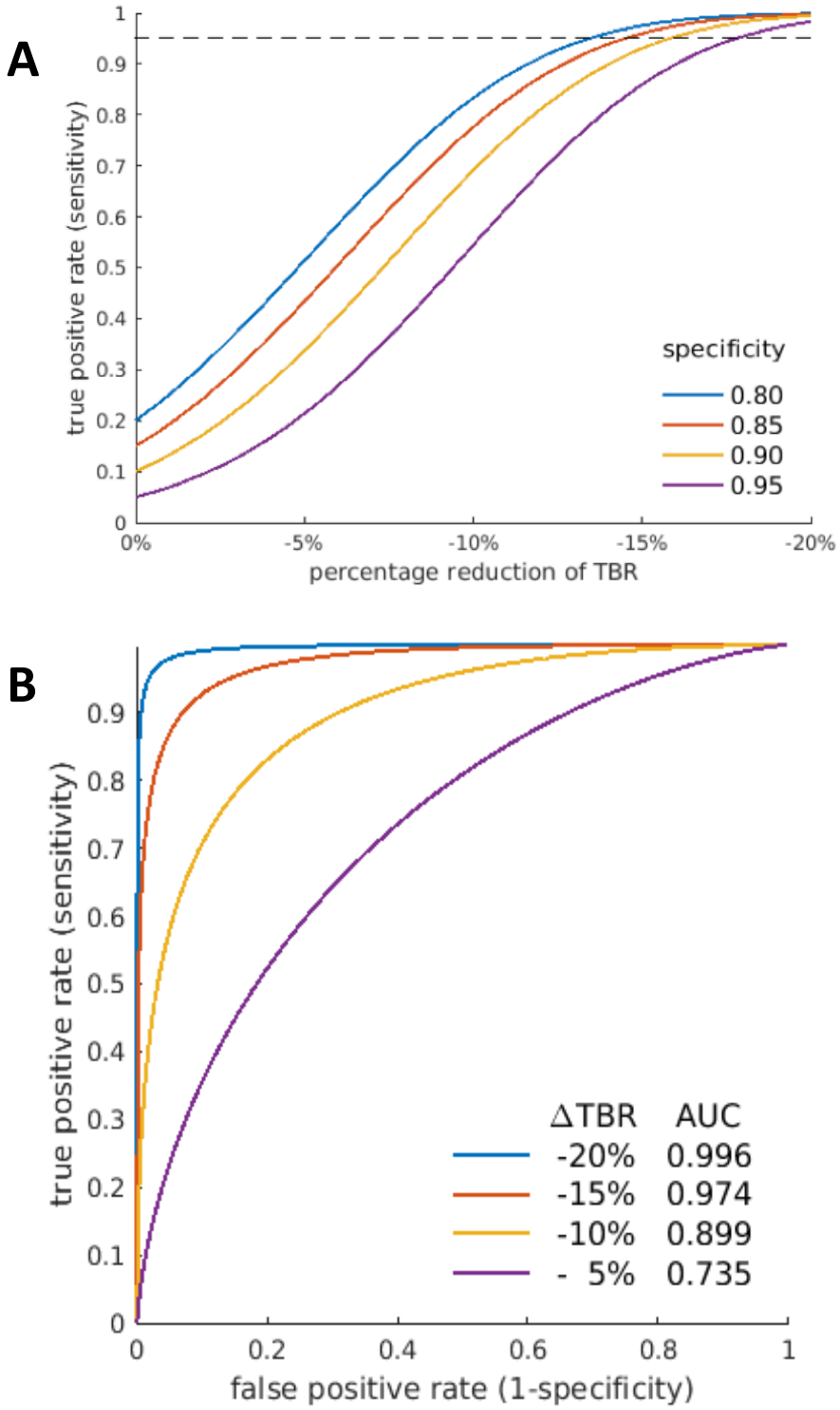

Figure 4.11. Sensitivity and AUC-ROC for different reductions of TBR.

(A): Sensitivity as a function of reduction in TBR from a pre-therapy value of 5:1. Each curve corresponds to one of four specificity values. (B): ROC curve for four TBR

reductions: -20%, -15%, -10% and -5%. Both plots were computed with the data set of sphere diameter of 5 mm and crystal thickness of 10 mm. The LOR estimation method was 2D-COM (without DOI).

Plot (A) in Figure 4.11 shows the sensitivity for detecting a change in TBR as a function of the reduction in true TBR. The results show that 95% sensitivity (horizontal dashed line) can be achieved for a true TBR reduction of approximately 13% to 18%, with a corresponding specificity of 80% to 95%, respectively. Plot (B) shows the calculated ROC curves. The AUC of a TBR change of -20% was over 99%. For the other scanner designs and sphere sizes in this study, the AUC's of a -10% TBR change are given in Table 4.10 and those of -20% TBR change in Table 4.11. Again, the values outside parenthesis were calculated with RC_{mean} and inside were with RC_{max}.

Table 4.10. AUC's of various configurations of crystal thickness, sphere size and LOR estimate method. (ΔTBR = -10%)

In each AUC analysis, ΔTBR=-10%

Crystal thickness	5 mm sphere		10 mm sphere	
	2D-COM	3D-COM	2D-COM	3D-COM
5 mm	0.7927 (0.7473)	0.7953 (0.7404)	0.9995 (0.9049)	0.9997 (0.8988)
10 mm	0.8987 (0.8364)	0.9342 (0.8847)	1.0000 (0.9772)	1.0000 (0.9913)

* the AUC's outside of the parentheses were calculated using RC_{mean}, and those inside were using RC_{max}

Table 4.11. AUC's of various configurations of crystal thickness, sphere size and LOR estimate method. (ΔTBR = -20%)

In each AUC analysis, ΔTBR=-20%

Crystal thickness	5 mm sphere		10 mm sphere	
	2D-COM	3D-COM	2D-COM	3D-COM
5 mm	0.9552 (0.9190)	0.9563 (0.9122)	1.0000 (0.9967)	1.0000 (0.9960)
10 mm	0.9957 (0.9795)	0.9991 (0.9939)	1.0000 (1.0000)	1.0000 (1.0000)

* the AUC's outside of the parentheses were calculated using RC_{mean}, and those inside were using RC_{max}

4.6 DISCUSSION

In this paper we present a preliminary analysis of how scanner crystal thickness and DOI information affects the ability of the proposed rectangular PET/X to accurately measure changes in radiotracer uptake. We used image reconstruction algorithms recently customized to the rectangular scanner geometry and multiple independent statistical realizations to investigate metrics aimed at characterizing the ability to reliably measure changes in tracer uptake in target lesions. The results indicated that, for fixed scan time, thicker crystals were beneficial to the system's ability to detect changes in lesion uptake (Table 4.10), despite the associated loss of spatial resolution and contrast recovery due to the thicker crystals (Figure 4.3 and Figure 4.10 top). The benefits stem from reduced image noise (lower variances, Table 4.9) achieved through the greater detector efficiency of thicker crystals. Improvements to spatial resolution via the use

of DOI information did not have a substantial impact on the ability to detect changes in radiotracer uptake.

Spatial resolution followed the expected trend of increasing (i.e., worsening) for thicker crystals and improving with the use of DOI information. Notably, thicker crystals also led to more spatial resolution variation throughout the scanner FOV.

It is important to note the idealized conditions of the simulations when assessing these results. Our goal was to establish the feasibility of quantitative precision for the rectangular scanner and customized image reconstruction algorithms. This paper represents a further, albeit still intermediate, assessment of these reconstruction approaches. We also examined fundamental improvements provided by near-ideal DOI information. The unconventional scanner geometry contributed to our motivation to study performance at a basic level.

Following our earlier work [59], we studied a potential spatial resolution surrogate (d_{FWHM}, eq.(4.1)) that is calculated from list-mode (or sinogram) data, independent of image reconstruction method. Such a metric would have utility in scanner design optimization by allowing assessment of intrinsic spatial resolution trends without the need for image reconstruction, whose properties may influence the resolution taken from images. We found a strong correlation between d_{FWHM} and 2D-COM (no DOI) image FWHM (Figure 4.3). However, while the d_{FWHM} metric using 3D-COM data (with DOI) was also sensitive to changes in crystal thickness, spatial resolution from images reconstructed using 3D-COM LOR estimates was not (Figure 4.3). Thicker crystals allow a wider distribution of event interaction positions, which will affect d_{FWHM} in the manner observed. The DOI information used for this study was idealized in that we did not model finite DOI resolution. As such, the DOI estimates in 3D-COM data could

act as ideal DOI data from which one would not expect to see variations in image FWHM as a function of crystal thickness.

Testing the attenuation correction (AC) process was part of this initial test of the new image reconstruction algorithm for the PET/X geometry. We used the known, true AC maps with a goal of validating the AC process. (With the test phantom of a 40 mm sphere, full contrast recovery of $RC = 1$ was obtained, indicating effective AC.) The ultimate goal is to couple PET/X to an x-ray mammography/tomosynthesis system, which will provide data from which a spatially variant attenuation correction map could be estimated. At this stage we are not in a position to speculate on the quality of measured AC data, and further details of AC approaches are beyond the scope of what was studied here.

Sphere size has an apparent influence on the RC value. For smaller spheres, *RC* values among the three LOR estimation methods were ordered as expected: 1st-vertex was the highest, followed by 3D-COM, and lastly 2D-COM. The impact of the partial volume effect is seen in Figure 4.10.

Crystal thickness was one of the design questions we investigated in this simulation study. Thicker crystals yielded lower mean activity recovery coefficient (Figure 4.10 top). The degradation was greater when no DOI information was available (2D-COM versus 3D-COM), likely due to a relatively high percentage of oblique LORs in the rectangular FOV geometry. It should be pointed out that, in evaluating the scanner's ability to detect change between two scans, both the mean and variance of *RC* matter. As shown in Figure 4.10 (top), thicker crystals led to a lower *RC*, but also lower variance, presenting a potential tradeoff between accuracy and precision. We suspected that the lower variance from thicker crystals was due to higher scanner

efficiency (Figure 4.4), which resulted in higher counts per scan for the fixed scan time that we simulated.

This analysis omitted several important physical phenomena (scattered photons, positron range, detector point-spread-function). Detailed effects of optical photon transport were not included in the event positioning modeling. Our lab has investigated spatial response functions for monolithic crystals [62; 63], which can have advantages over pixelated crystal detectors. Modeling the performance of monolithic crystal detectors requires more consideration of optical photon transport than does modeling pixelated detector response. The first prototype PET/X scanner has been constructed using pixelated scintillator detector blocks, with a 20×20 matrix of 2mm crystals resolved by a 12×12 array of 3 mm SiPM's. Although idealized in several ways, the event-positioning model used here should be a good first-order model of the positioning in these first prototype PET/X blocks.

Detector energy resolution was not modeled so that we could study scatter-free coincidence events by setting the energy cutoff at 510 keV. From parallel work on detector hardware development, however, we estimate that the energy resolution will be approximately 18% at 511 keV. If this is the case, then using a lower energy threshold (LLD) around 400 keV would result in the detection of the great majority of true coincidences for which both annihilation photons deposit 511 keV in the detectors, as well as many where one or both photons escape after scattering one or more times, as shown by Lewellen et al. [64]. This LLD would also result in the detection of undesirable scattered coincidences, thus reducing the noise-equivalent count (NEC). Thus the overall impact on the reducing the noise-equivalent count is not clear, and there is very little published literature on this specific question. Levin et al [65] showed that for energy resolutions of 3% for CZT and 12% for LSO, the peak reducing the

noise-equivalent count did not change appreciably when the LLD was optimized for each material. We note that there were multiple changes for the very different detector systems, such as photo-fraction and timing resolution etc., so the results of Levin et al. and Lewellen et al. may not apply in our situation. Nonetheless we believe that while there may be some loss in effective sensitivity with a typical energy resolution, it will be a small enough decrease to not impact our conclusions. We anticipate acquiring measured data to study this effect empirically.

In this study we did not perform a systematic evaluation of how performance metrics (spatial resolution, *RC*) varied within the PET/X rectangular FOV. We note however that some variation was observed at the FOV axial edge (e.g., image slices parallel to and near to the patient chest-wall) where coincidence event sampling is reduced and reconstruction normalization has yet to be optimized. Variations within the interior FOV were encompassed by the calculation of ERMSE.

Under the idealized conditions mentioned above, the PET/X system easily met our initial target performance of <5% type-1 error when measuring 20% TBR changes in 5 mm spheres. This is a promising indication that the PET/X scanner has the potential for measuring TBR changes that may prove clinically useful, even after including the omitted physical effects that will likely degrade the results found here.

As a starting point, this analysis used idealized data to demonstrate the feasibility of reaching the goals for the PET/X scanner. It also established a viable framework to quantitatively evaluate the scanner performance for phantom scans. The analyses will be carried forward in the future by introducing more accurate data modeling and ultimately using measured PET/X scanner data. Based on these results we expect the PET/X scanner to meet clinical requirements even when more realistic features are incorporated. Sensitivity and specificity data (Figure 4.11)

measured on the scanner from phantom imaging will be useful for designing clinical trials that use PET to monitor therapy response.

4.7 CONCLUSION

For the PET/X design parameters and clinical goals studied here, thicker crystals (≥ 10mm) provided an advantage in image noise that outweighed associated disadvantages in spatial resolution and recovery coefficients. This advantage assumed a fixed scan duration for which thicker crystals provided higher image data counts via the higher efficiency for annihilation photon absorption relative to the thinner comparators. Including idealized DOI information did not substantially improve AUC in the ROC analysis.

The results of this work represent best-case scenarios for identifying changes in radiotracer uptake using the proposed rectangular PET/X scanner and the current version of image reconstruction algorithm; perfect correction for attenuation, scatter, and normalizations are assumed, and positron range was not included. It is encouraging that the sensitivity was > 95% (for 95% specificity) and AUC was over 0.995 for the task of measuring a 20% change in tracer uptake in a 5 mm lesion, which was the initial, prospective goal of the PET/X scanner. While image quality degradations due to the neglected physical effects will reduce the statistical power, this work establishes a performance bound on which to base future studies that introduce additional physical effects.

Chapter 5. XAC (X-RAY BASED ATTENUATION CORRECTION)

5.1 OVERVIEW

Attenuation correction is arguably the most important correction in PET reconstruction. As illustrated in Figure 1.5, omitting this correction will lead to severe artifacts. In practice, the attenuation map is acquired by a low dose CT scan using the clinical PET/CT scanner. The CT image is then segmented by tissue type, converted to attenuation map at 511 keV, down-sampled to match the PET image size and resolution, and eventually used for PET attenuation correction. Since the CT image is not used for diagnostic purpose, it can be acquired with a lower dose than a diagnostic CT.

In principle, attenuation correction would be simpler for breast PET than for whole-body PET. Without presence of bones and lungs, breast tissue (composed of mainly adipose and glandular tissues) tends to have similar attenuation coefficients at 511 keV. On the other hand new challenges are posed for dedicated breast PET scanners, since they are expected to have a more compact design and a cheaper operating cost.

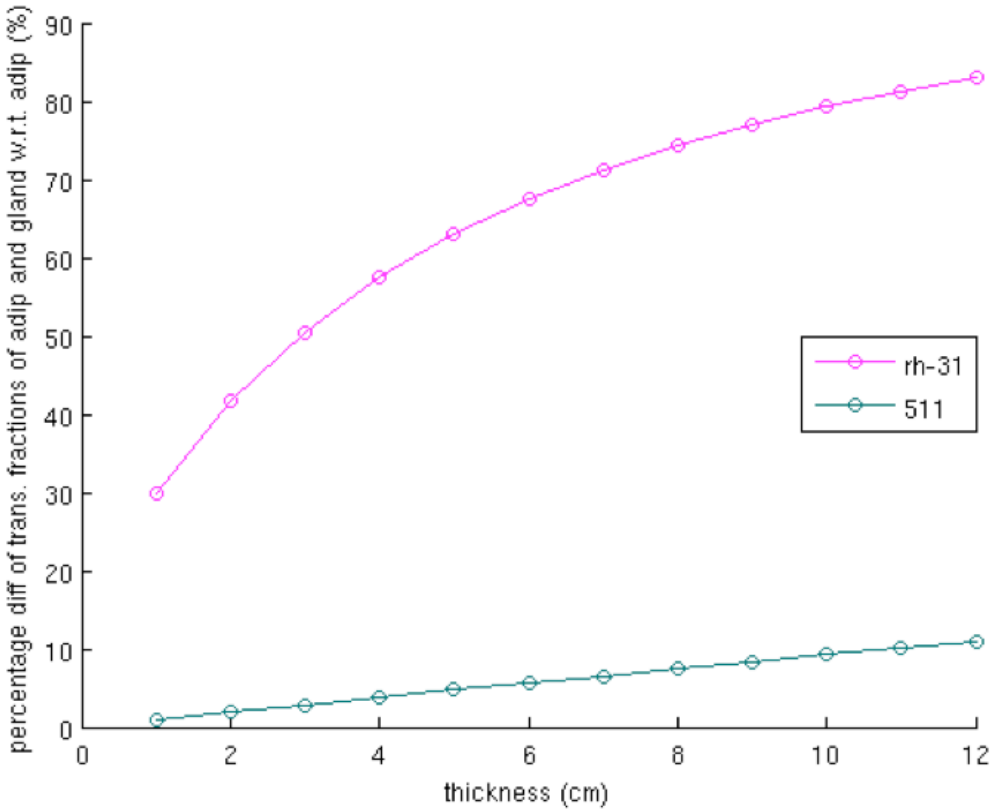

Figure 5.1. Difference of transmission properties of adipose and glandular. The percentage difference in the y axis is calculated as 1 - TF_glandular / TF_adipose, where TF stands for transmitted fraction of photons after going through a slab of said material. The pink curve corresponds to the mammographic spectrum (rhodium 30 keV) and the green curve is monochromatic X-ray (511 keV). One can see adipose and glandular materials behave quite distinctively in mammography but similarly for PET.

Very few dedicated studies were done to investigate the effect of attenuation correction for breast PET [66]. Some dedicated breast PET scanners, such as the commercial product from Naviscan, do not use any attenuation correction [67]. Other scanners that do deploy attenuation correction implementations fall in more or less two camps. The first one is to pair the PET detectors with a mini CT scanner [29]. It mimics the concept of a clinical whole-body PET/CT

scanner and computes the PET attenuation map based on the CT scan. The other class infers the breast boundary information from the PET emission data alone [68] [28].

PET/X is the first (and the only as we know now) prototype of combining PET and mammography. So it's natural to explore the possibility of inferring attenuation map from the mammogram. Admittedly it is obvious that the problem does not possess a mathematically closed, nor unique, solution, as we are inferring the 3D volume from a 2D projection image. However, for all intents and purposes, it's possible that an approximated volume will suffice for attenuation correction purpose in breast PET reconstruction.

It's worth mentioning that breast volume/contour estimation is also a point of interest in a few other research areas such as tomosynthesis and breast density estimation, in additional to breast PET reconstruction. For example, a recent study explored using structured light (SL) technology that involves 2 pairs of projectors and digital cameras [69]. Tomosynthesis itself can also produce a 3D volume estimation of breasts. We keep an eye on those innovative approaches for potential applications for PET/X attenuation correction.

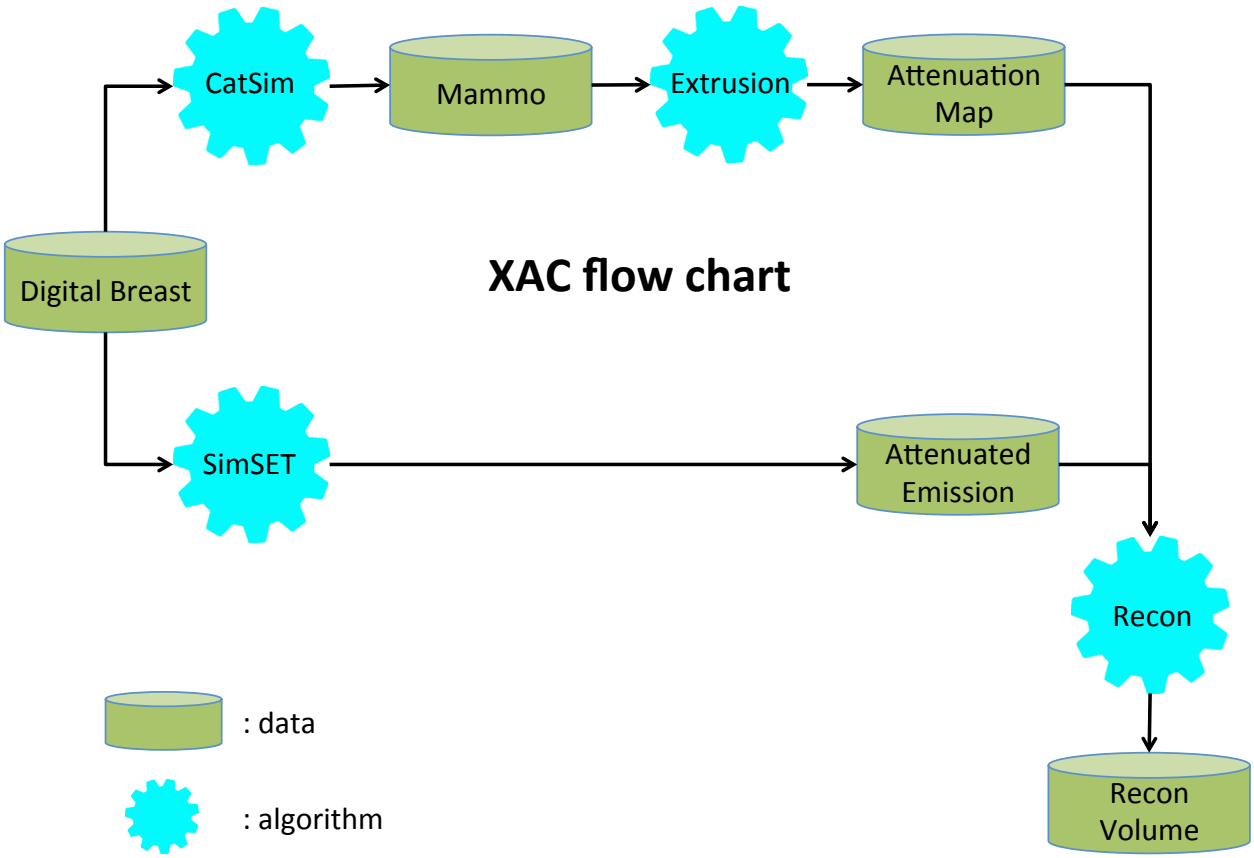

Figure 5.2. Flow chart of XAC for PET/X.

This flow chart shows the basic components of the X-ray-based attenuation correction (XAC) for PET/X in a simulation study. The top route is equivalent to the CT branch in the clinical PET/CT scanner, and outputs an estimated attenuation map. The bottom route is the PET branch and produces attenuated emission data. Both outputs are then combined and fed into the reconstruction package to produce the attenuation-corrected PET reconstruction image.

5.2 MAMMOGRAPHY SIMULATION

As detailed in 3.2, CatSim is modified to simulate mammograms. Along with the simulated mammogram, a corresponding air scan is also simulated. The latter is then used as a multiplicative correction to the former to remove the unevenness in the background (Figure 5.3). Though this correction may seem trivial and arguably redundant in simulation (since the uneven

background had to be simulated in the first place and then be undone via correction), it holds an indispensible role in practice. In a real scan, this calibration is responsible for the overall normalization correction, including dead pixels and heel effect etc.

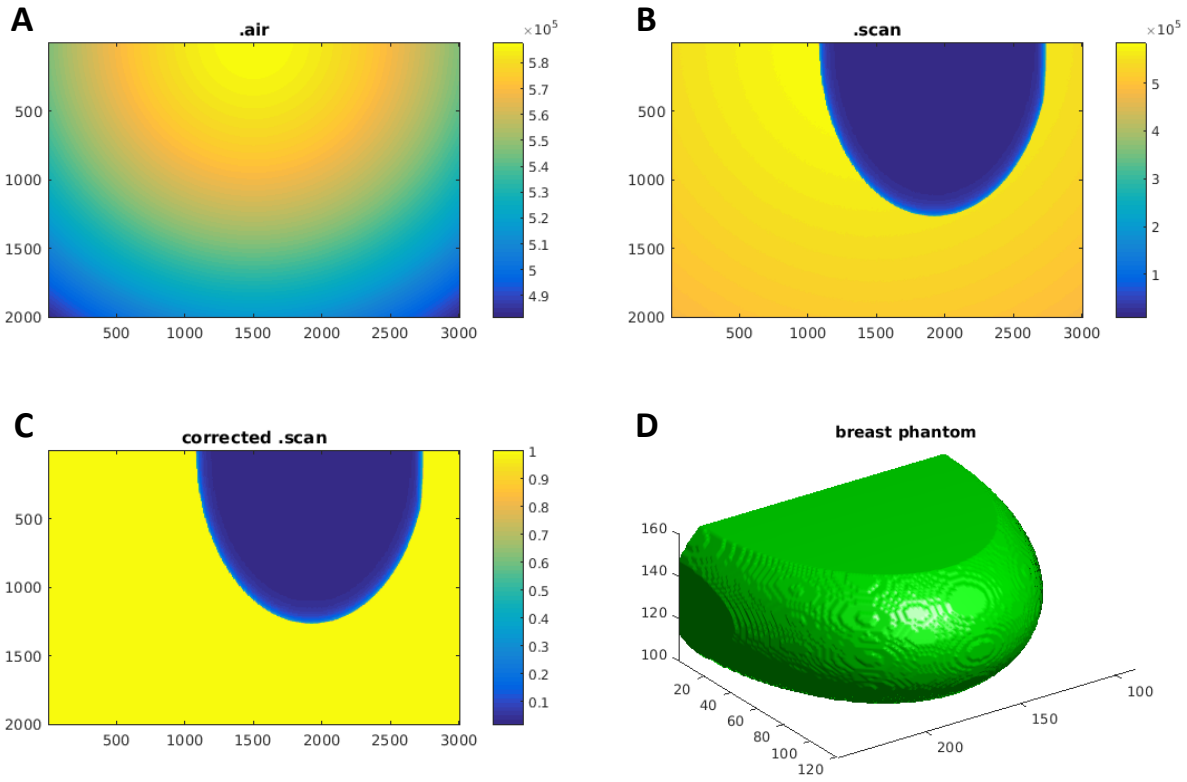

Figure 5.3. Simulated mammogram.

(A): Air scan from a mammography simulation. One can see the source is directly above the edge of FOV as expected (the brightest spot). (B): A simulated raw mammogram. (C): Corrected mammogram by dividing the raw mammogram by the air scan. One can see that the background uniformity is restored now. (D): 3D rendition of the digital breast phantom: a truncated ellipsoid with uniform adipose.

5.3 EXTRUSION

As a start, we take a simple approach to estimate the 3D breast volume extruded from the 2D mammogram. The algorithm first estimates the attenuation coefficient using the un-attenuated pixel values (of those outside the breast area) and the pixel values directly below the X-ray source. Assuming uniform attenuation coefficient within the breast, it then traverses through the entire FOV on mammogram to calculate the attenuation length from the source to each pixel. Those lengths of attenuation path are positioned back into the 3D volume with their middle points lying on the horizontal plane half way between the plane detector and compression paddle. Collectively the attenuation paths fill up the breast volume.

This algorithm requires a few pieces of prior knowledge, including SDD (X-ray source to detector distance), the compression height (compression paddle to detector distance) and mammogram pixel size. Since the mammogram pixel size is much smaller than the PET image voxel size, the extruded breast volume also needs to be down-sampled to match the PET FOV.

Even though this algorithm is relatively simple, for the given test digital breast phantom, it restores the breast volume relatively well, shown in Figure 5.4. The biggest discrepancy, as one can probably deduce, takes place toward the tip of the breast. Upon a voxel-to-voxel comparison, the extruded phantom differs from the original phantom by 49,686 voxels, a 6.26% difference from the 793,436 voxels in the original phantom. Surprisingly whether lesions of glandular tissue present in the phantom doesn't seem to affect the extrusion result much. The extrusion volumes from a uniform breast phantom with or without lesions differ by only 590 voxels, less than 1% of estimated volume.

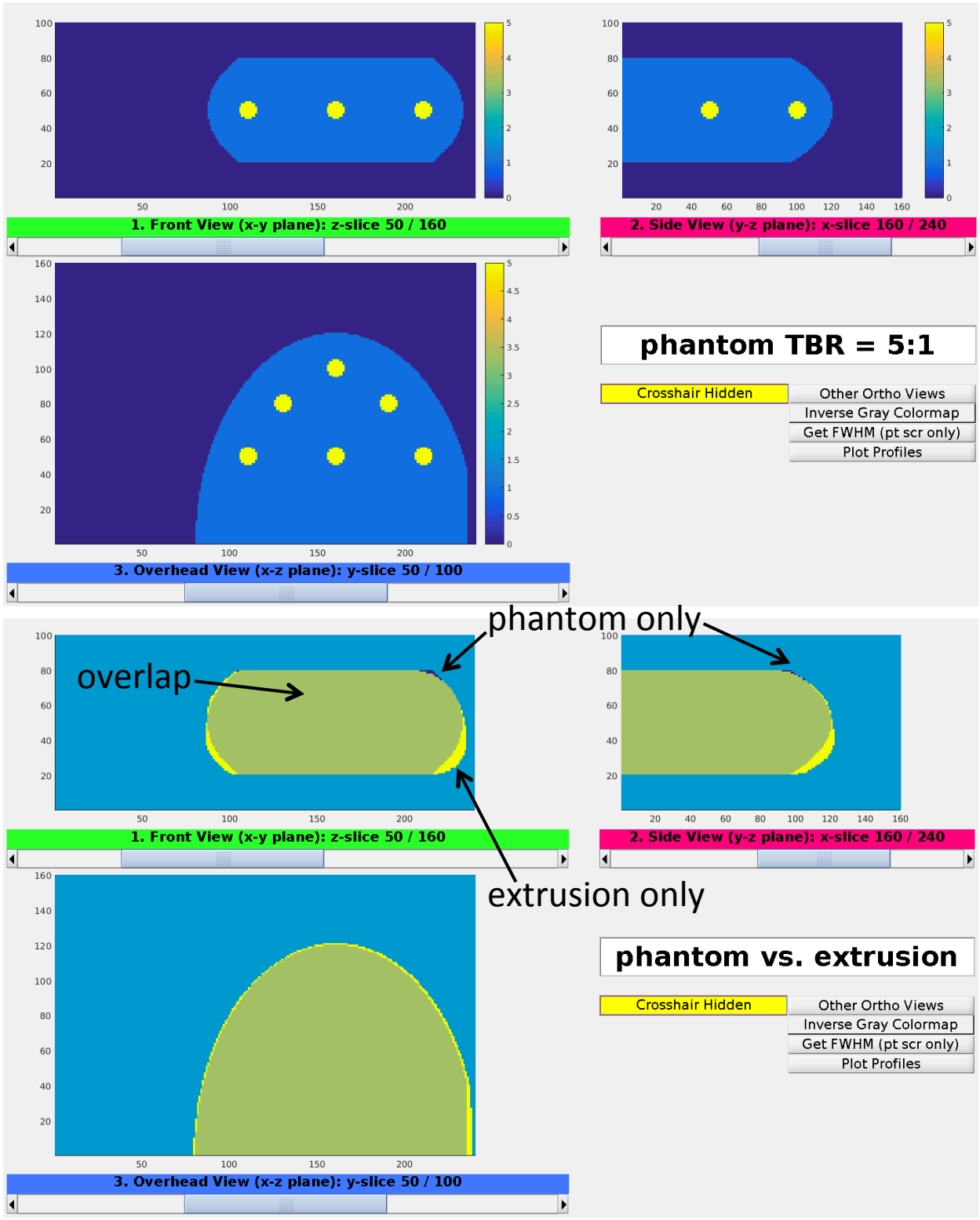

Figure 5.4. Original breast phantom compared to the extrusion volume. (Top): Original digital phantom for both PET and mammography simulation. The lesion-to-background activity ratio is 5:1 and the lesion/background materials are

glandular/adipose. (Bottom): The extruded breast volume from mammogram overlaid with the original phantom. One can see the majority of the two volumes overlap, differing mostly around the peripherals and the tip. The bright yellow voxels exist only in the extrusion, but not in the original phantom. Reversed for the dark blue voxels. The majority voxels (dirty green) indicate the overlap regions of the two volumes.

5.4 RECONSTRUCTION RESULTS

I reconstruct the PET images using 2 different attenuation maps and compare the results: one of ground truth attenuation map (trueAC) and the other of extruded breast volume based on the simulated mammogram (XAC). The original digital phantom contains 6 lesions of 10 mm diameter through out the breast volume. The difference of 2 reconstructed images (trueAC vs. XAC) is also shown to highlight the areas that are most affected by an imperfect attenuation map (Figure 5.5). As we can see, the 2 reconstructed images differ mostly around the peripherals and the tip of the breast, a pattern consistent with the difference of 2 attenuation maps (shown in the bottom image in Figure 5.4).

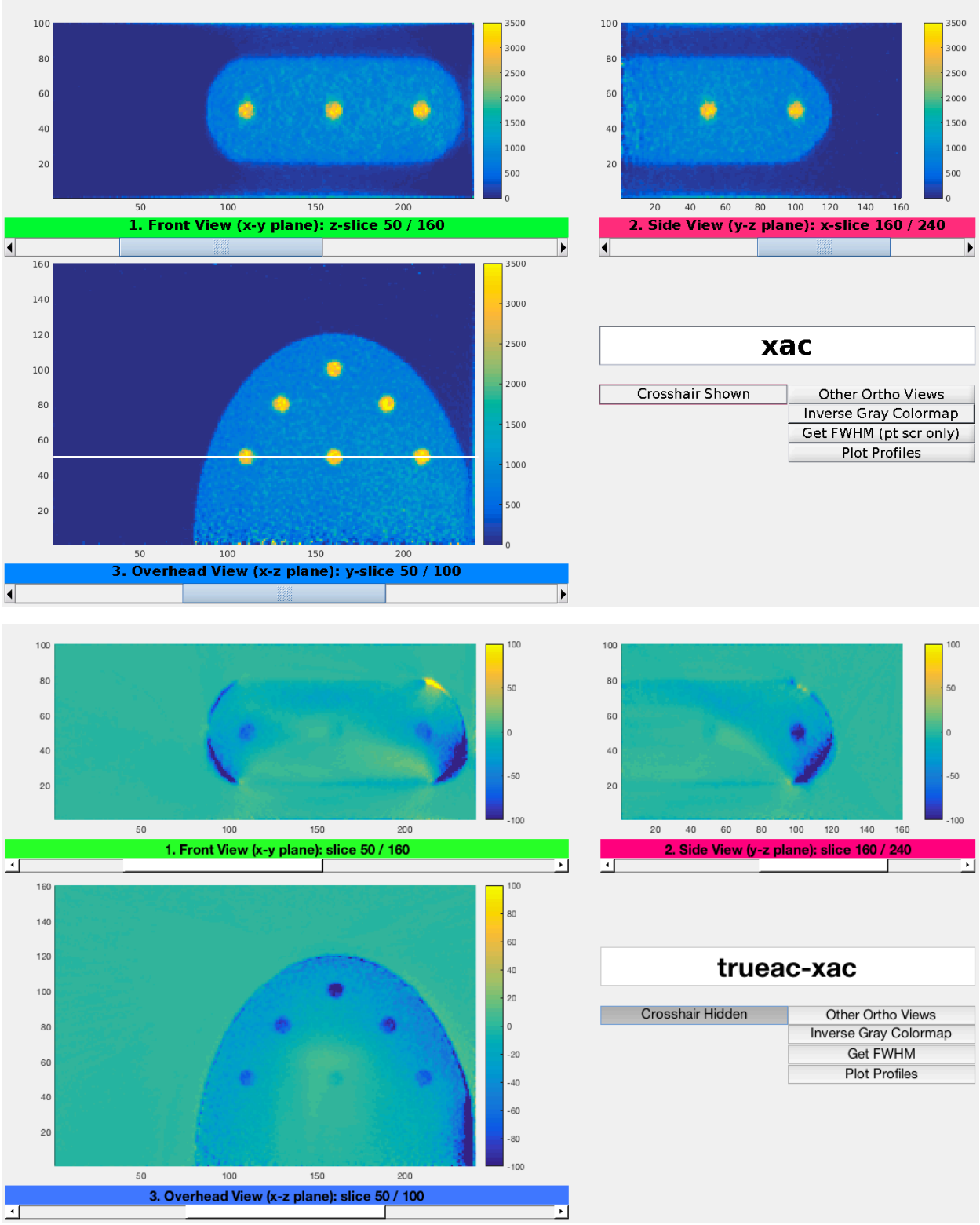

Figure 5.5. Reconstructed PET images using trueAC and XAC.

(Top): Reconstructed images using XAC. The profile through the white fine line will be plotted in a separate figure. (Bottom): Difference image obtained by subtracting XAC

image from trueAC image. As expected, the most variation occurs around the boundary of the breast, while the central lesion is mostly unaffected (barely visible).

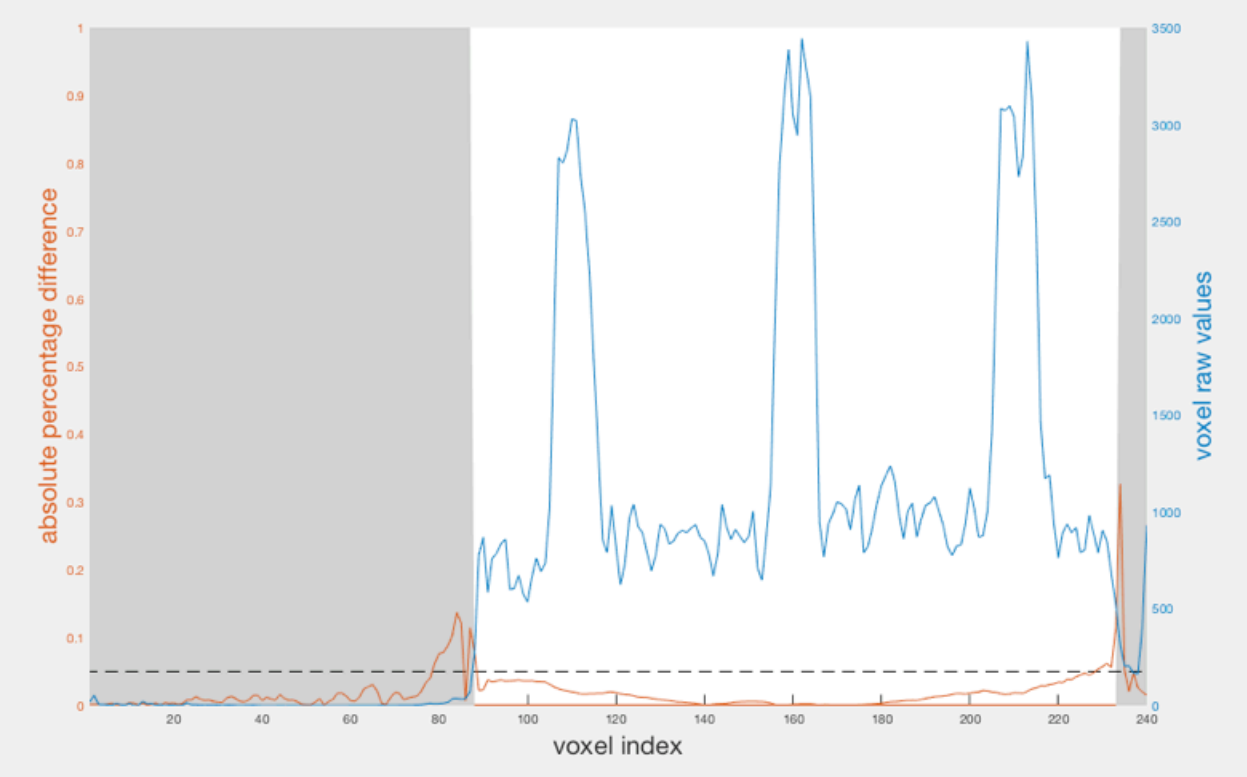

Figure 5.6. Profile through reconstructed images with XAC and trueAC.

The blue curve plots the profile in the reconstructed image with XAC (indicated by the white horizontal line in the top graph in Figure 5.5). The pink curve is the absolute percentage difference between the reconstructions using XAC and trueAC, defined as abs(1 - image_XAC / image_trueAC). The shaded area indicates the background (non-breast region). The dashed line of 5% difference is drawn for the convenience of reference.

Chapter 6. MEASURED DATA (ONGOING AS OF AUGUST 2018)

This chapter documents the most recent progress with the PET/X scanner as we start to collect measured data with physical phantom scans. Troubleshooting and debugging is common occurrence during this phase. Note that the preliminary images presented here are frequently updated.

6.1 Ge^{68} POINT SOURCE

Point sources are always the first choice of phantoms to try when working on a new imaging system. In fact it has helped us locate a few important bugs in the past. The following images come from a Germanium^{68} point source. The full-width-half-max values in the x, y and z directions are 1.7, 2.4 and 1.5 mm respectively.

As part of the debugging process, we also plot a few LOR's from the list mode data. It's a visual confirmation that the LORs converge to a point.

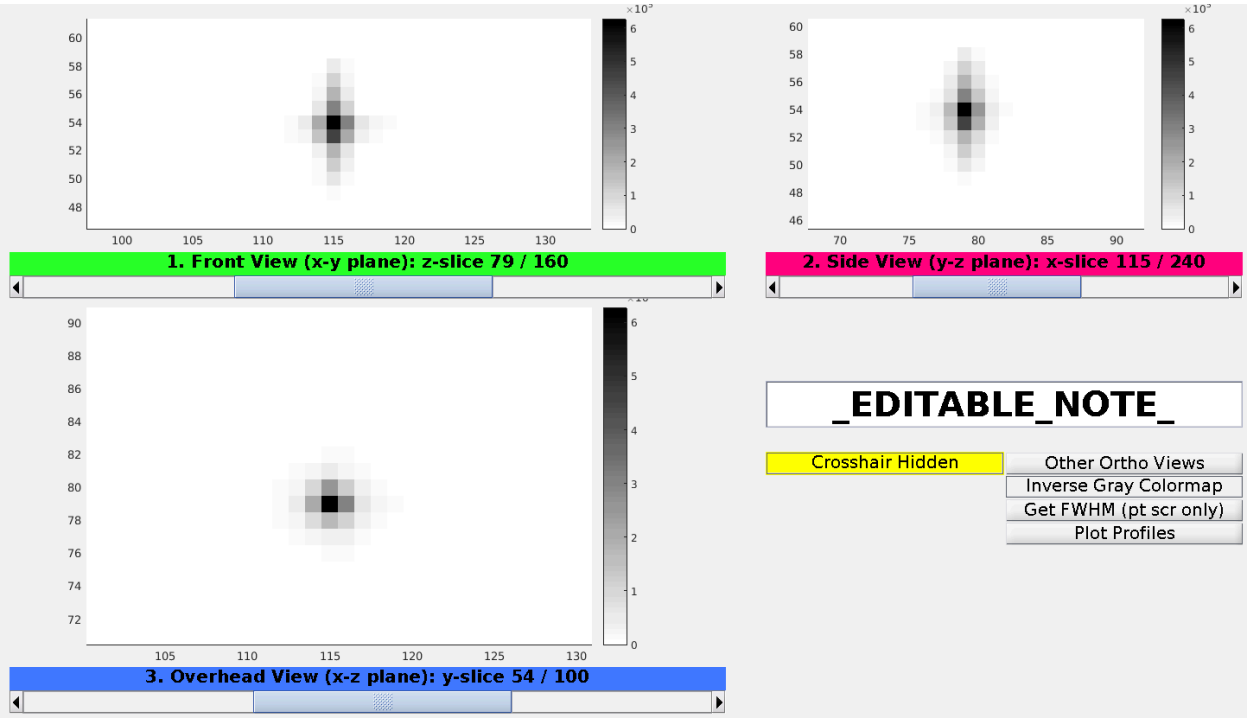

Figure 6.1. Reconstruction with measured data of the Ge^{68} point source. This is at iteration 30. The pixels in the images are 1 mm in all dimensions.

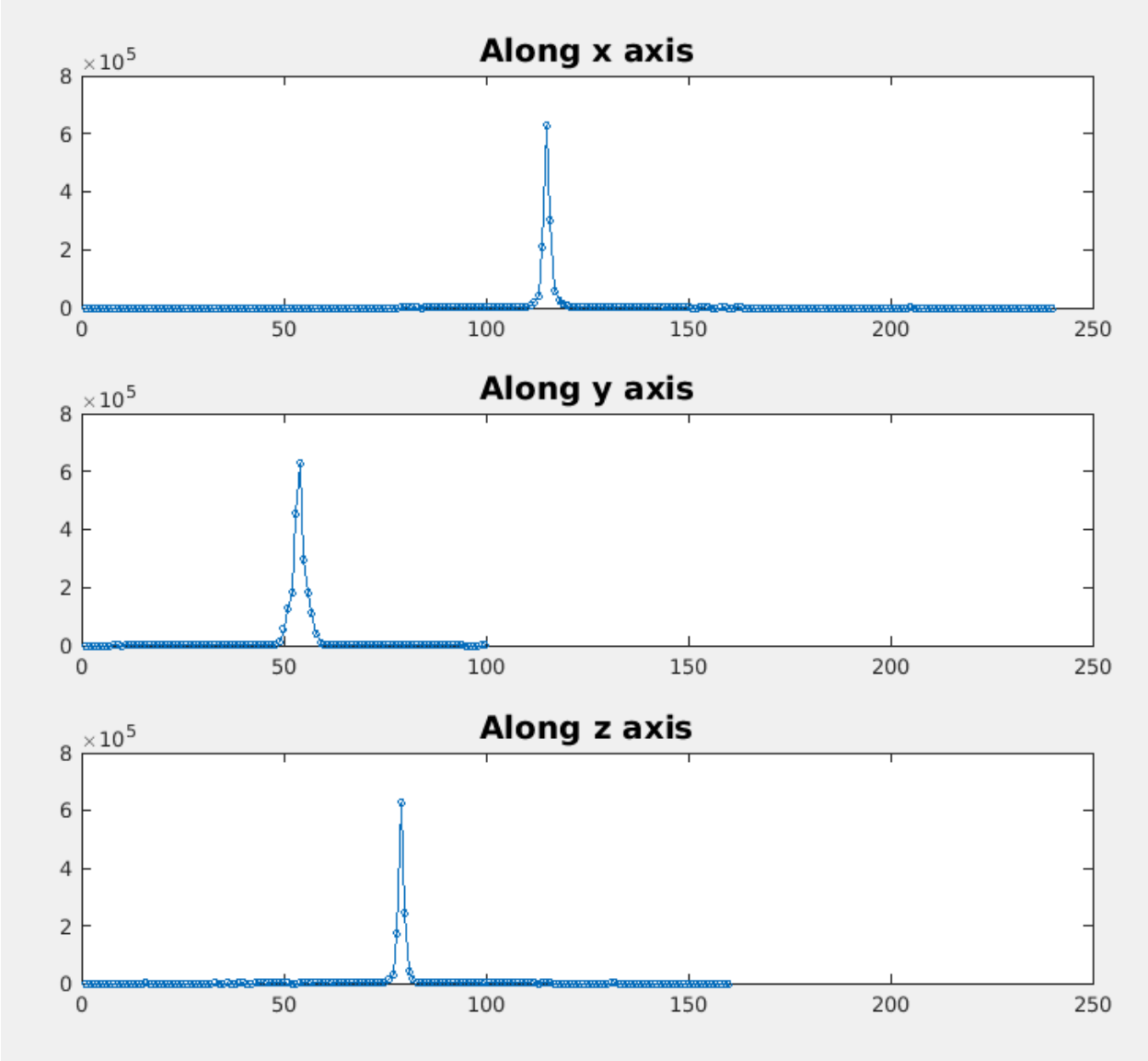

Figure 6.2. Profiles in x, y and z directions of the Ge^{68} point source reconstruction. The full-width-half-max values in the x, y and z directions are 1.7, 2.4 and 1.5 mm respectively using the linear interpolation method.

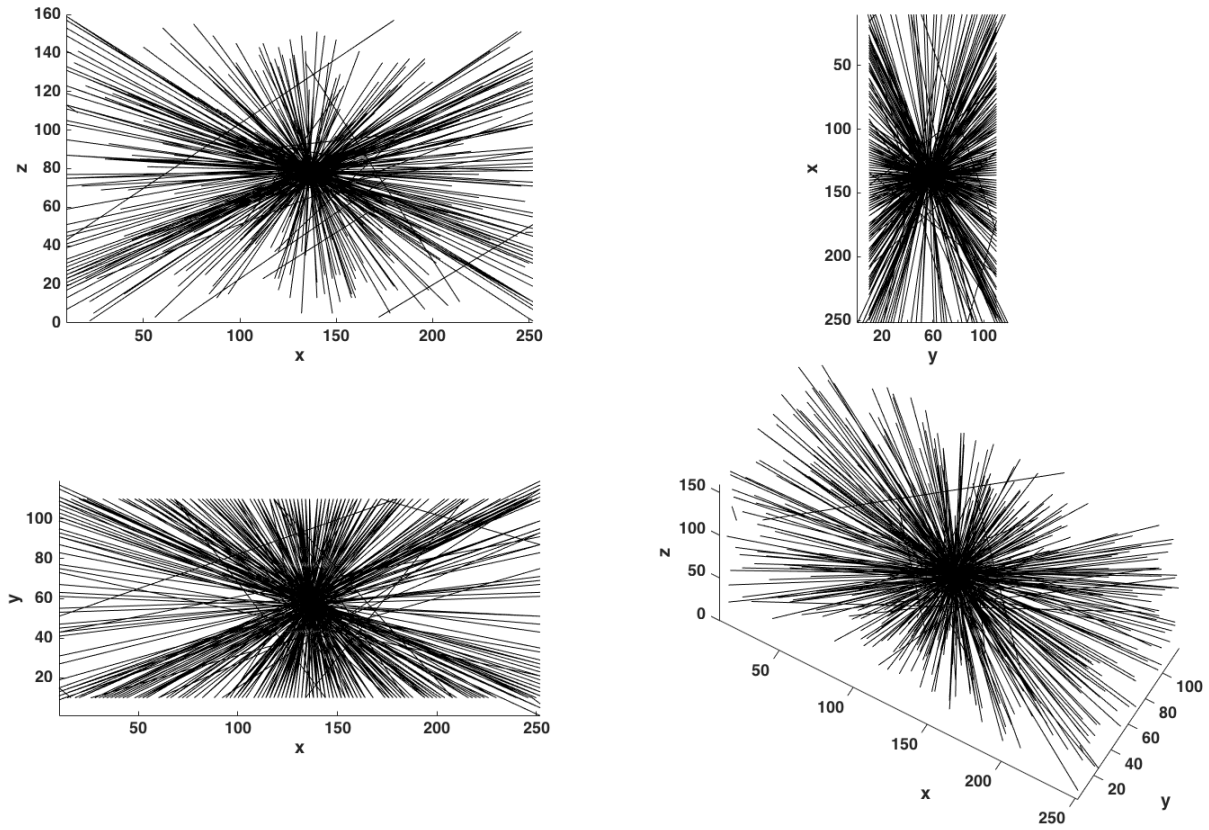

Figure 6.3. Plotting of LORs of the Ge^{68} point source measured data.

Simple plotting of the first few hundred LORs of the list mode data, as a visual confirmation that the majority of LORs go through a point source. No image reconstruction is involved.

6.2 GE^{68} VOLUMETRIC SOURCE

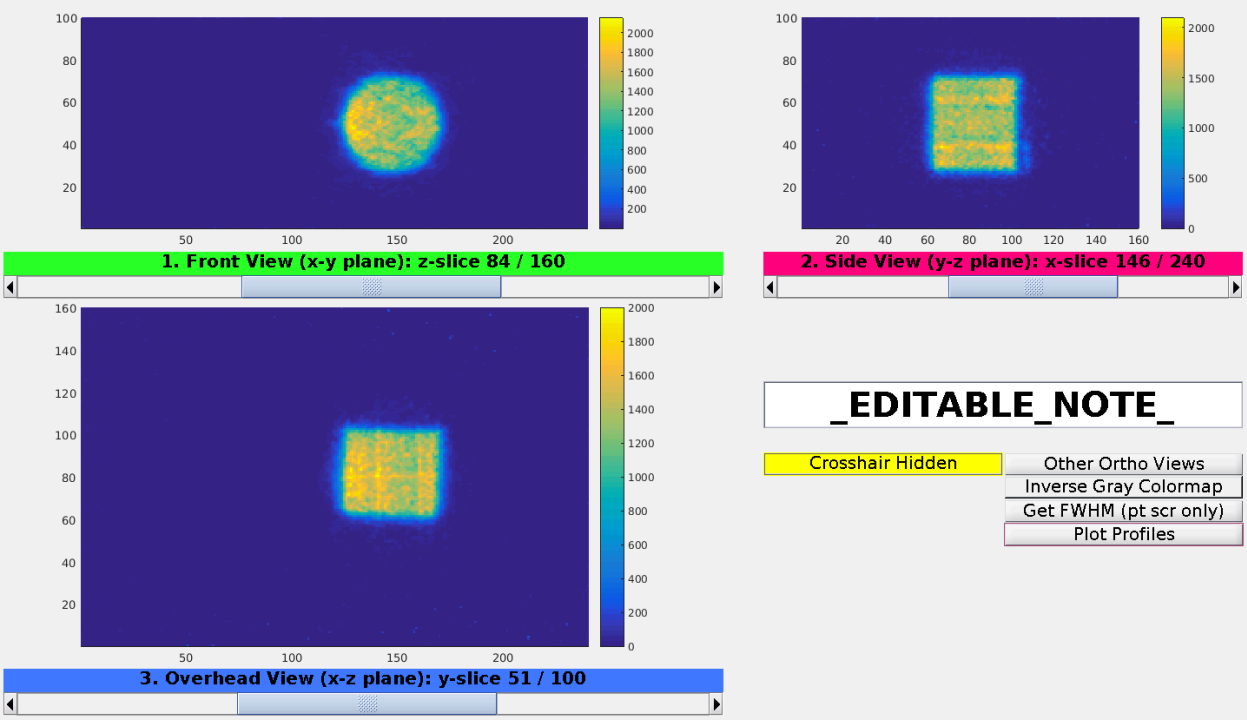

Figure 6.4. Reconstruction with measured data of the Ge^{68} cylindrical phantom. This is at iteration 30. No attenuation correction is used. The pixels in the images are 1 mm in all dimensions.

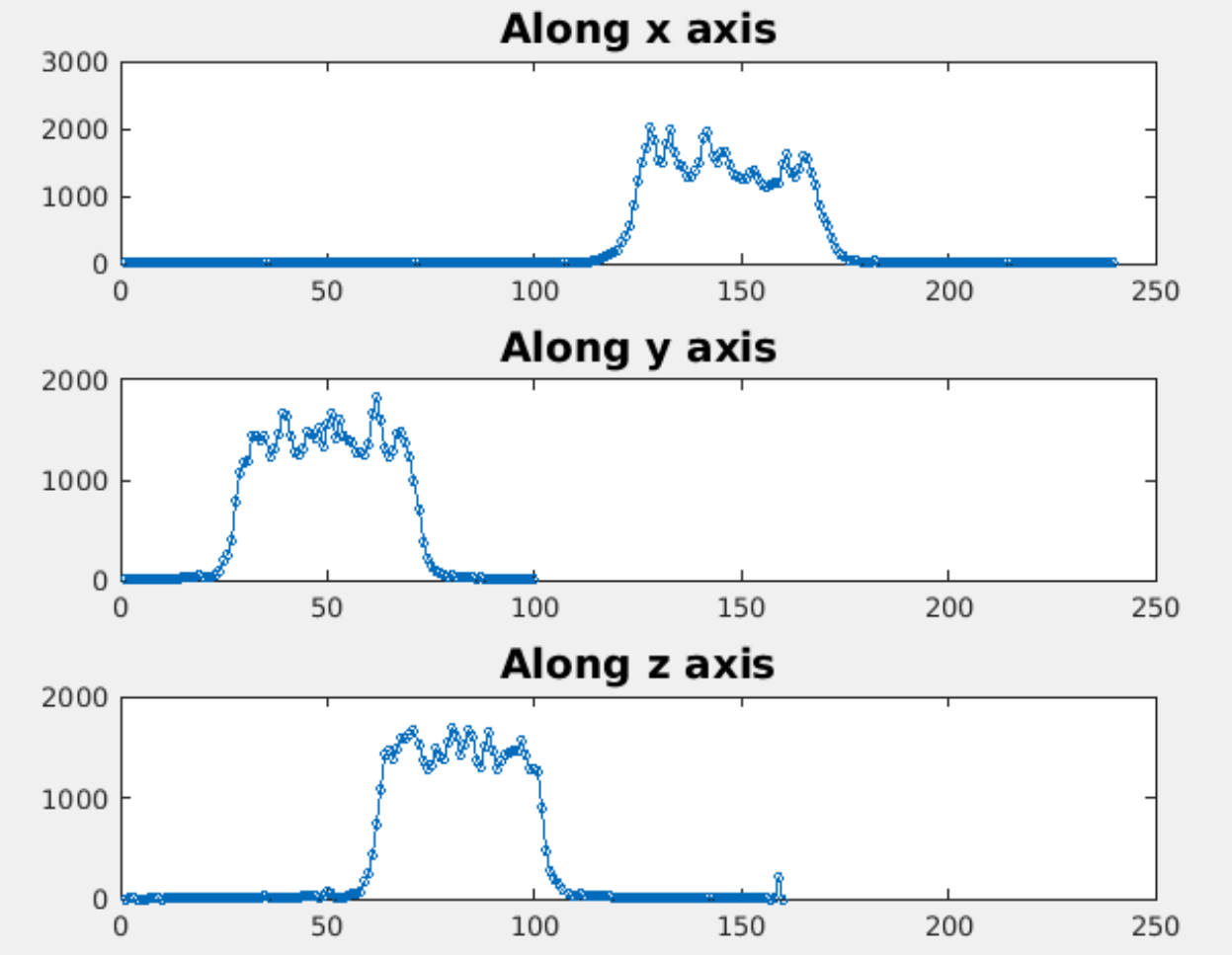

Figure 6.5. Profiles in x, y and z directions of the Ge^{68} cylindrical phantom reconstruction.

6.3 F^{18} VOLUMETRIC SOURCE

This F^{18} volumetric phantom comes from an unopened syringe that's sealed with FDG-F^{18} solution for clinical injection. It is imaged sequentially over the next 10 hours or so to get an estimate on our system's ability to handle high-count rate data. The reconstructed image uses the most decayed acquisition, with an activity level around 0.046 mCi.

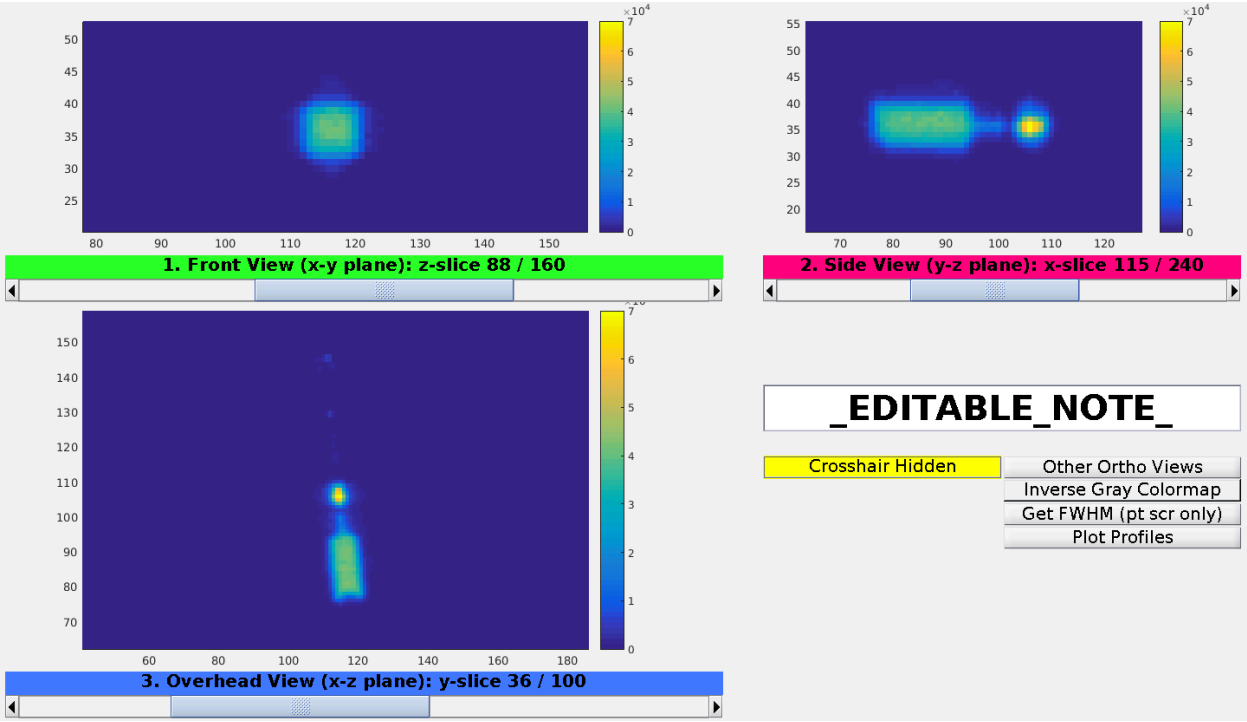

Figure 6.6. Reconstruction with measured data of the F^{18} volumetric phantom. This is at iteration 30. No attenuation correction is used. The pixels in the images are 1 mm in all dimensions.

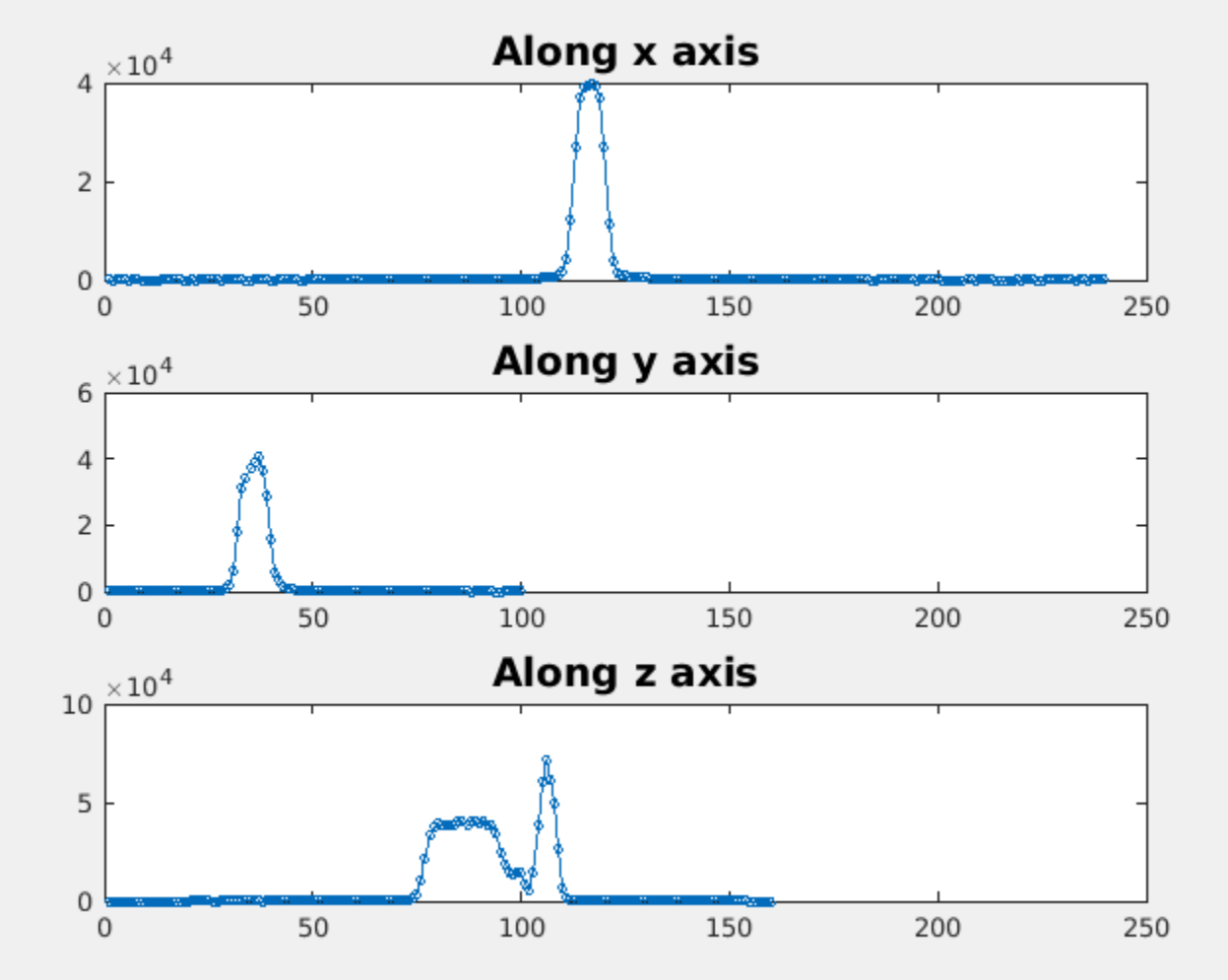

Figure 6.7. Profiles in x, y and z directions of the F^{18} volumetric phantom reconstruction.

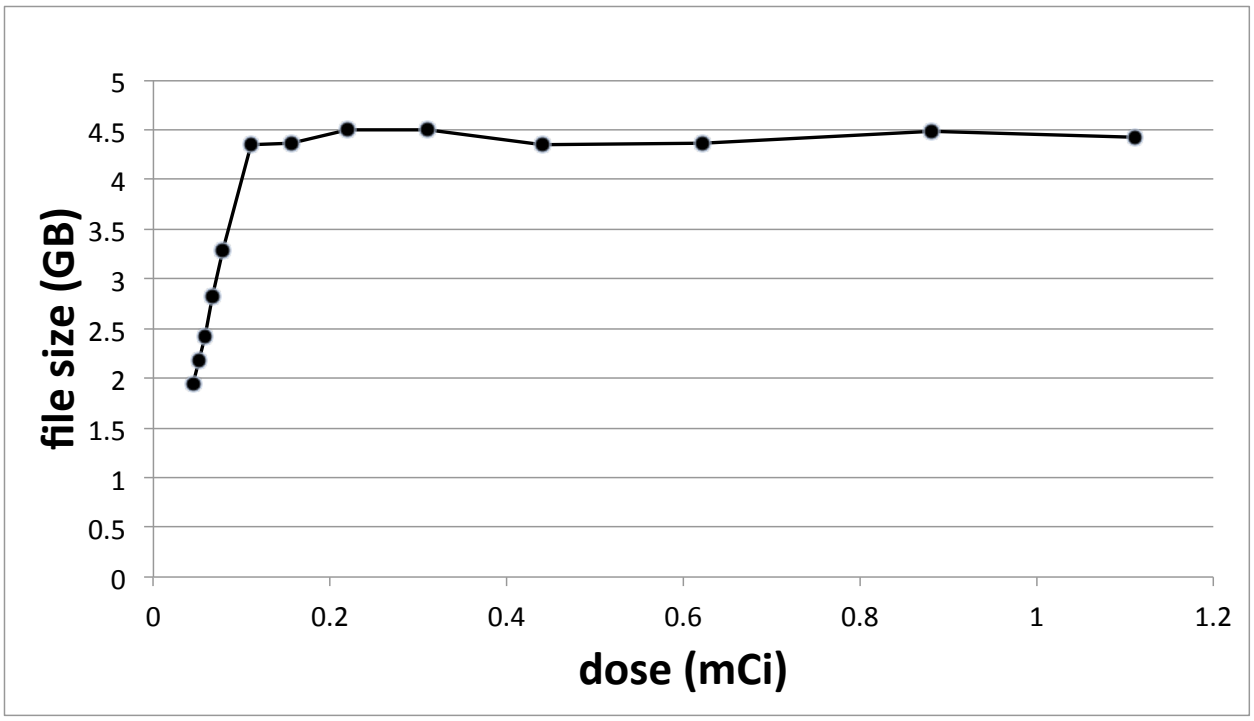

Figure 6.8. File size vs. radioactivity level for the syringe of FDG-F^{18}.

The radioactivity level is calculated based on the initial dose and timestamp stated on the FDG labeling. The file size is the raw binary file size directly acquired from the system, including header information. It can be viewed as a pseudo indicator of the coincidence counts. The turning point occurs at the activity level of roughly 0.1 mCi.

Chapter 7. FUTURE WORK

7.1 INCORPORATING DETECTOR CHARACTERISTICS INTO MODELING

A more realistic simulation model should include the detector characteristics, such as energy window and blurring. In previous presented simulation result from SimSET, the energy resolution in the detectors was left out, resulting in a perfect energy resolution. It was done due to 2 considerations. First we wanted to establish a performance upper bound that's independent of detector blurring, but rather focusing on system geometry. Second, at the time of simulation, exact characterization of the detectors we planned to deploy on the PET/X prototype was not yet

available. In the future, one could either set the corresponding parameters in SimSET to appropriate values, or leave the simulation as is and add in the detector blurring and windowing in post-processing of the list mode history data.

7.2 CORRECTION OF CRYSTAL BLOCK GAPS

Hua's reconstruction package has an upgraded version that models the gaps between crystal blocks. Ideally this would match the gap setup in SimSET or the physical setup of the PET/X prototype. However, due to a rushed delivery, this version of code has not been fully tested and validated. The previous presented results were all reconstructed with the version that does not consider gaps. That is, the code assumes uniform distribution of crystal elements along each dimension. It appears that using the simpler version of the reconstruction code does not introduce significant artifacts. (Note that the gaps are much smaller than the crystal pitch.) On the contrary, we do not know how much improvement the upgraded version, if works, will bring to the final image.

7.3 OTHER DATA CORRECTIONS

7.3.1 *Events in the corners of the PET/X scanner*

A fine detail in Hua's reconstruction code is to assume no overlap of vertical and horizontal crystals around the corners. However this is not consistent with the actual setup of PET/X. From the simulation study I estimate that roughly 5% of the qualified events have one or both photons detected in the overlapped crystals. These events are currently filtered out since they cannot be binned into the planogram input for Hua's reconstruction package. I had experimented "rescuing" those events by back-projecting them into the neighboring bins on the top and bottom panels, but it's not yet made available to the workflow routine.

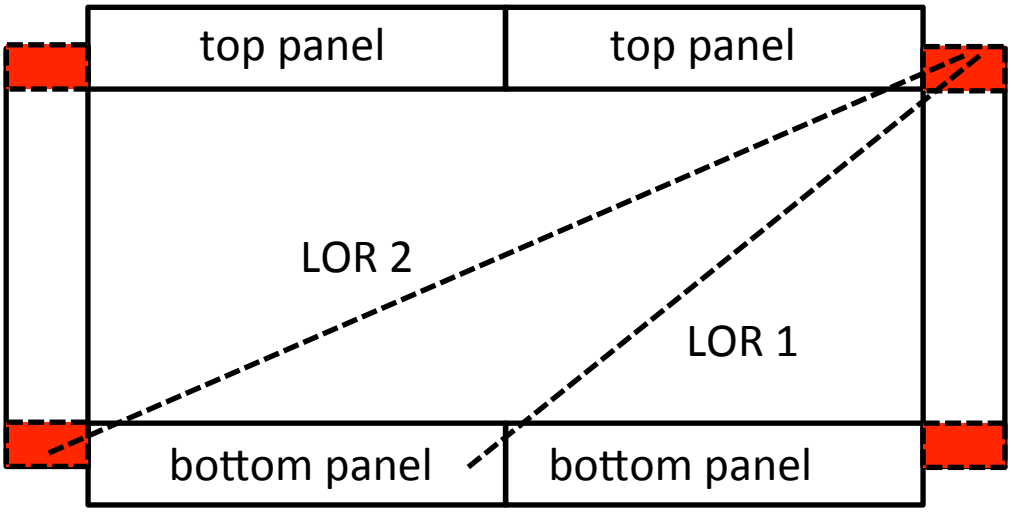

Figure 7.1. Corner events of the PET/X scanner.

Currently events detected in the overlapping corners (red highlighted areas) of the PET/X scanner are discarded in post-processing, as Hua's reconstruction code does not assume overlap between the main panels and side panels. Those events could have either one (illustrated by LOR 1) or both (illustrated by LOR 2) photons detected in the overlapped region.

7.3.2 *Crystal penetration correction*

Crystal penetration correction addresses the issue when a LOR goes through a path of crystal in the detector of length d_1, only $1-exp(-mu*d_1)$ of the original events are detected. If d_2 is the path length of crystal on the other end of the LOR, then a total fraction of $(1-exp(-mu*d_2))*(1-exp(-mu*d_1))$ of the original events are detected. Currently Hua's reconstruction code adopts a naïve crystal penetration correction by calculating the path lengths in crystals for each LOR connecting the corresponding bin pairs. The main assumption is that the four panels (top, bottom, left, right) extend infinitely faraway, without actually stopping at the corners. This clearly differs from the actual setup. I experimented calculating the correction factor based on the actual crystal size but unfortunately didn't yield much better result. It does appear that how the crystal penetration

correction is done could have a very noticeable impact on the reconstructed images. Much more time and effort need to be invested on this topic.

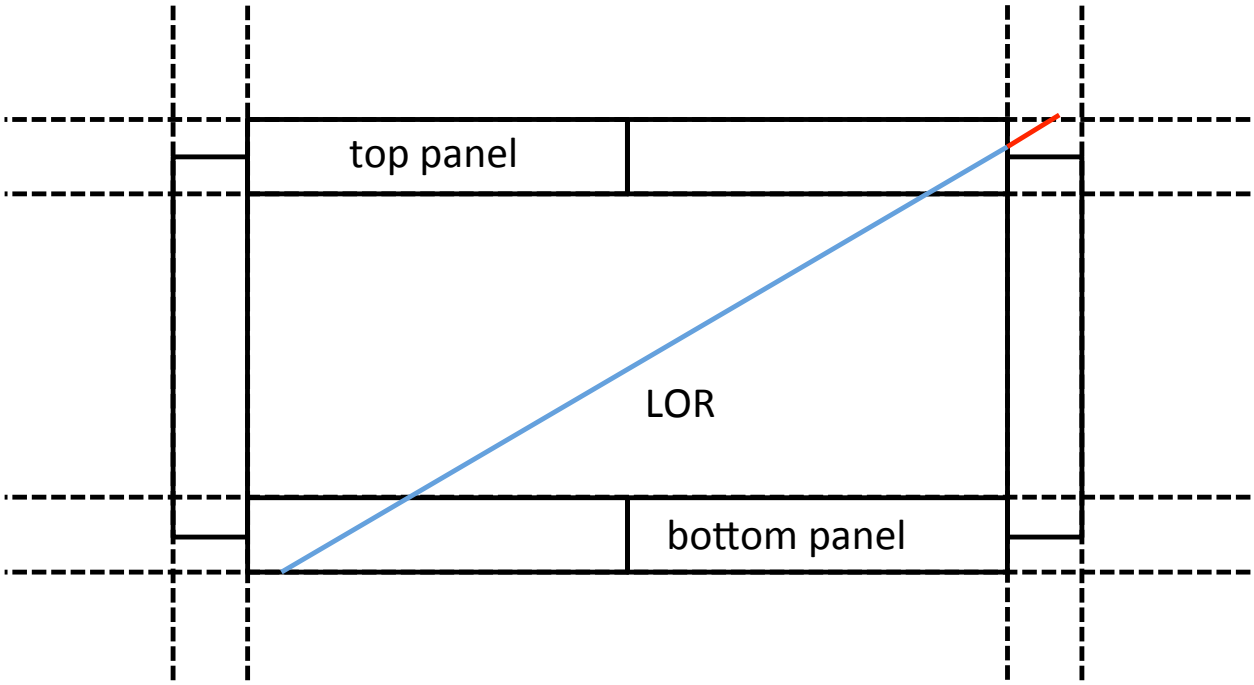

Figure 7.2. Crystal penetration correction in Hua's reconstruction code.

This figure shows the assumption used in Hua's reconstruction code to calculate crystal penetration correction. The solid black lines delineate detector crystals, while the dashed lines extend them infinitely without actually stopping at the corners. The crystal penetration correction in Hua's code is calculated based on the extension instead of the solid boundaries. Take the sample LOR (solid blue line) for example. While the blue line represents the true LOR through the detector crystals (with both ends on crystal boundaries), the calculation actually takes into account of the red portion as well (with one end extended to the dashed line). Hua's current implementation pre-calculates the crystal penetration correction as a multiplicative correction file given each specific configuration of the PET/X scanner.

7.3.3 *Other corrections*

Scatter correction and normalization are two other important data corrections we currently do not have, nor have spent much effort on. Normalization will probably be done empirically using some line or plane source. Note that if simulation is used, SimSET is at disposal of simulating analytical phantoms in forms of a line or plane.

7.4 WORKING WITH MEASURED DATA

Much of this thesis is based on the simulation of PET/X scanner, but ultimately it is the image from the measured data that proves its utility. Over the years we have gone through cycles of development of the data acquisition system and are finally starting to collect measured data. The results are rolling in as the thesis is being written.

7.5 EFFECT OF PET/X MODULE ON MAMMOGRAPHY

When PET/X is fully integrated with the mammography scanner, the mammogram will be taken under a different-than-normal condition. Specifically the breast is elevated due to PET/X's detector (bottom panel) between the breast and mammography detector. The breast is also under lighter compression due to the prolonged PET acquisition. While it's almost certain that the resulting mammogram is not a diagnostic one, we do not have much idea of how the new mammogram will work clinically in conjunction with the PET image.

Chapter 8. CONTRIBUTIONS

8.1 CatSim adaptation to mammography

CatSim is a simulation package that was previously used for CT simulation only. I modified it to simulate mammography. Since it's an internal simulation tool used by GE and lacks sufficient user support, I had to be extra proactive on the lookout for CatSim and mammography experts. To that end, I received very helpful tips from Pablo in GE, Buc, France. On my trip home to China, I also made a side trip to GE, Shanghai to have a chat with the code maintainer at the time. The modified CatSim now works with a polychromatic X-ray source for mammography and a voxelized phantom.

8.2 SimSET modification for PET/X geometry

SimSET is a well-supported package for PET and SPECT simulation. Previously it was not possible to simulate PET/X scanner due to its unique geometry. Since most scanners assume a circular FOV, SimSET is designed to enforce separation of detector elements and phantom object. I'm able to circumvent the restriction by breaking up the simulation into two separate steps and introducing in between a user-defined function. Now it is able to simulate PET/X without any restriction on the placement of detector elements and phantom object. I also make it now work with any analytical phantom, while earlier simulations prior to this study have been strictly with voxelized phantoms.

8.3 Testing and application of reconstruction algorithms

Both reconstruction packages are specifically written for the PET/X project by different remote authors. The codes have gone through multiple cycles of revisions back and forth between the

authors and me as they were written and re-tested. In overview, there are 3 major areas of effort that I spend time on. First is debugging. I test run them on my simulated PET data. When artifacts are observed, I make my best guess on where the algorithms can be improved and relay them back to the authors. Second is writing patch code to the packages. There are limitations of the algorithms that are recognized by the authors, and I ameliorate the situation by either amending the original code with patches or adding additional pre-processing/post-processing steps. The third area is tuning hyper parameters. It's especially important in iterative algorithms.

8.4 XAC SIMULATION STUDY WORKFLOW

XAC simulation study makes heavy use of CatSim, SimSET and reconstruction packages. Special care is given to the data format, image size and pixel/voxel resolution specific to each imaging modality. I make sure they will work with each other and fit them in a nice workflow.

8.5 DATA FORMATS AND WORKFLOW INTEGRATION

Because data can come from different sources: simulation packages, measured data, different processing codes, etc., they can have different formatting requirements. I work with different parties (hardware people, software people, clinical people) to standardize those data formats and make sure of the conversions in between them. The details can be found in section 2.2. The conversion code can be mostly found in *runDataflow.py*.

8.6 MACHINING AND DATA ACQUISITION

I also spend a fair amount of time machining the mechanical component of the PET/X prototype in the machine shop as well as acquiring the measured data in the front lab.

BIBLIOGRAPHY

[1] R. A. Weinberg, “The Biology of Cancer,” 2nd ed. 2014.

[2] R. L. Siegel, K. D. Miller and A. Jemal, “Cancer statistics, 2018.,” *CA Cancer J Clin*, vol. 68, no. 1, pp. 7-30, 2018

[3] C. E. DeSantis *et al.*, “Breast cancer statistics, 2017, racial disparity in mortality by state.,” *CA Cancer J Clin*, vol. 67, no. 6, pp. 439-448, 2017

[4] K. D. Miller *et al.*, “Cancer treatment and survivorship statistics, 2016.,” *CA Cancer J Clin*, vol. 66, no. 4, pp. 271-289, 2016

[5] K. P. McGuire *et al.*, “Are mastectomies on the rise? A 13-year trend analysis of the selection of mastectomy versus breast conservation therapy in 5865 patients.,” *Ann Surg Oncol*, vol. 16, no. 10, pp. 2682-2690, 2009

[6] J. Bushberg *et al.*, “The Essential Physics of Medical Imaging,” 3rd ed. 2011.

[7] K. Saika and T. Sobue, “Time trends in breast cancer screening rates in the OECD countries.,” *Jpn J Clin Oncol*, vol. 41, no. 4, pp. 591-592, 2011

[8] A. Bleyer and H. G. Welch, “Effect of three decades of screening mammography on breast-cancer incidence.,” *N Engl J Med*, vol. 367, no. 21, pp. 1998-2005, 2012

[9] B. L. Sprague *et al.*, “Prevalence of mammographically dense breasts in the United States.,” *J Natl Cancer Inst*, vol. 106, no. 10, 2014

[10] A. Coldman and N. Phillips, “Incidence of breast cancer and estimates of overdiagnosis after the initiation of a population-based mammography screening program.,” *CMAJ*, vol. 185, no. 10, pp. E492-8, 2013

[11] R. E. Hendrick and M. A. Helvie, “United States Preventive Services Task Force screening mammography recommendations: science ignored.,” *AJR Am J Roentgenol*, vol. 196, no. 2, pp. W112-6, 2011

[12] Y. Gao *et al.*, “Digital Breast Tomosynthesis Practice Patterns Following 2011 FDA Approval: A Survey of Breast Imaging Radiologists.,” *Acad Radiol*, vol. 24, no. 8, pp. 947-953, 2017

[13] F. A. Mettler *et al.*, “Effective doses in radiology and diagnostic nuclear medicine: a catalog.,” *Radiology*, vol. 248, no. 1, pp. 254-263, 2008

[14] G. Brix *et al.*, “Radiation exposure of patients undergoing whole-body dual-modality 18F-FDG PET/CT examinations.,” *J Nucl Med*, vol. 46, no. 4, pp. 608-613, 2005

[15] J. Vilar-Palop *et al.*, "Updated effective doses in radiology.," *J Radiol Prot*, vol. 36, no. 4, pp. 975-990, 2016

[16] C. J. Thompson *et al.*, "Feasibility study for positron emission mammography.," *Med Phys*, vol. 21, no. 4, pp. 529-538, 1994

[17] G. Gebhart *et al.*, "18F-FDG PET/CT for early prediction of response to neoadjuvant lapatinib, trastuzumab, and their combination in HER2-positive breast cancer: results from Neo-ALTTO.," *J Nucl Med*, vol. 54, no. 11, pp. 1862-1868, 2013

[18] D. Groheux *et al.*, "^{18}F-FDG PET/CT for the Early Evaluation of Response to Neoadjuvant Treatment in Triple-Negative Breast Cancer: Influence of the Chemotherapy Regimen.," *J Nucl Med*, vol. 57, no. 4, pp. 536-543, 2016

[19] K. K. Miyake, Y. Nakamoto and K. Togashi, "Current Status of Dedicated Breast PET Imaging," *Current Radiology Reports*, vol. 4, pp. 1-11, 2016

[20] F. Dehdashti *et al.*, "PET-based estradiol challenge as a predictive biomarker of response to endocrine therapy in women with estrogen-receptor-positive breast cancer.," *Breast Cancer Res Treat*, vol. 113, no. 3, pp. 509-517, 2009

[21] E. C. Dijkers *et al.*, "Biodistribution of 89Zr-trastuzumab and PET imaging of HER2-positive lesions in patients with metastatic breast cancer.," *Clin Pharmacol Ther*, vol. 87, no. 5, pp. 586-592, 2010

[22] L. Kostakoglu *et al.*, "A Phase II Study of 3'-Deoxy-3'-18F-Fluorothymidine PET in the Assessment of Early Response of Breast Cancer to Neoadjuvant Chemotherapy: Results from ACRIN 6688.," *J Nucl Med*, vol. 56, no. 11, pp. 1681-1689, 2015

[23] L. MacDonald *et al.*, "Clinical imaging characteristics of the positron emission mammography camera: PEM Flex Solo II.," *J Nucl Med*, vol. 50, no. 10, pp. 1666-1675, 2009

[24] H. Peng and C. S. Levin, "Design study of a high-resolution breast-dedicated PET system built from cadmium zinc telluride detectors.," *Phys Med Biol*, vol. 55, no. 9, pp. 2761-2788, 2010

[25] M. C. Abreu *et al.*, "Clear-PEM: A PET imaging system dedicated to breast cancer diagnostics," *Nuclear Instruments and Methods in Physics Research Section A: Accelerators, Spectrometers, Detectors and Associated Equipment. Proceedings of the 1st International Conference on Molecular Imaging TechnologyEuroMedIm 2006*, vol. 571, no. 1–2, pp. 81-84, 2007

[26] R. R. Raylman *et al.*, "The positron emission mammography/tomography breast imaging and biopsy system (PEM/PET): design, construction and phantom-based measurements.," *Phys Med Biol*, vol. 53, no. 3, pp. 637-653, 2008

[27] L. Moliner *et al.*, "Design and evaluation of the MAMMI dedicated breast PET.," *Med Phys*, vol. 39, no. 9, pp. 5393-5404, 2012

[28] K. K. Miyake *et al.*, "Performance Evaluation of a New Dedicated Breast PET Scanner Using NEMA NU4-2008 Standards.," *J Nucl Med*, vol. 55, no. 7, pp. 1198-1203, 2014

[29] A. Ferrero *et al.*, "Preliminary performance characterization of DbPET2.1, a PET scanner dedicated to the imaging of the breast and extremities," *Biomedical Physics & Engineering Express*, vol. 1, pp. 015202, 2015

[30] B. Ravindranath *et al.*, "Results from prototype II of the BNL simultaneous PET-MRI dedicated breast scanner," *2009 IEEE Nuclear Science Symposium Conference Record (NSS/MIC)*, pp. 3315-3317, 2009

[31] M. J. Michell *et al.*, "A comparison of the accuracy of film-screen mammography, full-field digital mammography, and digital breast tomosynthesis.," *Clin Radiol*, vol. 67, no. 10, pp. 976-981, 2012

[32] A. Tingberg, "X-ray tomosynthesis: a review of its use for breast and chest imaging.," *Radiat Prot Dosimetry*, vol. 139, no. 1-3, pp. 100-107, 2010

[33] L. A. Hardesty, S. M. Kreidler and D. H. Glueck, "Digital breast tomosynthesis utilization in the United States: a survey of physician members of the Society of Breast Imaging.," *J Am Coll Radiol*, vol. 11, no. 6, pp. 594-599, 2014

[34] W. A. Berg, "Tailored supplemental screening for breast cancer: what now and what next," *AJR Am J Roentgenol*, vol. 192, no. 2, pp. 390-399, 2009

[35] K. M. Kelly *et al.*, "Breast cancer detection using automated whole breast ultrasound and mammography in radiographically dense breasts.," *Eur Radiol*, vol. 20, no. 3, pp. 734-742, 2010

[36] G. M. Rauch *et al.*, "Multimodality Imaging for Evaluating Response to Neoadjuvant Chemotherapy in Breast Cancer.," *AJR Am J Roentgenol*, vol. 208, no. 2, pp. 290-299, 2017

[37] B. J. Hillman *et al.*, "Diagnostic performance of a dedicated 1.5-T breast MR imaging system.," *Radiology*, vol. 265, no. 1, pp. 51-58, 2012

[38] C. K. Kuhl *et al.*, "Mammography, breast ultrasound, and magnetic resonance imaging for surveillance of women at high familial risk for breast cancer.," *J Clin Oncol*, vol. 23, no. 33, pp. 8469-8476, 2005

[39] W. A. Berg *et al.*, "Detection of breast cancer with addition of annual screening ultrasound or a single screening MRI to mammography in women with elevated breast cancer risk.," *JAMA*, vol. 307, no. 13, pp. 1394-1404, 2012

[40] M. L. Marinovich *et al.*, "Early prediction of pathologic response to neoadjuvant therapy in breast cancer: systematic review of the accuracy of MRI.," *Breast*, vol. 21, no. 5, pp. 669-677, 2012

[41] M. Morrow, J. Waters MLS and E. Morris, "MRI for breast cancer screening, diagnosis, and treatment," *The Lancet*, vol. 378, no. 9805, pp. 1804-1811, 2011

[42] D. Tzias *et al.*, "Current Status and New Developments in Breast Cancer Diagnosis and Detection," *European Oncology & Haematology*, vol. 9, no. 1, pp. 21-26, 2013

[43] Y. Sun *et al.*, "Clinical usefulness of breast-specific gamma imaging as an adjunct modality to mammography for diagnosis of breast cancer: a systemic review and meta-analysis.," *Eur J Nucl Med Mol Imaging*, vol. 40, no. 3, pp. 450-463, 2013

[44] B. J. Tromberg *et al.*, "Imaging in breast cancer: diffuse optics in breast cancer: detecting tumors in pre-menopausal women and monitoring neoadjuvant chemotherapy.," *Breast Cancer Res*, vol. 7, no. 6, pp. 279-285, 2005

[45] L. Xi *et al.*, "Molecular photoacoustic tomography of breast cancer using receptor targeted magnetic iron oxide nanoparticles as contrast agents.," *J Biophotonics*, vol. 7, no. 6, pp. 401-409, 2014

[46] Z. Ji *et al.*, "Three-dimensional thermoacoustic imaging for early breast cancer detection.," *Med Phys*, vol. 39, no. 11, pp. 6738-6744, 2012

[47] F. Beca and K. Polyak, "Intratumor Heterogeneity in Breast Cancer.," *Advances in Experimental Medicine and Biology*, vol. 882, pp. 169-189, 2016

[48] R. M. Connolly *et al.*, "TBCRC 008: early change in 18F-FDG uptake on PET predicts response to preoperative systemic therapy in human epidermal growth factor receptor 2-negative primary operable breast cancer.," *J Nucl Med*, vol. 56, no. 1, pp. 31-37, 2015

[49] B. Coudert *et al.*, "Use of [(18)F]-FDG PET to predict response to neoadjuvant trastuzumab and docetaxel in patients with HER2-positive breast cancer, and addition of bevacizumab to neoadjuvant trastuzumab and docetaxel in [(18)F]-FDG PET-predicted non-responders (AVATAXHER): an open-label, randomised phase 2 trial.," *Lancet Oncol*, vol. 15, no. 13, pp. 1493-1502, 2014

[50] L. Kenny *et al.*, "Imaging early changes in proliferation at 1 week post chemotherapy: a pilot study in breast cancer patients with 3'-deoxy-3'-[18F]fluorothymidine positron emission tomography.," *Eur J Nucl Med Mol Imaging*, vol. 34, no. 9, pp. 1339-1347, 2007

[51] L. M. Kenny *et al.*, "Altered tissue 3'-deoxy-3'-[18F]fluorothymidine pharmacokinetics in human breast cancer following capecitabine treatment detected by positron emission tomography.," *Clin Cancer Res*, vol. 15, no. 21, pp. 6649-6657, 2009

[52] C. Zeng *et al.*, "Simulation study of quantitative precision of the PET/X dedicated breast PET scanner.," *J Med Imaging (Bellingham)*, vol. 4, pp. 045502, 2017

[53] H. Young *et al.*, "Measurement of clinical and subclinical tumour response using [18F]-fluorodeoxyglucose and positron emission tomography: review and 1999 EORTC recommendations. European Organization for Research and Treatment of Cancer (EORTC) PET Study Group.," *Eur J Cancer*, vol. 35, no. 13, pp. 1773-1782, 1999

[54] R. L. Wahl *et al.*, "From RECIST to PERCIST: Evolving Considerations for PET response criteria in solid tumors.," *J Nucl Med*, vol. 50 Suppl 1, pp. 122S-50S, 2009

[55] J. S. Huber *et al.*, "A retrospective on the LBNL PEM project.," *Phys Med*, vol. 21 Suppl 1, pp. 60-63, 2006

[56] G. C. Wang *et al.*, "Characterization of the LBNL PEM camera," *IEEE Transactions on Nuclear Science*, vol. 53, no. 3, pp. 1129-1135, 2006

[57] K. M. Champley, R. R. Raylman and P. E. Kinahan, "Advancements to the planogram frequency-distance rebinning algorithm.," *Inverse Probl*, vol. 26, no. 4, pp. 45008, 2010

[58] H. Qian *et al.*, "Image reconstruction in rectangular PET systems using distance-driven projections," *2013 IEEE Nuclear Science Symposium and Medical Imaging Conference (2013 NSS/MIC)*, pp. 1-5, 2013

[59] L. R. MacDonald *et al.*, "Effects of Detector Thickness on Geometric Sensitivity and Event Positioning Errors in the Rectangular PET/X Scanner.," *IEEE Trans Nucl Sci*, vol. 60, no. 5, pp. 3242-3252, 2013

[60] H. Qian *et al.*, "Tradeoffs in Detector Design for a Rectangular Breast PET Scanner," *Journal of Nuclear Medicine*, vol. 56, no. supplement 3, pp. 1856-1856, 2015

[61] R. L. Harrison and T. K. Lewellen, "The SimSET Program," in *Monte Carlo Calculations in Nuclear Medicine*, 2nd ed., M. Ljungberg, S.-E. Strand and M. A. King, Eds. Boca Raton, FL: CRC press, 2012, pp. 87-110.

[62] R. S. Miyaoka *et al.*, "Resolution Properties of a Prototype Continuous Miniature Crystal Element (cMiCE) Scanner.," *IEEE Trans Nucl Sci*, vol. 58, no. 5, 2011

[63] L. A. Pierce *et al.*, "Multiplexing strategies for monolithic crystal PET detector modules.," *Phys Med Biol*, vol. 59, no. 18, pp. 5347-5360, 2014

[64] T. K. Lewellen, R. L. Harrison and S. G. Kohlmyer, "Effect of lower energy threshold on single and multiple scatter distributions in positron volume imaging," *IEEE Trans Nucl Sci*, vol. 46, 1999

[65] C. S. Levin, A. M. K. Foudray and F. Habte, “Impact of high energy resolution detectors on the performance of a PET system dedicated to breast cancer imaging,” *Physica Medica*, vol. XXI, no. supplement 1, 2006

[66] L. Wang, P. Chai and L. W. Wu, “Attenuation correction for dedicated breast PET using only emission data based on consistency conditions,” *Chinese Physics C*, vol. 37, no. 1, 2012

[67] A. Springer and O. R. Mawlawi, “Evaluation of the quantitative accuracy of a commercially available positron emission mammography scanner.,” *Med Phys*, vol. 38, no. 4, pp. 2132-2139, 2011

[68] A. Soriano *et al.*, “Attenuation correction without transmission scan for the MAMMI breast PET,” *Nuclear Instruments and Methods in Physics Research Section A: Accelerators, Spectrometers, Detectors and Associated Equipment*
NIMA_4th International Conference on Imaging techniques in Subatomic Physics, Astrophysics, Medicine, Biology and Industry, vol. 648, Supplement 1, pp. S75-S78, 2011

[69] A. Rodríguez-Ruiz, G. A. Agasthya and I. Sechopoulos, “The compressed breast during mammography and breast tomosynthesis: in vivo shape characterization and modeling.,” *Phys Med Biol*, vol. 62, no. 17, pp. 6920-6937, 2017

VITA

Geng Zeng was born in Nanchang, China. His family later moved to the tropical city Nanning, where he went through middle school and high school peacefully. The 18-year-old briefly attended university in Beijing before the thought of going abroad crystalized and interrupted his life. After much preparation, at the age of 20, he flew to Ohio, USA to start his undergraduate years at Denison University.

Moving to a new country was a turning point. The new environment, new people, new language and new culture amazed him and he absorbed, with eager excitement, everything like a roll of sponge. His horizon expanded from China-ly to worldly. He later graduated with magna cum laude, majoring in physics and minoring in math. He then lived in Germany to practice German during the gap half-year before graduate school.

Moving to Seattle was another turning point in life, when he started the PhD program at University of Washington. His personal life and social life also blossomed, thanks to the abundant wonderfulness the Pacific Northwest has to offer. A serendipitous encounter after the second year exposed him to the medical physics field, and he soon joined the current lab to do research on medical imaging devices. Academic fluidity also gave him the chance to attend other classes, during which he was splashed with a taste of machine learning and data science.

When he is not in the lab, the following venues have a bigger likelihood to locate him. Laboring in vegetable gardens, swimming in lakes or rivers, hiking in the mountains, watching musicals in theaters. If all of these fail, he is probably on the plane somewhere to see the world.